

SDSS-IV MaStar: Quantification and Abatement of Interstellar Absorption in the Largest Empirical Stellar Spectral Library

KATE H. R. RUBIN ^{1,2} KYLE B. WESTFALL ³ CLAUDIA MARASTON ⁴ DANIEL THOMAS ^{5,4} RENBIN YAN ⁶
J. CHRISTOPHER HOWK ⁷ ERICK AGUIRRE ⁸ KAELEE S. PARKER ⁹ AND DAVID R. LAW ¹⁰

¹*Department of Astronomy, San Diego State University, San Diego, CA 92182 USA*

²*Department of Astronomy and Astrophysics, University of California, San Diego, La Jolla, CA 92092, USA*

³*University of California Observatories, University of California, Santa Cruz, 1156 High St., Santa Cruz, CA 95064, USA*

⁴*Institute of Cosmology and Gravitation, University of Portsmouth, 1-8 Burnaby Road, Portsmouth PO1 3FX, UK*

⁵*School of Mathematics and Physics, University of Portsmouth, Lion Gate Building, Portsmouth, PO1 3HF, UK*

⁶*Department of Physics, The Chinese University of Hong Kong, Shatin, N.T., Hong Kong S.A.R., China*

⁷*Department of Physics and Astronomy, University of Notre Dame, Notre Dame, IN 46556, USA*

⁸*Department of Astronomy, New Mexico State University, Las Cruces, NM 88003, USA*

⁹*Department of Astronomy, The University of Texas at Austin, 2515 Speedway, Stop C1400, Austin, TX 78712, USA*

¹⁰*Space Telescope Science Institute, 3700 San Martin Drive, Baltimore, MD 21218, USA*

ABSTRACT

We assess the impact of Ca II $\lambda\lambda 3934, 3969$ and Na I $\lambda\lambda 5891, 5897$ absorption arising in the interstellar medium (ISM) on the SDSS-IV MaNGA Stellar Library (MaStar) and produce corrected spectroscopy for 80% of the 24,162-star catalog. We model the absorption strength of these transitions as a function of stellar distance, Galactic latitude, and dust reddening based upon high-spectral resolution studies. With this model, we identify 6342 MaStar stars that have negligible ISM absorption ($W^{\text{ISM}}(\text{Ca II K}) < 0.07 \text{ \AA}$ and $W^{\text{ISM}}(\text{Na I } 5891) < 0.05 \text{ \AA}$). For 12,110 of the remaining stars, we replace their Na I D profile (and their Ca II profile for effective temperatures $T_{\text{eff}} > 9000 \text{ K}$) with a coadded spectrum of low-ISM stars with similar T_{eff} , surface gravity, and metallicity. For 738 additional stars with $T_{\text{eff}} > 9000 \text{ K}$, we replace these spectral regions with a matching ATLAS9-based BOSZ model. This results in a mean reduction in $W(\text{Ca II K})$ ($W(\text{Na I D})$) of $0.4 - 0.7 \text{ \AA}$ ($0.6 - 1.1 \text{ \AA}$) for hot stars ($T_{\text{eff}} > 7610 \text{ K}$), and a mean reduction in $W(\text{Na I D})$ of $0.1 - 0.2 \text{ \AA}$ for cooler stars. We show that interstellar absorption in simple stellar population (SSP) model spectra constructed from the original library artificially enhances $W(\text{Ca II K})$ by $\gtrsim 20\%$ at young ages ($< 400 \text{ Myr}$); dramatically enhances the strength of stellar Na I D in starbursting systems (by $\gtrsim 50\%$); and enhances stellar Na I D in older stellar populations ($\gtrsim 10 \text{ Gyr}$) by $\gtrsim 10\%$. We provide SSP spectra constructed from the cleaned library, and discuss the implications of these effects for stellar population synthesis analyses constraining stellar age, [Na/Fe] abundance, and the initial mass function.

1. INTRODUCTION

Stellar spectral template libraries are fundamental tools for the analysis of spectroscopy of external galaxies. Catalogs of spectra of individual Milky Way stars were crucial to the earliest efforts to understand the chemical abundances and stellar populations of nearby galaxies (Spinrad & Taylor 1971; Faber 1972; O’Connell 1976; Turnrose 1976; Pickles 1985). Their use continues to serve an exceptionally broad range of science topics,

from galactic stellar and gas dynamics (e.g., Cappellari et al. 2011; Cappellari 2016; Bloom et al. 2017; Westfall et al. 2019; Bryant et al. 2019; Law et al. 2022), to stellar and gas-phase chemical abundances and evolution (e.g., Tremonti et al. 2004; Ho et al. 2015; Belfiore et al. 2017, 2019; Parikh et al. 2019, 2021; Neumann et al. 2021), to stellar initial mass function (IMF) studies (e.g., Treu et al. 2010; Thomas et al. 2011c; Conroy & van Dokkum 2012b; Parikh et al. 2018; Bernardi et al. 2023).

Measurement of quantities relevant to each of these topics relies on the modeling of galaxy continua using stellar template spectra. These templates may be derived from the coaddition of individual stellar library

spectra with similar parameters (e.g., effective temperature, surface gravity, and metallicity; Westfall et al. 2019), or are constructed from selected library stars to represent simple stellar populations (SSPs) having a range of ages and chemical abundances (e.g., Tinsley 1978; Bruzual 1983; Guiderdoni & Rocca-Volmerange 1987; Worthey et al. 1994; Maraston 1998; Leitherer & Heckman 1995; Vazdekis 1999; Bruzual & Charlot 2003; Maraston & Strömbäck 2011; Conroy 2013; Maraston et al. 2020). The stellar continua of distant galaxy populations may then be modeled using linear combinations of these templates.

Theoretical stellar libraries calculated from models of stellar atmospheres (e.g., Kurucz 1993; Coelho et al. 2005; Rodríguez-Merino et al. 2005; Bohlin et al. 2017; Eldridge et al. 2017) are advantageous in that they can be produced at arbitrarily high spectral resolution, and can sample any chemical abundance pattern of interest to the user. However, such calculations have not yet fully accounted for the numerous physical processes that give rise to the profile shapes of stellar absorption lines (e.g., Kurucz 2011). For example, the model atmospheres upon which they are built rely on our incomplete knowledge of the relevant atomic and molecular transitions, as well as upon accurate calculation of absorption line opacities. This becomes challenging at low effective temperatures (T_{eff}) due to the profusion of molecular transitions (e.g., Coelho 2014; Bohlin et al. 2017).

Alternatively, empirical libraries may be constructed through spectroscopic campaigns targeting stars within $\lesssim 15$ kpc of the Sun. Traditionally, such libraries have been limited in their coverage of stellar parameter space, such that they are likely not fully representative of distant galaxy stellar populations (Yan et al. 2019). However, the recent completion of the Mapping Nearby Galaxies at Apache Point Observatory (MaNGA) survey (Bundy et al. 2015; Yan et al. 2016) has included the construction and publication of the MaNGA Stellar Library (MaStar), by far the largest empirical stellar library to date (Yan et al. 2019; Chen et al. 2020; Abdurro'uf et al. 2022; Hill et al. 2022; Imig et al. 2022; Lazarz et al. 2022). MaStar includes over an order of magnitude more stars than any other empirical library in common use (e.g., MILES, STELIB, INDOUS; Sánchez-Blázquez et al. 2006; Le Borgne et al. 2003; Valdes et al. 2004) at a spectral resolution ($\mathcal{R} \sim 1800$) and with wavelength coverage (3622 – 10354 Å) matching that of the MaNGA survey data. It is furthermore constructed from high-quality spectra having, e.g., precise and accurate wavelength and flux calibration and telluric correction (Yan et al. 2019; Abdurro'uf et al. 2022). Such a library is required to comprehensively

model the broad diversity of spectra among MaNGA's $\sim 10,000$ galaxy targets (Yan et al. 2019).

Even with the significant advances of MaStar, any empirical library is nevertheless affected by the presence of the Milky Way's interstellar medium (ISM). The broad range of gas temperatures and densities in and around the Galactic plane gives rise to strong absorption in resonant transitions across the ultraviolet and optical (e.g., Hartmann 1904; Hobbs 1969, 1974; Sembach et al. 1999; Richter et al. 2001a,b; Wakker 2001; Pellerin et al. 2002; Robert et al. 2003; Howk et al. 2003; Yao et al. 2009; Lehner & Howk 2011). The profusion of far- and near-UV metal-line transitions tracing warm neutral or ionized material (e.g., O VI $\lambda 1031$, O I $\lambda 1302$, Si II $\lambda 1260$, C IV $\lambda 1548$, among many others), in combination with the numerous Lyman and Werner transitions of molecular hydrogen at $980 \text{ \AA} < \lambda_{\text{rest}} < 1120 \text{ \AA}$ (Tumlinson et al. 2002), introduce significant “contaminating” absorption into Galactic stellar UV spectroscopy (Pellerin et al. 2002; Robert et al. 2003; Crowther 2022). In the optical, the Ca II $\lambda\lambda 3934, 3969$ and Na I $\lambda\lambda 5891, 5897$ transitions have long been understood to trace the warm (temperature $T > 10,000$ K) and cold ($T < 1000$ K) phases of the ISM (Hartmann 1904; Münch & Zirin 1961; Hobbs 1969, 1974; Crawford 1992; Welty et al. 1996; Richter et al. 2011; Puspitarini & Lallement 2012). More recent studies have demonstrated a close association between these transitions and massive H I cloud complexes observed in 21 cm emission (e.g., Wakker 2001; Ben Bekhti et al. 2008, 2012; Bish et al. 2019).

The absorption strength of Ca II and Na I has also been demonstrated to correlate strongly with dust reddening, both within the Milky Way (Phillips et al. 1984; Sembach & Danks 1994; Munari & Zwitter 1997; Welty et al. 2006; Poznanski et al. 2012; Welty et al. 2012; Murga et al. 2015) and in extragalactic systems (Wild & Hewett 2005; Zych et al. 2009; Chen et al. 2010b; Phillips et al. 2013; Baron et al. 2016; Rupke et al. 2021). The widely used Poznanski et al. (2012) relation between $E(B - V)$ and the equivalent width of the Na I D doublet ($W(\text{Na I})$) observed toward extragalactic sources probing the Milky Way ISM and halo predicts that even a modest degree of reddening is associated with significant interstellar Na I; e.g., it implies an absorption strength of $\approx 0.7 \text{ \AA}$ for $E(B - V) = 0.1$. Given that early-type (O/B/A) stars are preferentially located in dusty star-forming regions, their spectra may suffer an even greater degree of contamination. Considering that late-type galaxies typically exhibit NaD spectral index strengths of $1.0 - 3.5 \text{ \AA}$ (Parikh et al. 2021), it is plausible that the level of Milky Way Na I D contamination in empirical stellar library spectra is as strong as that

observed in the extragalactic systems these templates are being used to model. For analyses that draw on the NaD spectral index as an indicator of stellar sodium abundance by linking its observed strength to that predicted in SSP models (e.g., Thomas et al. 2003, 2011b; Martín-Navarro et al. 2015; Parikh et al. 2019, 2021), this implies that such [Na/Fe] constraints are systematically underestimated (as we demonstrate in Section 4). Analyses making use of the Na I D doublet to trace the absorption strength and kinematics of cool interstellar gas in extragalactic systems will likewise be affected, as they typically rely on stellar continuum modeling to remove the contribution of stellar atmospheres from the observed line profiles. Those studies of interstellar gas kinematics that are based upon data sets of modest spectral resolution ($\mathcal{R} \lesssim 3000$; e.g., Chen et al. 2010b; Cazoli et al. 2014; Concas et al. 2019; Roberts-Borsani & Saintonge 2019; Perna et al. 2020, 2021; Roberts-Borsani et al. 2020; Avery et al. 2022) would be most severely impacted by the implied systematic overestimation of the stellar component of Na I D.

In this work, we address this issue by removing Milky Way interstellar Ca II $\lambda\lambda 3934, 3969$ and Na I $\lambda\lambda 5891, 5897$ absorption from the MaStar empirical stellar library. We begin by assembling high-resolution spectroscopic observations of interstellar Ca II and Na I absorption toward early-type stars from the literature (Sembach et al. 1993; Munari & Zwitter 1997; Welsh et al. 2010). We use these data to build simple models of the equivalent widths of these transitions (W^{ISM}) as a function of stellar distance, Galactic latitude, and the dust reddening measured along the stellar sightline. We then use these models to estimate the level of ISM contamination toward each MaStar object, and identify a subset of the library for which the contamination level is minimal ($W^{\text{ISM}}(\text{Ca II K}) < 0.07 \text{ \AA}$ and $W^{\text{ISM}}(\text{Na I } 5891) < 0.05 \text{ \AA}$). These “low-ISM” sightlines comprise $\approx 27\%$ of the spectral sample. For each of the remaining stars, we identify subsets of the low-ISM sample that have similar stellar parameters (T_{eff} , surface gravity or $\log g$, and [Fe/H]) where possible, coadd the spectra within these subsets, and replace the portions of the affected star’s spectrum immediately surrounding the Ca II and Na I transitions with the coadd. For those stars for which we could not identify a low-ISM replacement subset that was sufficiently close in stellar parameter space, and which have $T_{\text{eff}} > 9000 \text{ K}$, we instead draw on the theoretical stellar library of Bohlin et al. (2017) to replace the affected spectral regions.

We demonstrate the presence of Milky Way interstellar absorption in a subset of early-type stars from the MaStar library, build our model of interstellar Ca II and

Na I absorption, and identify our “low-ISM” subsample in Section 2. In Section 3, we assess the intrinsic dispersion in the Ca II and Na I profiles of low-ISM stars with similar stellar parameter values; describe our spectral coaddition technique; and describe our profile replacement procedures. Section 3.4 presents the final “cleaned” MaStar spectroscopy and assesses the change in absorption strength of the stellar Ca II and Na I D profiles relative to the original library. In Section 3.5, we use a hierarchical clustering technique to construct a set of 58 coadded templates from our cleaned spectra that are representative of the library’s stars, and that may be used for continuum modeling of galaxy spectra. In Section 3.6, we present a suite of SSP model spectral templates constructed from our cleaned spectra which may be used for stellar population synthesis studies. The cleaned stellar spectra, hierarchically-clustered templates, and SSP templates are all publicly available.¹ To our knowledge, this is the only extant stellar empirical library with relatively low spectral resolution ($\mathcal{R} \lesssim 10,000$) for which the effects of absorption lines arising in the Milky Way’s ISM have been assessed and corrected (although corrections have been offered for ultraviolet stellar spectroscopy and higher-resolution optical libraries; e.g., Taresch et al. 1997; Robert et al. 2003; Borisov et al. 2023). Finally, we discuss the implications of our results for studies of stellar population age, sodium abundance, and IMF in extragalactic systems in Section 4.

2. A MODEL OF INTERSTELLAR CA II AND NA I ABSORPTION

2.1. *Interstellar Ca II and Na I in MaStar Stellar Spectroscopy*

We begin our investigation by searching for direct evidence of the impact of interstellar Ca II and Na I absorption on spectra drawn from the MaStar library. Spectral types O, B, and A are commonly used as background probes of foreground interstellar absorption, in part due to the weakness of the intrinsic absorption in their atmospheres. This suggests that an analysis of early-type MaStar stars may provide the most straightforward evidence of contamination from the ISM. However, first we must quantify the strengths of the intrinsic absorption that is expected from these stars, since the resolution of

¹ The cleaned stellar spectra are available at Zenodo at <https://doi.org/10.5281/zenodo.14014915>. The full set of SSP templates is available at <https://doi.org/10.5281/zenodo.14807331>. The hierarchically-clustered templates, as well as a subset of the SSP templates which have been modified for use with the MaNGA Data Analysis Pipeline are available at https://github.com/sdss/mangadap/tree/4.2.0/mangadap/data/spectral_templates.

MaStar spectroscopy is too low to differentiate intrinsic stellar profiles from interstellar absorbers.

We note here that high-resolution stellar spectroscopy has also revealed significant telluric absorption in the wavelength range $5885 \text{ \AA} < \lambda < 5906 \text{ \AA}$ (e.g., Lallement et al. 1993; Chen et al. 2014; Sandford et al. 2023). Any telluric contamination of the Na I D spectral region can be modeled and corrected for at high spectral resolution, but has not been removed from the MaStar spectra (Yan et al. 2016, 2019). In Appendix A, we show that the strength of telluric absorption features in this wavelength range is likely to be negligible ($< 0.1 \text{ \AA}$) given the atmospheric conditions at Apache Point Observatory during the observations of the vast majority of the MaStar sample. However, we also demonstrate that telluric absorption may be significant ($\sim 0.1 - 0.2 \text{ \AA}$) in a small minority of spectra. Studies that require precision stellar population modeling of Na I may therefore benefit from an additional correction for telluric effects.

Returning to our effort to assess the intrinsic strengths of Ca II and Na I D in hot stars, we draw on the theoretical stellar spectra computed by Maraston & Strömbäck (2011). These templates rely on model stellar atmospheres described in full by Maraston et al. (2009), and are based on the UVBLUE and BLUERED libraries of $\mathcal{R} = 10,000$ theoretical spectra computed by Rodríguez-Merino et al. (2005). We continuum-normalize each template spectrum using a linear fit to feature-free spectral regions on either side of each transition. We then compute the boxcar W over the ranges $3931.0 \text{ \AA} < \lambda_{\text{air}} < 3935.5 \text{ \AA}$ and $5895.0 \text{ \AA} < \lambda_{\text{air}} < 5896.5 \text{ \AA}$ to assess the strength of Ca II K and Na I 5897, respectively. In the case of Ca II K, the spectral window also includes absorption from neighboring, weak metal-line transitions which dominate the equivalent width in stars with $T_{\text{eff}} \geq 40,000 \text{ K}$. Measurements of these line strengths in all theoretical spectra having metallicities $Z = Z_{\odot}$ and $2Z_{\odot}$ are shown in Figure 1. We find that the strength of Na I 5897 decreases monotonically with temperature in the range $15,000 \text{ K} < T_{\text{eff}} < 50,000 \text{ K}$. The strength of Ca II K also decreases monotonically over this temperature range, but the equivalent width measurement shown plateaus at $T_{\text{eff}} > 30,000 \text{ K}$ due to the presence of the contaminating transitions mentioned above. The maximum measured line strengths within this temperature range are $W(\text{Ca II K}) = 0.207 \text{ \AA}$ and $W(\text{Na I 5897}) = 0.015 \text{ \AA}$. Moreover, above $T_{\text{eff}} \geq 30,000 \text{ K}$, we measure $W(\text{Ca II K}) \leq 0.074 \text{ \AA}$. We conclude that intrinsic stellar absorption in the Na I 5897 transition is minimal for all stars with $T_{\text{eff}} \geq 15,000 \text{ K}$, while equivalent widths of up to $\approx 0.2 \text{ \AA}$ may be attributed to stellar absorption in the case of Ca II K.

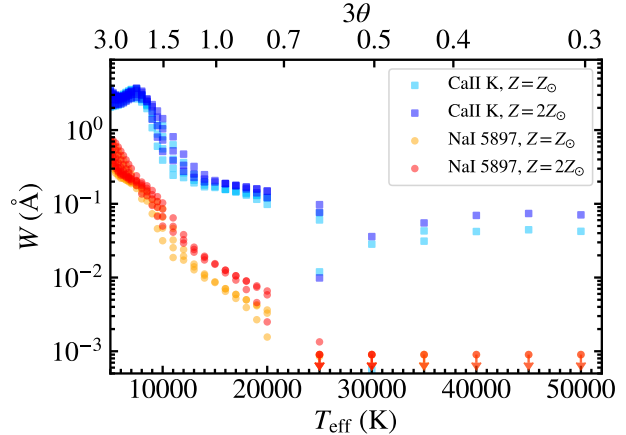


Figure 1. Equivalent widths of the Ca II K (light and dark blue) and Na I 5897 (orange and red) transitions measured from the Rodríguez-Merino et al. (2005) theoretical spectral templates. Measurements for solar-metallicity model spectra are shown in light blue and orange, and measurements for models with twice solar-metallicity are shown in dark blue and red. Measurements that fall below the range in W shown are indicated as upper limits. The scatter in W values at a given T_{eff} and metallicity is due to differences in $\log g$ (which cover the range $0 \leq \log g \leq 5$). The top axis shows the quantity $3\theta = 3 \times 5040 \text{ K}/T_{\text{eff}}$ for reference.

We now proceed with measurement of the absorption strengths of the Ca II K and Na I 5891, 5897 transitions in a subset of the MaStar spectra which have been deemed “high-quality” (i.e., they have high signal-to-noise ratios and relatively high spectral resolution). We focus here on the 29 stars in the high-quality sample with $T_{\text{eff}} > 15,000 \text{ K}$, adopting the median T_{eff} value among stellar parameter estimates computed by four groups within the MaStar team (hereafter $T_{\text{eff,med}}$; Imig et al. 2022; Hill et al. 2022; Lazarz et al. 2022, Y. Chen et al. *in preparation*).² We determine the continuum level of each star by fitting a spline function to feature-free spectral regions close to the transitions of interest using the `1t_continuumfit` GUI, which is part of the `linetools`³ Python package (version 0.3). This tool allows for interactive placement of knots and visual inspection of the resulting spline fit.

We then use the `XAbsSys` GUI, also available with `linetools`, to visually inspect the Ca II K and Na I transitions in each star. In all cases, an absorption feature is evident within $\pm 300 \text{ km s}^{-1}$ of the rest frame.

² We adopt the median stellar parameter values reported in the v2 catalog available at <https://www.sdss4.org/dr17/mastar/mastar-stellar-parameters/>.

³ <https://linetools.readthedocs.io/en/latest/>

We use this GUI to manually select the spectral window to be used to compute the W for each line, and perform this computation using a boxcar sum of the continuum-normalized flux decrement. Spectral regions surrounding these transitions for the ten stars with the highest values of $T_{\text{eff,med}}$ are shown in Figure 2. All exhibit clear Na I absorption, and the vast majority exhibit strong Ca II K absorption. Our W measurements for the full sample of high-quality MaStar stars with $T_{\text{eff,med}} > 15,000$ K are included in Figure 3.

2.2. Establishing the W^{ISM} – Dust Reddening Relation as a Function of Distance

To constrain the relationship between the absorption strength of these transitions and the distance and dust reddening of the star toward which they are observed, we draw on a rich literature of Milky Way ISM studies. Sembach et al. (1993) obtained $\mathcal{R} \sim 68,000$ optical spectroscopy of 57 early-type stars at distances beyond 1 kpc, with the goal of probing interarm regions, Galactic center sightlines, and high latitude directions. They performed Voigt profile fitting of the observed Ca II and Na I absorption troughs, and reported the column densities and Doppler parameters of individual velocity components, in addition to the total W^{ISM} of each system. They determined the color excess of each star ($E(B - V)$) by comparing the intrinsic colors implied by previously published spectral types (Strand 1963) to observed colors, and estimated distances using the spectral type – absolute magnitude relations of Walborn (1972, 1973). They assumed a reddening law with $R_V = A_V/E(B - V) = 3.1$.

We also draw on the sample of 32 O and B stars observed by Munari & Zwitter (1997) at $\mathcal{R} \sim 16,500$. The primary aim of this study was to establish the relation between Na I D and K I line strengths and color excess across a wide range of reddening values. Ca II K did not fall within their spectroscopic coverage. $E(B - V)$ estimates for the sample were adopted from Sūdzius & Bobinas (1994), and distances were computed using the Schmidt-Kaler (1982) absolute magnitude scale. They assumed $R_V = A_V/E(B - V) = 3.2$ when calculating these distances. The total W^{ISM} for each system was reported, along with the W^{ISM} of individual velocity components in multi-component systems.

Finally, we take advantage of the large sample of sightlines studied by Welsh et al. (2010). This work presents $\mathcal{R} > 50,000$ spectroscopy of Na I detected along 482 stellar sightlines, and of Ca II K detected toward 807 sightlines. The authors performed Voigt profile modeling of each of these systems, and then combined these measurements with previously published data to produce a

catalog of absorption toward 1857 early-type stars, all within 800 pc of the Sun. Their analysis reveals a “wall” of Na I-absorbing material at a distance of 80 pc from the Sun, within which only quite weak Na I ($W^{\text{ISM}}(\text{Na I } 5891) < 5 \text{ m}\text{\AA}$) is observed. This finding alone implies that Na I absorption varies significantly over very short distances.

To explore the relationship between W^{ISM} , stellar distance, and reddening in these samples, we first make use of the three-dimensional (3D) Milky Way dust map of Green et al. (2019) to estimate reddening values for the Welsh et al. (2010) stellar sightlines. We use the Python package `dustmaps` (Green 2018) to perform our query. The map returns a reddening E_{DustMap} in arbitrary units designed to be consistent with those used by Schlegel et al. (1998). Here we choose to adjust the $E(B - V)$ values reported in Sembach et al. (1993) and Munari & Zwitter (1997) to the units of E_{DustMap} so that we may report on relationships between W^{ISM} and E_{DustMap} .

To do so, we refer to Lazarz et al. (2022), who established the relation between A_V and E_{DustMap} via an analysis comparing the latter to extinction values derived from stellar spectral template modeling of the MaStar sample. Their relation,

$$A_V = 3.31E_{\text{DustMap}} - 0.076, \quad (1)$$

is consistent with the relation between A_V and $E(g - r)$ derived by Green et al. (2019). We compute the extinction (A_V) implied by the $E(B - V)$ values reported by Sembach et al. (1993) and Munari & Zwitter (1997), adopting $R_V = 3.1$ and 3.2, respectively. We then solve Equation 1 for E_{DustMap} and apply the resulting relation to these two samples.

We then divide all of these literature samples (including that of Sembach et al. 1993, Munari & Zwitter 1997, and Welsh et al. 2010) into several distance bins, and show the relationship between W^{ISM} and E_{DustMap} within each bin in Figure 3 (black filled circles and triangles). There are also numerous sightlines with $E_{\text{DustMap}} < 0.01$ which we exclude from this figure (many of which have $E_{\text{DustMap}} = 0$). Because these sightlines exhibit a broad range of W^{ISM} values that generally fall below 0.1 \AA , we treat them separately and show their cumulative distributions in two bins of Galactic latitude in Figure 4. For completeness, Figure 3 also includes the W^{ISM} values measured from the high-quality MaStar O and B stellar spectra as described in Section 2.1 (magenta squares).

Comparing the distribution of points between the columns of Figure 3, we note that these quantities appear correlated, and that the slope of the relation be-

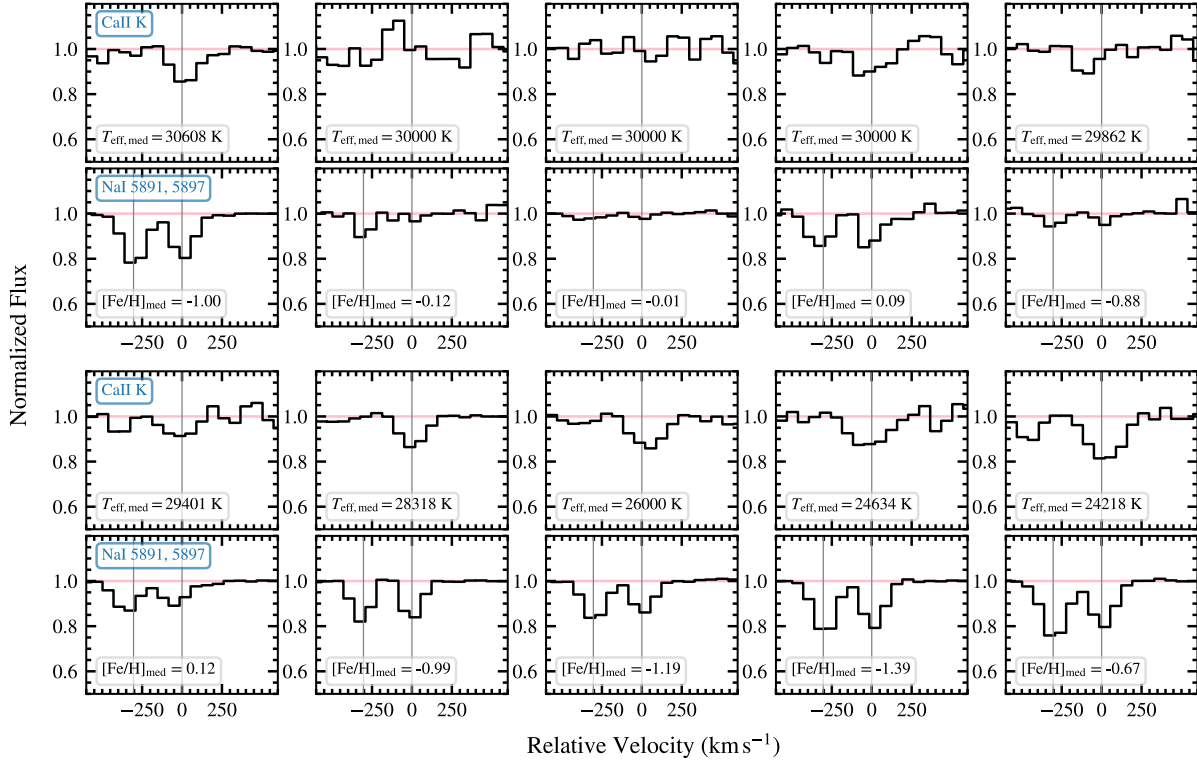


Figure 2. Spectroscopy of the ten stars with the highest $T_{\text{eff,med}}$ in the high-quality MaStar sample. Each pair of stacked panels shows the same spectrum in windows surrounding the Ca II K and Na I $\lambda\lambda 5891, 5897$ transitions on top and bottom, respectively. Velocities are computed relative to the Ca II K $\lambda 3934$ and Na I $\lambda 5897$ rest wavelengths, and the gray vertical lines indicate these transitions along with the relative velocity of $\lambda 5891$. The values of $T_{\text{eff,med}}$ and $[\text{Fe}/\text{H}]_{\text{med}}$ for each star are included in each panel pair.

tween them steepens with increasing distance. We also show the relations between W^{ISM} and $E(B-V)$ reported by Murga et al. (2015, for all transitions) and Poznanski et al. (2012, for the Na I transitions) for extragalactic sightlines with transparent magenta and gray contours.⁴ Most measurements lie below these relations at stellar distances $D < 1$ kpc, while at $D > 1$ kpc, the Na I equivalent widths shown here appear broadly consistent with the Poznanski et al. (2012) relations. The Ca II measurements shown lie below the fitted Murga et al. (2015) relation at $D < 4$ kpc, but come into accord with it at $D > 4$ kpc. We have also examined these relationships by first dividing the sample into bins in E_{DustMap} , and plotting W^{ISM} vs. $\log D$. We find that while W^{ISM} and $\log D$ are indeed correlated at $E_{\text{DustMap}} > 0.05$, the W^{ISM} vs. E_{DustMap} relations exhibit significantly less scatter.

⁴ Both of these works used reddening values obtained from the Schlegel et al. (1998) dust maps ($E(B-V)_{\text{SFD}}$), which have similar units to E_{DustMap} .

To understand the relationships shown in Figure 3 quantitatively, we follow Chen et al. (2010a) and Rubin et al. (2018) to compute the likelihood function for the model

$$W^{\text{ISM}} = \beta + \alpha \log E_{\text{DustMap}} \quad (2)$$

for each transition (Ca II K, Na I 5891, and Na I 5897), with slope α and intercept β . All securely-measured W^{ISM} values contribute $\chi^2/2$ to the logarithm of the likelihood. For non-detections, we integrate the Gaussian contribution to the likelihood from $-\infty$ to the value of the limit (see Rubin et al. 2018 for details). We also assume that the Gaussian variance of each measurement about this model (s_i^2) has contributions from both the W^{ISM} measurement error (σ_i) and intrinsic scatter in the relation (σ_{intr}), such that $s_i^2 = \sigma_i^2 + \sigma_{\text{intr}}^2$. We sample the posterior probability density function (PPDF) for this model using the affine-invariant ensemble Markov Chain Monte Carlo sampler as implemented in the Python software package `emcee` (Foreman-Mackey et al. 2013). We adopt the noninformative priors $-1.4 < \phi = \arctan \alpha < 1.4$,

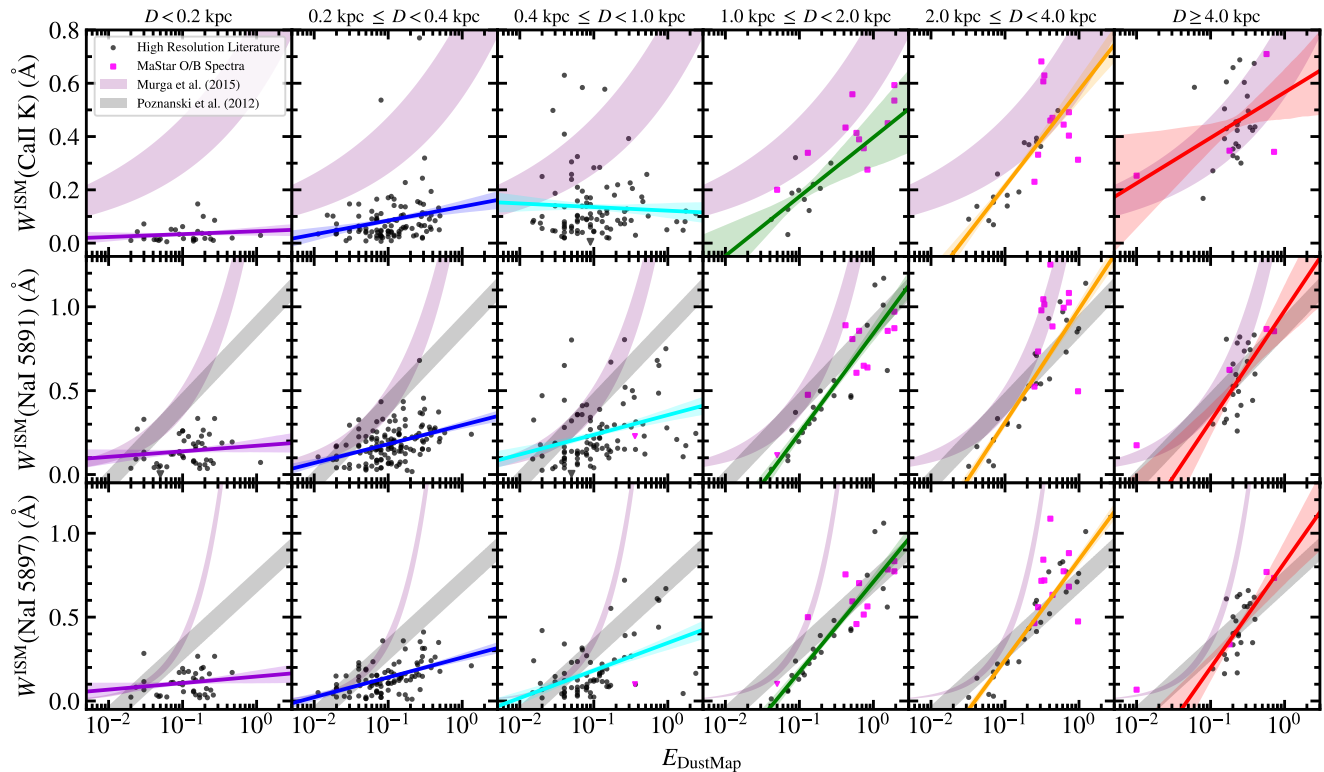


Figure 3. Equivalent widths of interstellar Ca II K (top row), Na I 5891 (middle row), and Na I 5897 (bottom row) vs. E_{DustMap} reported from analysis of high-spectral-resolution stellar spectroscopy by Sembach et al. (1993), Munari & Zwitter (1997), and Welsh et al. (2010). Detections and 2.5σ upper limits (reported by Welsh et al. 2010) are indicated with solid black circles and downward-pointing triangles, respectively. Each column shows measurements of stars with distances within the range specified above the top-most panel. All panels exclude sightlines with $E_{\text{DustMap}} < 0.01$. Magenta squares and triangles indicate detections and upper limits measured from the high-quality MaStar O and B spectral sample. Colored lines show best-fit linear relations between W^{ISM} and $\log E_{\text{DustMap}}$ (see Section 2.2), and the surrounding transparent contours indicate the inner $\pm 34\%$ of the locus of fits drawn randomly from the PPDF of each model. The W ranges indicated by the gray and magenta contours correspond to the ranges in these quantities that are implied by the Poznanski et al. (2012) and Murga et al. (2015) relations and $\pm 1\sigma$ uncertainties, respectively.

$-10 < \beta_{\perp} = \beta \cos(\phi) < 10$, and $-10 < \ln \sigma_{\text{intr}} < 10$ (Robert et al. 2009; VanderPlas 2014). We sample this 3D parameter space with 100 “walkers”, each of which takes 5000 steps in total, and the first 1000 of which are discarded. We adopt the median and ± 34 th-percentile values of marginalized versions of the resulting PPDF as the best value of each parameter and its uncertainty.

The results of this modeling are shown in Figure 3. The solid colored lines indicate the best-fit model for the data shown in the corresponding panel. The transparent contours around each best-fit relation were obtained by drawing 1000 sets of parameters at random from the PPDF, calculating the W^{ISM} implied by those parameters at each point along the x -axis, and then filling in the region containing the inner ± 34 th-percentile values of that W^{ISM} distribution. Our modeling indicates that the slope of the $W^{\text{ISM}} - \log E_{\text{DustMap}}$ relation tends to increase with increasing distance. This steep-

ening is significant for all transitions shown. We list the best-fit parameters of each of these models in Table 1.

Turning our attention to the equivalent widths measured along very low E_{DustMap} sightlines shown in Figure 4, we note that these cumulative distributions tend to shift to higher $\log W^{\text{ISM}}$ values with increasing stellar distance. We also find that while the W^{ISM} distribution of Ca II K absorbers does not appear to vary with Galactic latitude, the subsamples of Na I absorbers close to the disk plane (at $b < 40^\circ$) exhibit higher median $\log W^{\text{ISM}}$ values than those at higher latitudes by $0.3 - 0.5$ dex at $D > 0.1$ kpc. This is consistent with the survival of Ca II in the lower-density, higher-temperature gas ($\sim 1000 - 10,000$ K) above the disk plane (Pusparitani & Lallement 2012), as well as with the findings of, e.g., Sembach & Danks (1994) and Welsh et al. (2010), who measure larger exponential scale heights for the Milky Way’s interstellar Ca II than for Na I.

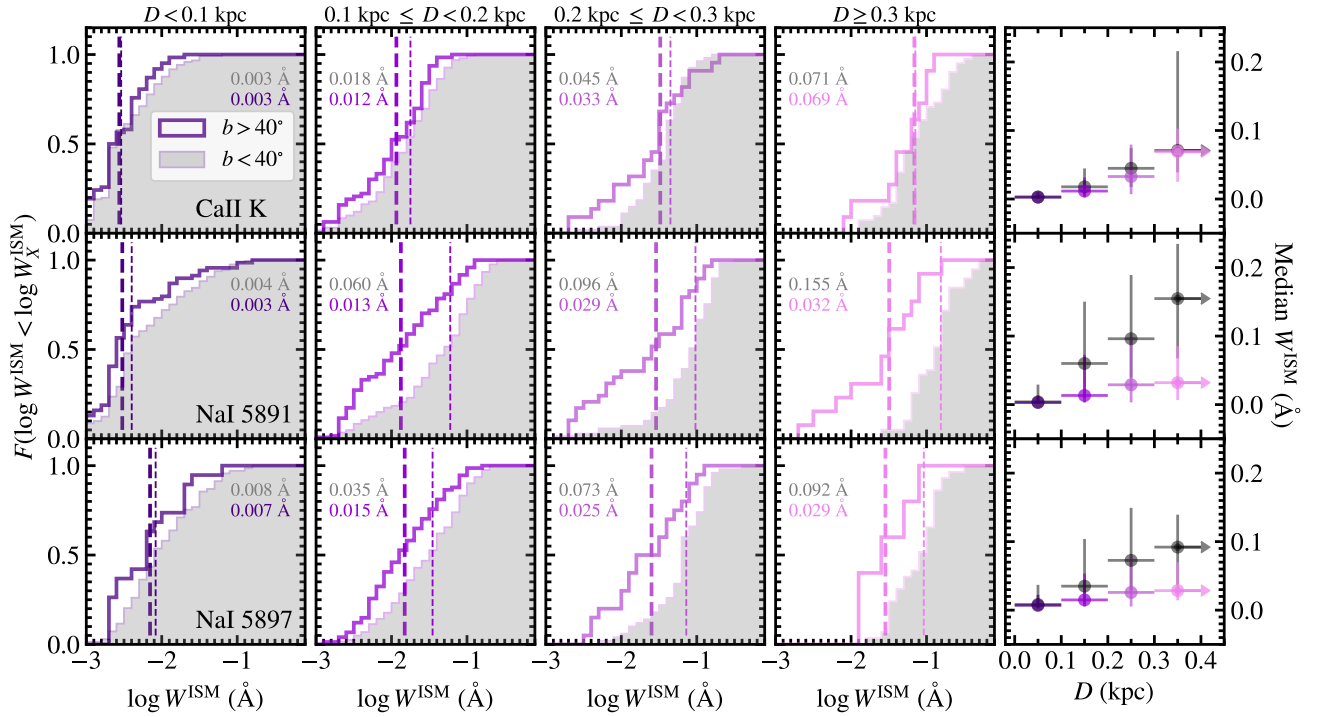


Figure 4. Cumulative distributions of $\log W^{\text{ISM}}$ for interstellar Ca II K (top row), Na I 5891 (middle row), and Na I 5897 (bottom row) for sightlines having $E_{\text{DustMap}} < 0.01$ reported from analysis of stellar spectroscopy by Sembach et al. (1993), Munari & Zwitter (1997), and Welsh et al. (2010). Nondetections are included at the value of their 2.5σ or 3σ upper limits for Welsh et al. (2010) and Sembach et al. (1993) sightlines, respectively. Each column includes measurements of stars with distances within the range specified above the top-most panel. The open histograms with thick outlines include sightlines with high Galactic latitudes ($b > 40^\circ$), while the filled gray histograms include sightlines with $b < 40^\circ$. The median values of these distributions are marked with thick and thin dashed vertical lines, respectively, and are printed on each panel in colored and gray text. The right-most column shows the median W^{ISM} values of each low-latitude (gray) and high-latitude (colored) distribution as a function of distance. Error bars indicate the 16th- and 84th-percentile values of W^{ISM} for the corresponding subsample.

2.3. Implied ISM Absorption Strengths for the MaStar Sample

We now consider the implications of these statistics and models for the stellar sightlines in the MaStar sample. We have found a strong dependence of the absorption strength of interstellar material on both stellar distance and dust reddening. We thus begin by exploring the distributions of these latter quantities as a function of spectral type in the full sample of MaStar targets with high-quality stellar parameter constraints (including 24,162 stars). We adopt T_{eff} ranges for each spectral type as listed in Table 2 and established for main-sequence stars by Habets & Heintze (1981, see their Table 8). Figure 5 shows the frequency distributions of E_{DustMap} values, estimated from the Green et al. (2019) dust maps as described above (top panel), for each of these spectral type categories. The bottom

panel shows the corresponding frequency distributions of stellar distances, for which we adopt the Gaia Early Data Release 3 photogeometric distance estimates of Bailer-Jones et al. (2021). Comparing these distributions among different spectral types, we see that, e.g., the O and B stars have higher median E_{DustMap} values than do the F or G stars in this sample. These differences will be reflected in the distributions of ISM absorption strengths predicted by our modeling.

We then use these E_{DustMap} and stellar distance values (as well as the Galactic latitude for a subset of the stars), in combination with the median W^{ISM} values and best-fit models generated as described above, to compute the implied absorption strength (W^{ISM}) along each stellar sightline. In detail, for those sightlines having $E_{\text{DustMap}} < 0.01$, we simply adopt the median W^{ISM} value of the appropriate literature subsample (drawing from those shown in Figure 4). For sightlines with larger

Table 1. Best-fit Parameters for $W^{\text{ISM}} - \log E_{\text{DustMap}}$ Relations

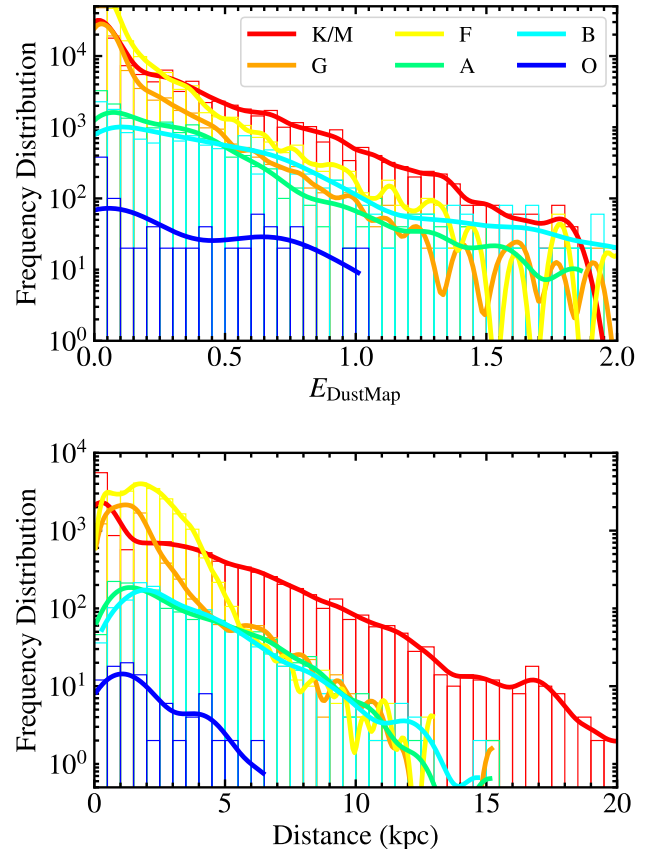
| Transition | Distances (kpc) | α | β | σ_{intr} |
|------------|--------------------|---|------------------|------------------------|
| | | ($\text{\AA} (\log \text{mag})^{-1}$) | (\AA) | (\AA) |
| Ca II K | [0.0, 0.2] | 0.01 ± 0.01 | 0.04 ± 0.02 | 0.03 ± 0.00 |
| | [0.2, 0.4] | 0.05 ± 0.02 | 0.14 ± 0.02 | 0.09 ± 0.01 |
| | [0.4, 1.0] | -0.01 ± 0.03 | 0.12 ± 0.03 | 0.12 ± 0.01 |
| | [1.0, 2.0] | 0.22 ± 0.11 | 0.40 ± 0.11 | 0.08 ± 0.02 |
| | [2.0, 4.0] | 0.36 ± 0.05 | 0.57 ± 0.05 | 0.06 ± 0.01 |
| Na I 5891 | [4.0, 20.0] | 0.17 ± 0.13 | 0.57 ± 0.09 | 0.13 ± 0.02 |
| | [0.0, 0.2] | 0.03 ± 0.04 | 0.17 ± 0.04 | 0.09 ± 0.01 |
| | [0.2, 0.4] | 0.11 ± 0.02 | 0.29 ± 0.02 | 0.10 ± 0.01 |
| | [0.4, 1.0] | 0.12 ± 0.04 | 0.35 ± 0.04 | 0.17 ± 0.01 |
| | [1.0, 2.0] | 0.60 ± 0.06 | 0.84 ± 0.05 | $0.13^{+0.03}_{-0.02}$ |
| Na I 5897 | [2.0, 4.0] | 0.68 ± 0.05 | 0.99 ± 0.04 | 0.11 ± 0.02 |
| | [4.0, 20.0] | $0.66^{+0.25}_{-0.24}$ | 0.98 ± 0.16 | $0.17^{+0.03}_{-0.02}$ |
| | [0.0, 0.2] | 0.04 ± 0.04 | 0.15 ± 0.04 | 0.07 ± 0.01 |
| | [0.2, 0.4] | 0.12 ± 0.02 | 0.26 ± 0.02 | 0.08 ± 0.01 |
| | [0.4, 1.0] | 0.16 ± 0.04 | 0.35 ± 0.04 | 0.14 ± 0.01 |
| K/M | [1.0, 2.0] | 0.54 ± 0.05 | 0.71 ± 0.04 | 0.11 ± 0.02 |
| | [2.0, 4.0] | 0.60 ± 0.04 | 0.84 ± 0.03 | $0.09^{+0.02}_{-0.01}$ |
| | [4.0, 20.0] | 0.63 ± 0.20 | 0.83 ± 0.13 | 0.13 ± 0.02 |

Table 2. Adopted Spectral Type T_{eff} Ranges

| Spectral Type | minimum T_{eff} | maximum T_{eff} |
|---------------|--------------------------|--------------------------|
| O | 29,900 K | ... |
| B | 9700 K | 29,900 K |
| A | 7610 K | 9700 K |
| F | 5950 K | 7610 K |
| G | 5200 K | 5950 K |
| K/M | ... | 5200 K |

amounts of reddening, we apply the appropriate best-fit model to calculate W^{ISM} . The distributions of these values for each transition (again separated by spectral type) are shown in Figure 6. Here, we see that the $W^{\text{ISM}}(\text{Na I})$ values for O and B stars are roughly evenly distributed over the range $0-1 \text{ \AA}$, whereas K/M spectral types have median $W^{\text{ISM}}(\text{Na I})$ values of 0.15 \AA and 0.09 \AA for the 5891 \AA and 5897 \AA transitions, respectively.

In preparation for our effort to reduce the impact of interstellar absorption on the MaStar library, we also consider the detailed distribution of those stars with very low levels of predicted W^{ISM} in stellar parameter space. We make use here of the parameter $\theta = 5040 \text{ K}/T_{\text{eff,med}}$, and will in most cases be considering the quantity 3θ , as it has a very similar dy-

**Figure 5.** *Top:* Frequency distributions of E_{DustMap} values for 23,991 MaStar targets having $E_{\text{DustMap}} \geq 0$, binned by spectral type as indicated in the legend. The smooth curves show continuous probability density curves corresponding to each histogram. *Bottom:* Frequency distributions of stellar distance for the same sample.

namic range to that of both surface gravity ($\log g$) and $[\text{Fe}/\text{H}]$ for this sample. In Figure 7, we show the $\log g$ vs. 3θ distribution of the full MaStar sample (including all stars in the stellar parameter catalog `mastar-goodstars-v3_1_1-v1_7_7-params-v2.fits` with valid parameter entries), divided into 19 bins in the calibrated median $[\text{Fe}/\text{H}]$.⁵ Those stars with predicted $W^{\text{ISM}}(\text{Ca II K}) < 0.05 \text{ \AA}$ and $W^{\text{ISM}}(\text{Na I 5891}) < 0.05 \text{ \AA}$, and which also have well-constrained stellar parameters (with $\sigma_{\theta}/\theta < 0.1$, $\sigma_{\log g} < 1$, and $\sigma_{[\text{Fe}/\text{H}]} < 0.5$), are highlighted in red. This subset includes only 2084 stars and fails to sample much of the

⁵ $[\text{Fe}/\text{H}]$ values are calibrated to those derived by the APOGEE Stellar Parameters and Abundances Pipeline (J. Holtzman et al. *in preparation*) for stars with complementary APOGEE observations as described in <https://www.sdss4.org/dr17/mastar/mastar-stellar-parameters/>.

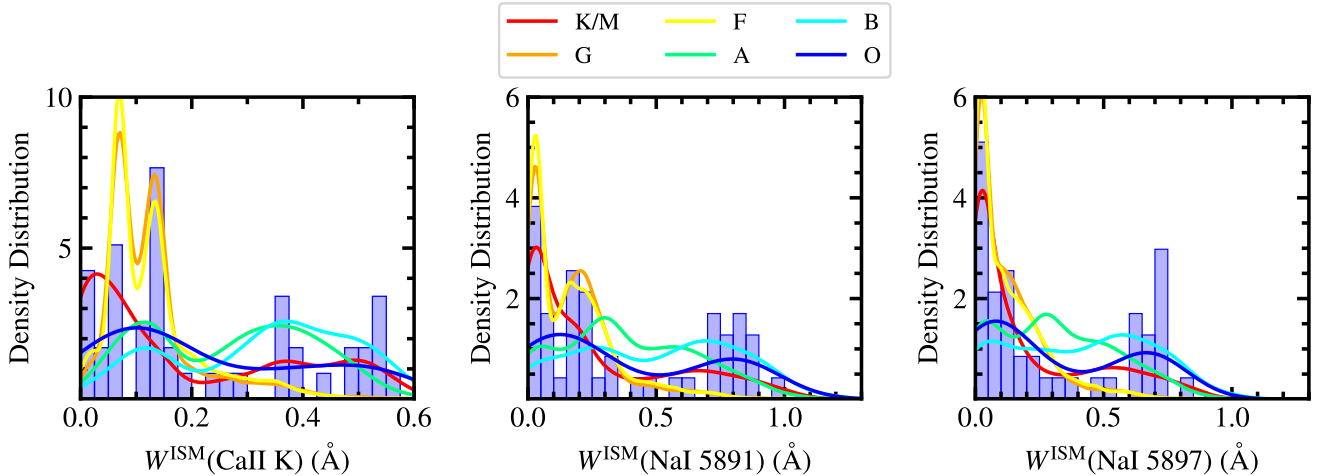


Figure 6. The distribution of equivalent widths arising from interstellar absorption for the MaStar stellar sample, as predicted by the modeling described in Section 2.2. Distributions of $W^{\text{ISM}}(\text{Ca II K})$, $W^{\text{ISM}}(\text{Na I 5891})$, and $W^{\text{ISM}}(\text{Na I 5897})$ values are shown in the left, middle, and right panels, respectively. We show the continuous probability density curves that represent these distributions for all spectral types, and include the corresponding histograms for O-type stars in blue.

$\log g - 3\theta - [\text{Fe}/\text{H}]$ parameter space occupied by the full MaStar sample (and is instead strongly dominated by cool, high-metallicity dwarfs). To improve our sampling of parameter space, we relax our selection criteria to include stars with slightly stronger predicted Ca II K absorption: $W^{\text{ISM}}(\text{Ca II K}) < 0.07 \text{ \AA}$ and $W^{\text{ISM}}(\text{Na I 5891}) < 0.05 \text{ \AA}$. This latter sample is indicated by the combination of cyan and red points, and includes a total of 6408 sightlines. This larger subset covers much of the desired $\log g - 3\theta - [\text{Fe}/\text{H}]$ parameter space, and we therefore choose to adopt these spectra as “low-ISM” sightlines.

Under the assumption that the intrinsic Ca II and Na I profiles of stars with similar stellar parameter values will likely also be very similar on average, we can draw on these “low-ISM” spectra to predict the shape of these intrinsic profiles for much of the remainder of the sample. This approach is similar in spirit to a technique that has been successfully adopted in studies aiming to extract the absorption strength of diffuse interstellar bands from high-resolution stellar spectroscopy (e.g., Kos et al. 2013; Gaia Collaboration et al. 2023a; Vogrinčić et al. 2023); however, here we rely solely on stellar parameters for our intrinsic profile prediction, rather than a minimization of spectral residual differences (Kos et al. 2013). We justify this choice in the following section, and then describe our approach to implementing our intrinsic profile prediction.

3. CORRECTING CA II AND NA I ABSORPTION PROFILES WITH ISM CONTAMINATION

3.1. The Intrinsic Dispersion of Ca II and Na I D Absorption Profiles in Stars with Similar Stellar Parameters

To establish subsamples of stars that have sufficiently similar stellar parameters such that we may consider their Ca II K and Na I D profiles interchangeable, we calculate the 3D distance between every star (i) and all stars in the low-ISM sample (j) as follows:

$$\Psi(i, j) = \left\{ \left(\frac{\log g_i - \log g_j}{\sigma_{\log g_{i,j}}} \right)^2 + \left(\frac{\theta_i - \theta_j}{\sigma_{\theta_{i,j}}} \right)^2 + \left(\frac{[\text{Fe}/\text{H}]_i - [\text{Fe}/\text{H}]_j}{\sigma_{[\text{Fe}/\text{H}]_{i,j}}} \right)^2 \right\}^{1/2},$$

with the values of $\sigma_{\log g_{i,j}}$, $\sigma_{\theta_{i,j}}$, and $\sigma_{[\text{Fe}/\text{H}]_{i,j}}$ equal to the corresponding uncertainties on the parameters of the two stars (i, j) added in quadrature. For each star i , we find the minimum value of this distance across all j sightlines, $\Psi_{\min}(i)$. In Figure 8, we show the same distributions of stellar parameters as in Figure 7, and have color-coded each star by this latter value. Among the 24,162 stars shown here, 55% have $\Psi_{\min} < 0.2$, while just 8% (1819) have $\Psi_{\min} > 1.0$. This latter subset tends to either exhibit high effective temperatures (with $3\theta < 2$), or to be located toward the tip of the red giant branch. The maximum value of Ψ_{\min} among our sample is 9.4. This analysis indicates that it is important to assess the scatter in the intrinsic Ca II and Na I D line profiles of stars having 3D parameter distances in the range $0 < \Psi \lesssim 2$ in order to determine whether our

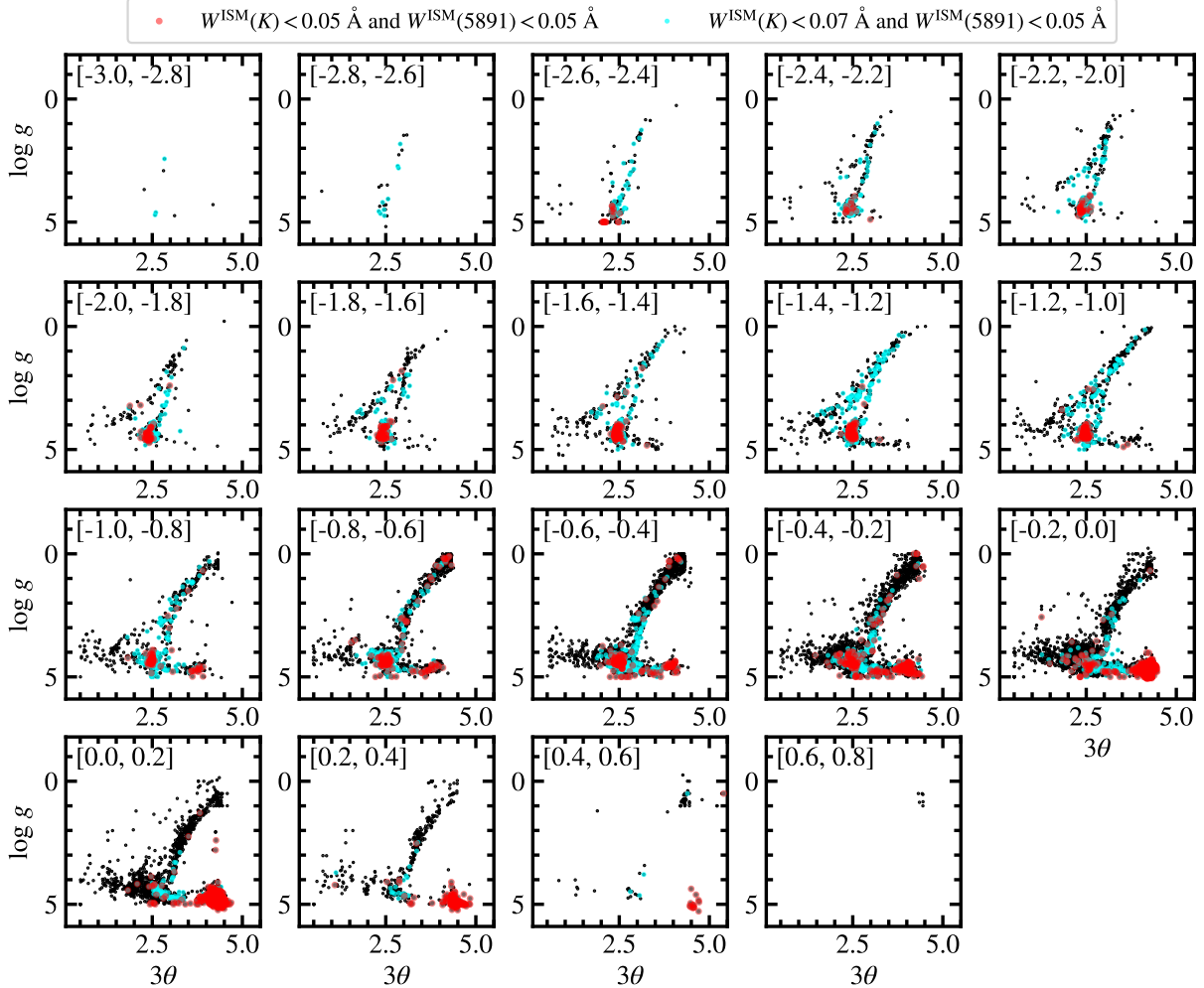


Figure 7. Stellar parameter distributions for the $\approx 24,000$ unique stars in the MaStar sample (black). Each panel shows objects having $[\text{Fe}/\text{H}]$ values between those listed at the top left. Red points indicate those stars with predicted ISM absorption strengths $W^{\text{ISM}}(\text{Ca II K}) < 0.05 \text{ \AA}$ and $W^{\text{ISM}}(\text{Na I 5891}) < 0.05 \text{ \AA}$. The combination of cyan and red points shows stars with $W^{\text{ISM}}(\text{Na I 5891}) < 0.05 \text{ \AA}$ and $W^{\text{ISM}}(\text{Ca II K}) < 0.07 \text{ \AA}$. The latter set of stars samples much of this parameter space well; however, they are rare among hot stars ($3\theta < 2$), and are sparse along the red giant branch at solar and supersolar metallicities.

low-ISM sightlines may be used to predict these profiles across the full MaStar sample.

To make this assessment, we first choose nine locations in this parameter space that are approximately representative of the parameter ranges exhibited by the full sample. These locations are indicated with black squares in Figure 8. We then identify all low-ISM stars having parameters that fall within a distance $\Psi < \Psi_{\text{thresh}}$ of each location, where we set $\Psi_{\text{thresh}} = 0.2, 0.4, 0.6, 0.8, 1.0, 1.2,$ and 1.5 in successive iterations of this exercise.

Then, for each location and each value of Ψ_{thresh} , we compute the average of all selected low-ISM spectra. For this analysis, and for all analyses to follow, we use the MaStar spectra which have been smoothed to a uniform line spread function (LSF) representative of the 99.5th

percentile of the native LSFs across the survey. To coadd our spectral subsamples, we use the following approach:

1. We first normalize each spectrum by its mean value, and then compute their median S/N-weighted average as a function of wavelength (shown in panels (a) and (e) in Figure 9 for subsamples ‘3’ and ‘7’ constructed using $\Psi_{\text{thresh}} = 0.4$).
2. To reduce dispersion in the coadded sample due to slight differences in overall continuum shape, we divide each normalized spectrum by this coadd, and fit fourteenth-order Legendre polynomials to the results. These polynomial models are shown in panels (b) and (f) of Figure 9. Any objects with

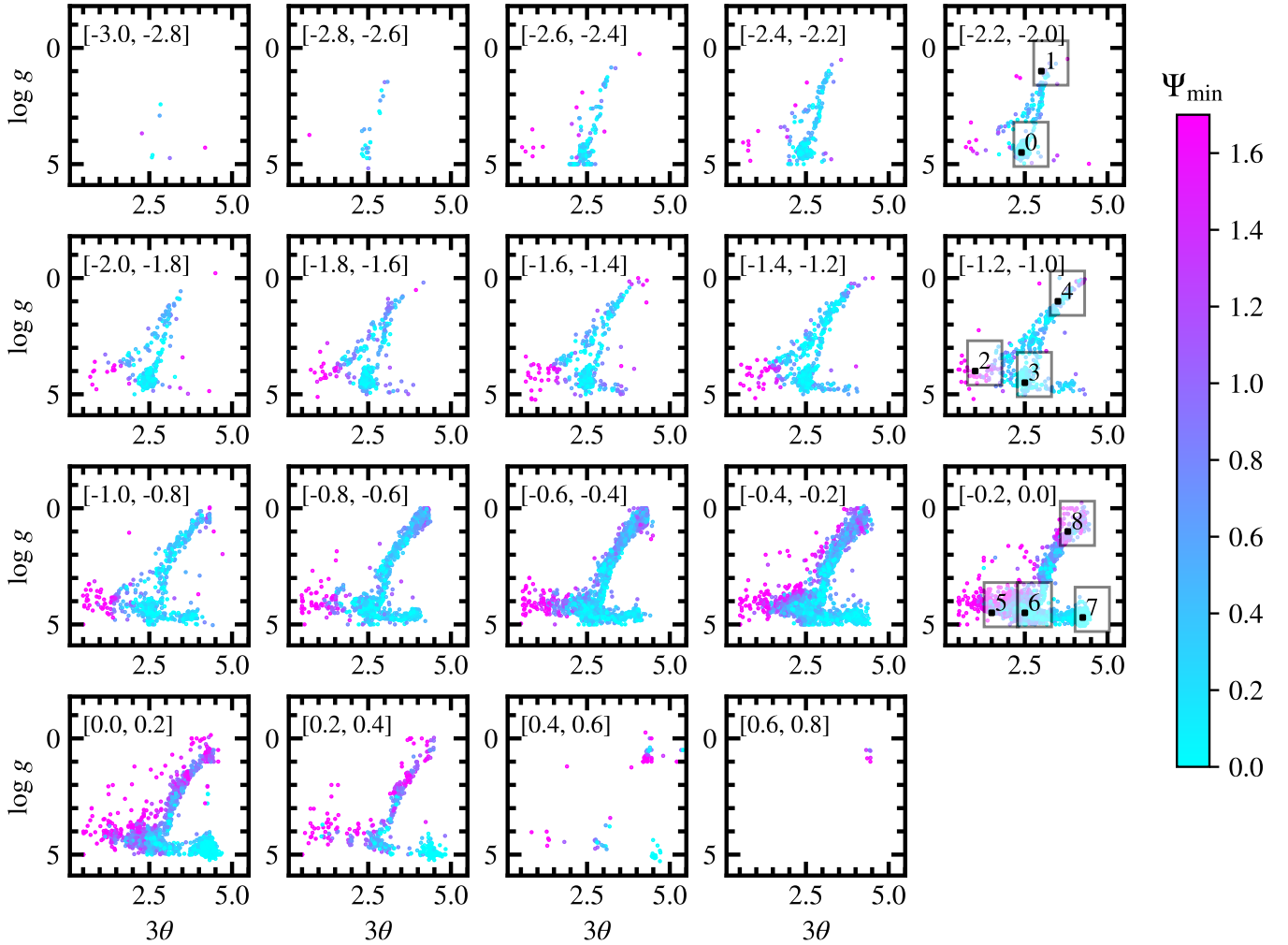


Figure 8. Stellar parameter distributions for the full MaStar sample. Each panel shows objects having $[\text{Fe}/\text{H}]$ values between those listed at the top left. Stars are color-coded by Ψ_{\min} , a measure of their distance in this parameter space from the nearest low-ISM sightline. The black squares labeled with integers in the right-most column indicate the locations in parameter space chosen to investigate the intrinsic scatter in Ca II and Na I D profiles as described in Section 3.1.

model values > 2 or < 0.5 are considered outliers and are removed from the subsample.

3. We renormalize each spectrum by its fitted Legendre polynomial, and re-construct their average as described above (shown in panels (c) and (g) in Figure 9).

We additionally compute the uncertainty in this final coadd via propagation of the errors in the individual spectra (σ_{prop}), shown in blue in panels (d) and (h) of Figure 9, as well as the median S/N-weighted standard deviation of the flux across all spectra (σ_{coadd}), shown in red in the same panels.

We then measure the equivalent widths and associated uncertainties of the Ca II K and Na I D features in the resulting sample of coadds. To do so, we choose relatively feature-free spectral regions on either

side of each profile in order to establish the continuum level (in the ranges $3920.0 \text{ \AA} < \lambda < 3925.0 \text{ \AA}$ and $3945.0 \text{ \AA} < \lambda < 3950.0 \text{ \AA}$ around Ca II K; and in the ranges $5881.0 \text{ \AA} < \lambda < 5885.0 \text{ \AA}$ and $5904.0 \text{ \AA} < \lambda < 5908.0 \text{ \AA}$ around Na I D). We fit a linear model to the flux across these pixels, and use this model to locally continuum-normalize these spectral regions. We then compute a boxcar equivalent width in the spectral window $3925.0 \text{ \AA} < \lambda < 3944.0 \text{ \AA}$ to measure the strength of Ca II K ($W_{\text{coadd}}(\text{Ca II K})$), and in the spectral window $5885.0 \text{ \AA} < \lambda < 5904.0 \text{ \AA}$ to measure the total strength of both transitions in the Na I D doublet ($W_{\text{coadd}}(\text{Na I D})$). We likewise compute the uncertainty in these line strengths arising from the deviation in the flux profiles across each subsample ($\sigma_{W, \text{coadd}}$, calculated from σ_{coadd}).

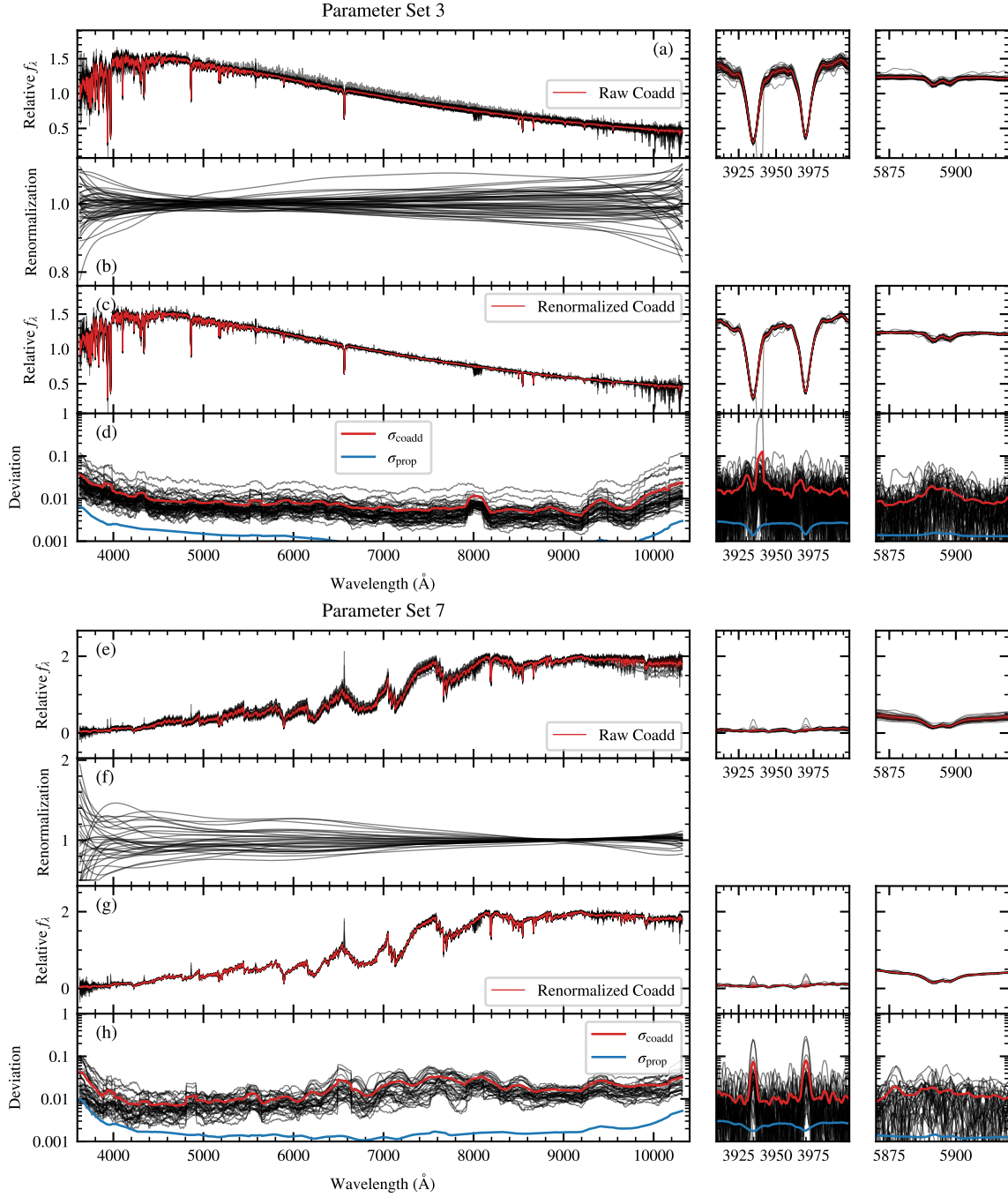


Figure 9. Demonstration of our spectral coadding algorithm for stars selected within $\Psi_{\text{thresh}} = 0.4$ of the parameter locations labeled ‘3’ (rows (a)-(d)) and ‘7’ (rows (e)-(h)) in Figure 8. The right-hand columns show the Ca II and Na I D regions of the spectra shown at left. (a,e) Spectra of all stars selected for this coadd, normalized by their mean flux values, are shown in black. The average of these spectra, weighted by their median S/N, is shown in red. (b,f) Fourteenth-order Legendre polynomial fits to the ratio of each normalized spectrum to the coadd shown above. (c,g) Same as panels (a,e) for individual spectra renormalized by their Legendre polynomial fits and then coadded in the same manner. (d,h) The absolute deviation of each renormalized spectrum from the final coadd is shown in black. The uncertainty in the final coadd calculated via propagation of the individual spectral error arrays is shown in blue, and the total dispersion in the renormalized flux values from the final coadd is shown in red.

We show these results in Figure 10. The left-hand panels show the W_{coadd} measured in each spectral coadd as a function of Ψ_{thresh} . The point sizes indicate the number of spectra included in the coadd (see legend at upper right). Symbols that are not connected by a colored line represent the equivalent width measured in the individual spectrum of the star closest to the appropriate parameter space location, and are included only in cases in which there are no other stars meeting the $\Psi < \Psi_{\text{thresh}}$ criterion (such that we cannot construct a coadd). Error bars indicate $\sigma_{W,\text{coadd}}$.

Broadly speaking, these equivalent width values do not change significantly with increasing Ψ_{thresh} . The $W_{\text{coadd}}(\text{Ca II K})$ values of all but one of the coadds of sets 0, 2, 3, 4, 5, 6, and 8 differ from the corresponding equivalent width value shown at $\Psi_{\text{thresh}} = 0.2$ by $\leq 2.2\sigma$. The spectra of the solar-metallicity cool dwarf stars in parameter set 7 exhibit only very weak emission in this spectral region and lack well-defined Ca II profiles. The coadds of parameter set 1 exhibit Ca II K equivalent width differences of $0.2 - 0.4 \text{ \AA}$ (at $1.9\sigma - 4.0\sigma$ significance) relative to that of the closest individual spectrum; however, the equivalent widths of the five coadds shown are consistent with each other within $< 1.2\sigma$.

Na I D exhibits similar behavior: the equivalent width values of sets 0, 1, 2, 3, 4, 5, 6 and 7 are all within 2.4σ of the equivalent width shown at $\Psi_{\text{thresh}} = 0.2$. Set 8 exhibits modestly more significant differences of $0.8\sigma - 2.9\sigma$. However, we note that the spectra of stars in parameter set 8 lack a well-defined Na I D profile and are dominated by molecular absorption bands.

The right-hand panels of Figure 10 show the ratio $\sigma_{W,\text{coadd}}/W_{\text{coadd}}$ for the Ca II K (top) and Na I D (bottom) profiles in each of these spectral stacks. Here, we have not included equivalent width measurements of individual spectra, and also exclude negative equivalent width measurements (which arise for Ca II K in set 7). In general, we see that this ratio tends to increase weakly with increasing Ψ_{thresh} , but that it remains $\lesssim 0.2$ in most cases. The coadds in set 8 are exceptions to these rules: in particular, the equivalent width of Ca II K exhibits a scatter well above $> 1 \text{ \AA}$ at $\Psi_{\text{thresh}} > 1.0$, implying significant inconsistency in these line profiles.

In summary, we find that the coadded spectra of stars with stellar parameters that differ by Ψ_{thresh} values between 0.2 and 1.0 exhibit statistically consistent Ca II K and Na I D equivalent widths. The dispersion in these equivalent width values ($\sigma_{W,\text{coadd}}$) arising from differences in absorption profile shapes within each coadd is $< 20\%$ in most subsamples. Moreover, this dispersion is typically minimized at lower values of Ψ_{thresh} . These findings imply that we may use the Ca II and Na I D pro-

files of our low-ISM sample to replace those in stars with greater predicted foreground ISM absorption in cases in which we are able to identify low-ISM sightlines that are sufficiently close in stellar parameter space.

3.2. Empirical Spectral Replacement

We now use the findings laid out above to identify subsamples of low-ISM stellar sightlines that may be coadded to replace the relevant spectral regions for every star with $W^{\text{ISM}}(\text{Ca II K}) > 0.07 \text{ \AA}$ or $W^{\text{ISM}}(\text{Na I 5891}) > 0.05 \text{ \AA}$ in the MaStar sample. For each such star, we first search for all low-ISM sightlines having $\Psi < 0.2$. If there are 10 or more low-ISM stars meeting this criterion, we consider this our “final” replacement subsample. If there are fewer than 10 stars, we increase Ψ_{thresh} in increments of 0.1 until either (1) the subsample includes at least 10 stars or (2) $\Psi_{\text{thresh}} = 0.6$. If the $\Psi_{\text{thresh}} = 0.6$ subsample includes at least five stars, we consider them our “final” replacement subsample. If it includes fewer than five stars, we continue to increase Ψ_{thresh} in increments of 0.1 until (1) the subsample includes at least five stars or (2) $\Psi_{\text{thresh}} = 1.0$. If there is a minimum of one star within $\Psi < \Psi_{\text{thresh}} = 1.0$, we use that sample as our “final” replacement subsample. If there are no stars within $\Psi < 1.0$, then we do not attempt a spectral replacement. Among the 23,771 stars with high-quality parameter values and available spectra, there are 6342 low-ISM sightlines, and 15,661 stars for which we were able to construct a replacement subsample in the manner described above. This leaves 1768 stars with potentially high levels of ISM contamination that cannot be removed via this method. This latter sample corresponds to those stars shown in magenta in Figure 8.

For each of the 15,661 stars for which “empirical replacement” is possible (referred to below as “primary” stars), we first coadd the spectra of all stars in the corresponding replacement subsample in the same manner described in Section 3.1. We then normalize the spectrum of the primary star by its mean value. We divide this normalized spectrum by the initial spectral coadd (described in Step 2 above), and fit a fourteenth-order Legendre polynomial to the resulting spectral ratio. We then renormalize the primary spectrum by this model so that its continuum level is well-matched to that of the final coadd. We perform the complementary manipulations of the inverse variance, first multiplying it by the square of the mean value of the primary spectrum, and then by the square of the Legendre polynomial fit.

We then replace the spectral regions $3912.0 \text{ \AA} < \lambda < 3995.0 \text{ \AA}$ and $5873.0 \text{ \AA} < \lambda < 5917.0 \text{ \AA}$ in the primary spectrum with the same regions in the coadd. These

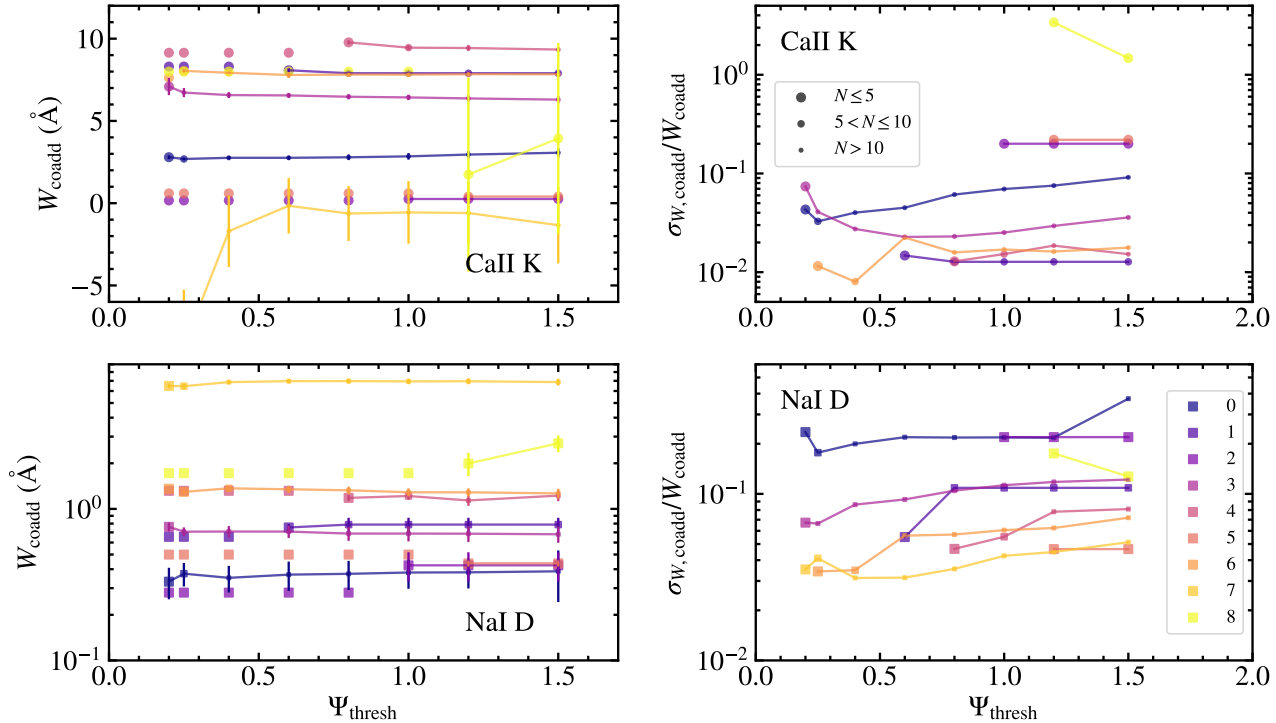


Figure 10. *Left panels:* The equivalent width of the Ca II K (top) and Na I D (bottom) transitions in the spectral coadds described in Section 3.1 as a function of Ψ_{thresh} (with Ψ representing the 3D parameter space distance from the parameter space location of each coadd). Points are color-coded according to their location in parameter space as indicated in the legend at bottom right. The size of each point corresponds to the number of spectra in the coadd, as indicated by the legend in the upper right panel. Symbols that are not connected by lines represent the equivalent width measured in the individual spectrum closest to the corresponding parameter space location. Error bars indicate the uncertainty in W_{coadd} ($\sigma_{W_{\text{coadd}}}$) due to the deviation in the flux levels across the subsample. *Right panels:* The ratio $\sigma_{W_{\text{coadd}}}/W_{\text{coadd}}$ for Ca II K (top) and Na I D (bottom). Points are color-coded and sized as in the left-hand panels. The dispersion in flux levels across these absorption profiles gives rise to a $\lesssim 10 - 20\%$ uncertainty in their equivalent widths in the vast majority of the coadds included here.

windows are chosen to encompass both Ca II H & K and Na I D in stars in which these profiles are very broad. To avoid sharp features at the edges of these regions, we adopt a weighted sum of the primary and coadded spectra. The primary spectrum is weighted by the amplitude of the sum of two Gaussian functions ($G(\lambda)$): one Gaussian is centered at the left edge of the spectral window, and the other is centered at the right edge. Both Gaussians are assigned dispersions $\sigma = 3 \text{ \AA}$, such that $G(\lambda) = 0$ across much of the window. The coadded spectrum is weighted by $1 - G(\lambda)$.

After performing this replacement, we multiply the entire primary spectrum by its Legendre polynomial fit, as well as by its mean value, and have verified that this procedure returns all pixels outside of the Ca II and Na I D spectral windows to their original flux levels. The renormalized variance of the primary star spectrum is likewise replaced with a sum of the square of the weighted σ_{coadd} array and the variance array itself. The resulting inverse variance is then divided by the square of the Legendre

polynomial fit, and again by the square of the mean value of the primary spectrum.

In the case that the replacement subsample includes only one star, we simply adopt its flux and inverse variance (normalized by its mean value) as that used to replace the relevant spectral regions in the primary star. We again apply the Gaussian tapering function described above to smooth the transition from one spectrum to the other. We ensure the stars have comparable continuum shapes by fitting a Legendre polynomial to their ratio, and renormalizing the primary spectrum by this model (as described above).

We assess the results of this procedure by first measuring the equivalent widths of the relevant transitions in the original spectra (W_{orig}) and in the spectra that have been “cleaned” via replacement with a coadd (W_{coadd}), using the same spectral windows and approach to continuum fitting as described in Section 3.1. We then compute the difference $\Delta W = W_{\text{orig}} - W_{\text{coadd}}$ for each star. In Figure 11, we show the distributions of these

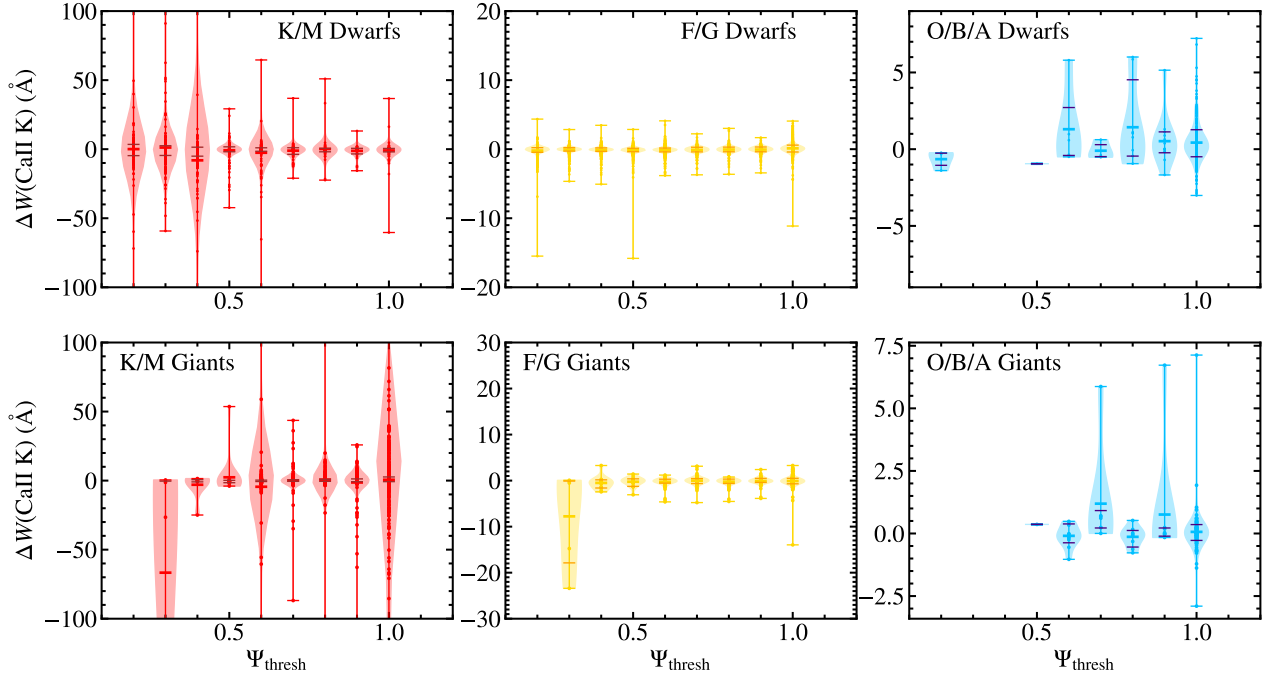


Figure 11. The distributions of the change in the Ca II K equivalent width in spectra “cleaned” with a replacement coadd relative to the original stellar spectra ($\Delta W = W_{\text{orig}} - W_{\text{coadd}}$) as a function of Ψ_{thresh} . Only sightlines that are not considered “low-ISM” and for which we can construct replacement coadds are included. The mean value of each distribution is indicated with a matching red, yellow, or light blue horizontal bar, and the minimum and maximum values correspond to the extremes for each subsample. The widths of the filled contours scale with the frequency of the data along the y -axis. The 16th- and 84th-percentile values are shown with horizontal bars of a complementary color. Stars have been grouped according to their location in $T_{\text{eff}} - \log g$ space, with dwarf and giant stars having $\log g > 4$ and $\log g < 4$, respectively.

values for the Ca II K transition as a function of Ψ_{thresh} , excluding those stars in the “low-ISM” subsample. Each panel includes stars in a different region of $\log g - T_{\text{eff}}$ space: the top three panels include dwarf stars with $\log g > 4$ at cool ($T_{\text{eff,med}} < 5200$ K), medium (F/G; 5200 K $< T_{\text{eff,med}} < 7610$ K), and hot (O/B/A; $T_{\text{eff,med}} > 7610$ K) temperatures, and the bottom three panels include giant stars with $\log g < 4$ in the same temperature categories. We find that the $\Delta W(\text{Ca II K})$ distributions for cool dwarfs and giants are very broad even at $\Psi_{\text{thresh}} < 0.5$, with numerous catastrophic failures resulting in $\Delta W(\text{Ca II K})$ values of $\approx \pm 50 - 100$ Å. Medium and hot stars overall have significantly more narrow $\Delta W(\text{Ca II K})$ distributions, but nevertheless include a handful of spectra with $|\Delta W(\text{Ca II K})| > 3$ Å, which is unlikely to arise from ISM contamination. We also note that the averages of these distributions (indicated by the red, yellow, and light blue horizontal dashes) are not systematically > 0 Å for either cool- or medium-temperature stars.

Figure 12 shows the same set of distributions for the Na I D doublet. These distributions all have much

smaller dispersions than the analogous Ca II K distributions, and for medium-temperature and hot stars, have mean values > 0 Å. We also note that the incidence of catastrophic failures (with $\Delta W(\text{Na I D}) < -1$ Å) increases sharply at $\Psi_{\text{thresh}} = 1$ in several of these subsamples.

We next show the distributions of these values as a function of the spectral type in Figure 13. Here again, only those stars for which a replacement coadd may be constructed and that are not “low-ISM” sightlines are included. We have also excluded all sightlines for which coadds were constructed adopting a $\Psi_{\text{thresh}} = 1.0$ to reduce the incidence of catastrophic failures in our empirical replacement sample. The second and fourth panels from the left in this figure do not include histograms for O-type stars, as there are no such stars that satisfy all of these criteria.

Even having excluded those coadds with $\Psi_{\text{thresh}} = 1.0$, the mean $\Delta W(\text{Ca II K})$ for our K/M and G samples are -0.6 Å and -0.2 Å, and is very close to zero for F types. The A and B spectral type distributions have means of 0.3 Å and 3.2 Å, respectively. We have also looked

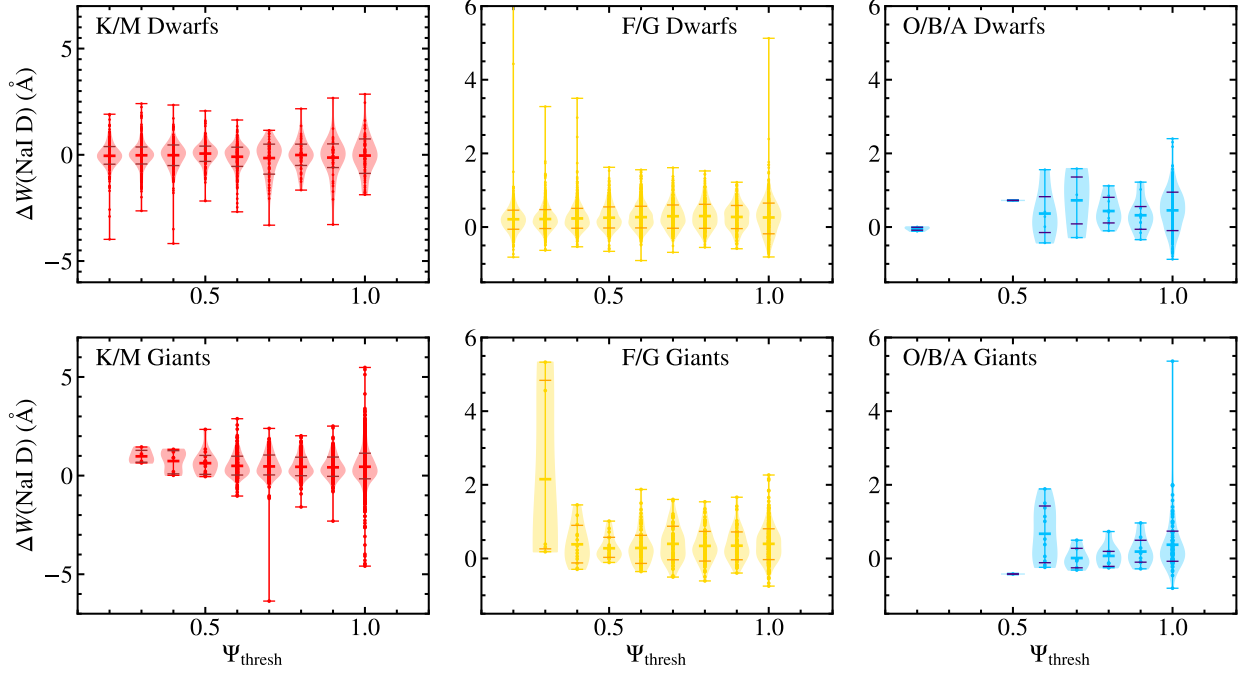


Figure 12. Same as Figure 11, for Na I D.

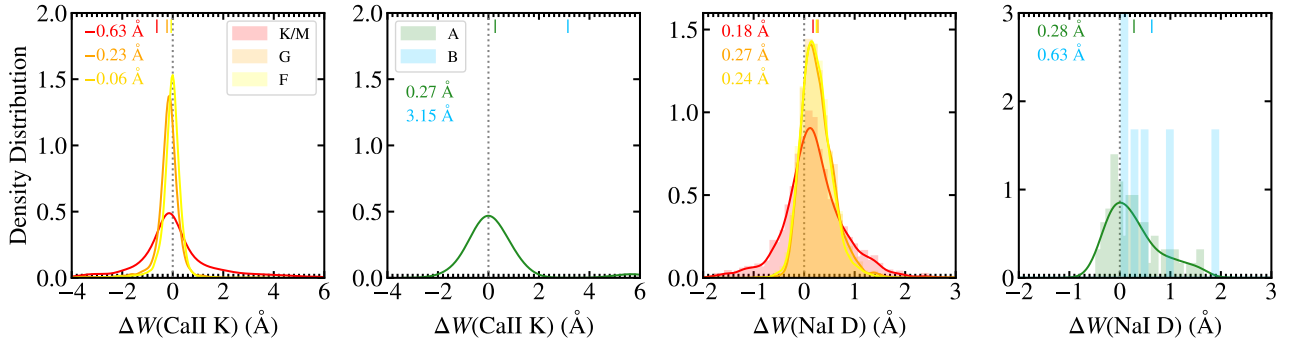


Figure 13. The distributions of the change in Ca II K (left-hand panels) and Na I D (right-hand panels) equivalent widths in spectra “cleaned” with a replacement coadd relative to the original stellar spectra ($\Delta W = W_{\text{orig}} - W_{\text{coadd}}$). Only sightlines that are not considered “low-ISM” and for which we can construct replacement coadds with $\Psi_{\text{thresh}} < 1.0$ are included. Distributions are color-coded by spectral type as indicated in the legend. The smooth curves show continuous probability density distributions corresponding to each histogram. The average value of each distribution is printed and indicated toward the top of each panel with a bar of the corresponding color.

closely at sightlines that are outliers in the A- and B-star distributions at $\Delta W(\text{Ca II K}) > 4 \text{ \AA}$, for which the original spectrum exhibits a much stronger K transition relative to that of its replacement coadd than could arise from ISM contamination. We posit that this scenario arises because Ca II H & K are particularly sensitive to temperature at $T_{\text{eff}} \approx 10,000 \text{ K}$ (see Figure 1), with the K transition decreasing in strength from $\approx 2.0 \text{ \AA}$ to 0.2

\AA over the T_{eff} range from 8000 K to 12,000 K. Moreover, the median and maximum uncertainties on $T_{\text{eff,med}}$ for stars in this temperature range are 316 K and 7861 K, respectively, meaning that the low-ISM stars satisfying our Ψ_{thresh} criteria may in some cases have temperatures spanning this range.

The distributions showing the change in the Na I D absorption strength indicate that its equivalent width

has been reduced in the vast majority of the cleaned spectra. The mean value of $\Delta W(\text{Na I D})$ falls in the range $0.2 - 0.3 \text{ \AA}$ for K/M, G, and F stars, and is 0.3 \AA and 0.6 \AA for A and B stars, respectively. This trend is qualitatively consistent with the predictions shown in Figure 6.

3.3. Spectral Replacement with Theoretical Stellar Templates

We now consider an alternative approach to removing ISM contamination from these sightlines. This is of particular importance for those stars that are isolated in parameter space, such that no replacement subsample could be identified. From examination of Figure 8, it is evident that many of these stars have high effective temperatures (i.e., $3\theta < 2$ with $T_{\text{eff,med}} > 7560 \text{ K}$). Such O, B, and A stars will dominate stellar continuum models of strongly star-forming galaxies, along with any extant absorption due to foreground Milky Way ISM. Moreover, the analysis presented in Figure 6 demonstrates that these hot stars are likely subject to the strongest ISM contamination among all stars in the MaStar sample, as they tend to exhibit a high degree of reddening overall (see also Figure 5).

At the same time, theoretical modeling of the atmospheres of stars in this temperature range is not subject to complications arising from significant line blanketing and the interplay of molecular opacities (e.g., Bohlin et al. 2017; Byrne & Stanway 2023). We therefore choose to explore the intrinsic Ca II and Na I D profiles predicted from model stellar atmospheres for all stars having $T_{\text{eff,med}} > 7,500 \text{ K}$.

Bohlin et al. (2017) have computed and made public a large suite of stellar spectra predicted using the ATLAS-APOGEE ATLAS9 model atmosphere database (Mészáros et al. 2012). The suite is generated from a grid of models covering the temperature range $3500 \text{ K} \leq T_{\text{eff}} \leq 35,000 \text{ K}$, a metallicity range $-2.5 \leq [\text{M}/\text{H}] \leq 0.75$, a range in α abundance of $-0.25 \leq [\alpha/\text{M}] \leq 0.5$, and a range in carbon abundance of $-0.75 \leq [\text{C}/\text{M}] \leq 0.25$. The resulting spectra cover a wavelength range of $1000 \text{ \AA} < \lambda < 32\mu\text{m}$ at a native resolution $\mathcal{R} = 300,000$. Bohlin et al. (2017) demonstrated that χ^2 minimization of the residuals between this model spectroscopy and that of the CALSPEC standard stars yields low values in the range $\chi^2 = 0.1 - 3$, and yields best-fit T_{eff} values that are fully consistent with those based on the models of Castelli & Kurucz (2003).

We retrieve the subset of these theoretical spectra that were generated from model atmospheres with $T_{\text{eff}} \geq 7500 \text{ K}$ and that have been smoothed to a resolution

$\mathcal{R} = 2000$ from the MAST archive.⁶ The T_{eff} and $\log g$ sampling of this portion of the grid of models is variable, with the range $7500 \text{ K} \leq T_{\text{eff}} \leq 8000 \text{ K}$ sampled in increments of 250 K with surface gravities over the range $1 \leq \log g \leq 5$ in increments of 0.5 . The temperature range $8250 \text{ K} \leq T_{\text{eff}} \leq 12,000 \text{ K}$ is sampled in increments of 250 K with surface gravities over the range $2 \leq \log g \leq 5$ in increments of 0.5 . The temperature range $12,500 \text{ K} \leq T_{\text{eff}} \leq 20,000 \text{ K}$ is sampled in increments of 500 K at $\log g = 3.0, 3.5, 4.0, 4.5$, and 5.0 , and the temperature range $21,000 \text{ K} \leq T_{\text{eff}} \leq 30,000 \text{ K}$ is sampled in increments of 1000 K at $\log g = 4.0, 4.5$, and 5.0 . Together, these comprise 246 grid points in T_{eff} and $\log g$. We make use of models across the full range in metallicity and α -abundance listed above, but consider only those with $[\text{C}/\text{M}] = 0$. With both the aforementioned metallicity and α -abundance ranges sampled in increments of 0.25 dex , the nominal size of the grid of theoretical spectra we consider is $246 \times 13 \times 4 = 12792$. In practice, there are additional models available from MAST that range in temperature up to $35,000 \text{ K}$, but that are not described in Bohlin et al. (2017). Considering these additions, we make use of 13,466 models in total.

To match each of the hot MaStar stars requiring “cleaning” with the appropriate model stellar spectrum, we use the APOGEE-calibrated values of $[Z/\text{H}]_{\text{med}}$ and $[\alpha/\text{Fe}]_{\text{med}}$ available from the MaStar stellar parameter catalog to compute $[\alpha/Z]_{\text{med}} = [\alpha/\text{Fe}]_{\text{med}} + [\text{Fe}/\text{H}]_{\text{med}} - [Z/\text{H}]_{\text{med}}$. For each star, we then compute the Euclidean distance between its values of $3\theta, \log g_{\text{med}}, [Z/\text{H}]_{\text{med}}$, and $[\alpha/Z]_{\text{med}}$, and the values of $3\theta, \log g, [\text{M}/\text{H}]$, and $[\alpha/\text{M}]$ at each model grid point. We select the model with the minimum value of this distance as our “replacement” spectrum.

We use the function `match_spectral_resolution` available as part of the MaNGA Data Analysis Pipeline Python package⁷ (Westfall et al. 2019) to smooth the model spectra to the observed spectral resolution, and then rebin the smoothed spectra to match the pixel sampling of the MaStar stars. We continuum-normalize each model and corresponding observed spectrum in a similar manner to that described in Section 3.2, fitting a Legendre polynomial to their ratio, and then dividing the MaStar spectrum by the polynomial model. We replace the spectral regions $3912.0 \text{ \AA} < \lambda < 3990.0 \text{ \AA}$ and $5873.0 \text{ \AA} < \lambda < 5917.0 \text{ \AA}$ in the data with the resampled, smoothed model spectrum, again weighting by a

⁶ <https://archive.stsci.edu/prepds/bosz/>

⁷ <https://sdss-mangadap.readthedocs.io/en/latest/>

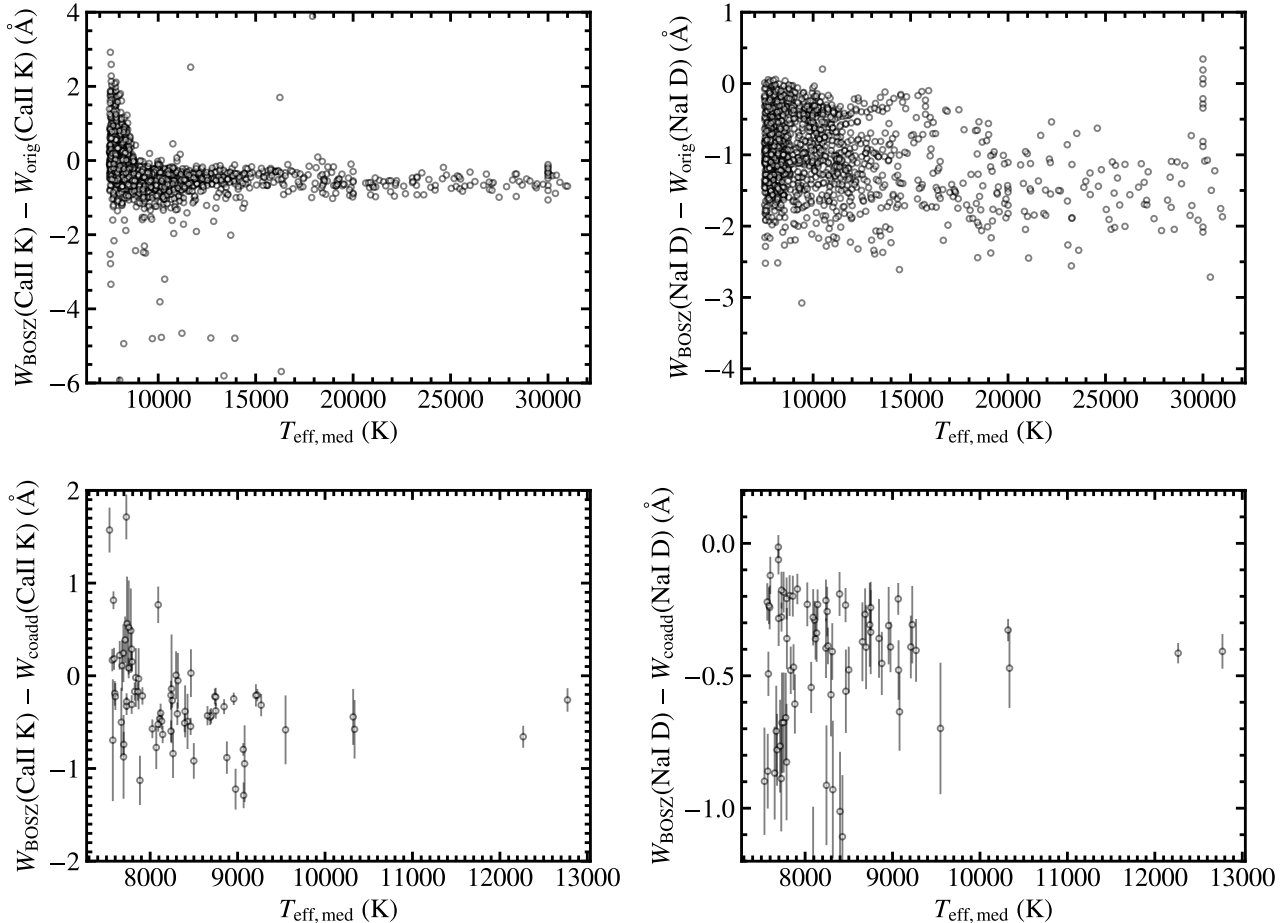


Figure 14. *Top panels:* The difference in the W measured for Ca II K (left) and Na I D (right) in the spectra “cleaned” with BOSZ theoretical templates and that measured in the original spectra, plotted vs. $T_{\text{eff,med}}$. *Bottom panels:* Same as above, for the difference in W measured in the spectra cleaned with BOSZ templates and those measured in the corresponding empirical replacement coadds. The error bars represent the uncertainties on W_{coadd} .

Gaussian with $\sigma = 3 \text{ \AA}$ at the window edges to avoid introducing sharp spectral features. We then reverse our normalization procedure in order to return all pixels outside of these replacement windows to their original flux values. We do not adjust the values of the inverse variance array during this process.

We measure the strength of the Ca II K and Na I D features in the spectra cleaned using this method using the same continuum normalization procedure and spectral windows described in Section 3.1. We show the offset between these line strengths and those measured from the original spectra in the top panels of Figure 14 as a function of $T_{\text{eff,med}}$. The Na I D equivalent widths are nearly universally weaker in the BOSZ spectra across this temperature range, by up to $\approx 2.5 \text{ \AA}$, consistent with the presence of significant interstellar Na I in the original spectra. The same is true for Ca II K for stars at $T_{\text{eff,med}} > 9000 \text{ K}$; however, at lower effective tem-

peratures, a significant fraction of the BOSZ matched templates have stronger Ca II K absorption than the original spectrum. This implies that either the BOSZ modeling fails to capture the behavior of this transition at temperatures below 9000 K, and/or that there are small offsets between the true effective temperature and the $T_{\text{eff,med}}$ determined for some stars that result in a mismatch between the Ca II absorption profile predicted in the matched template and the observed profile.

For comparison, we also show the offsets between the equivalent widths measured in the BOSZ-cleaned spectra and those measured in the corresponding empirical replacement coadds with $\Psi_{\text{thresh}} < 1.0$ in the bottom panels of this figure. There are 73 stars shown in the top panels for which we could construct an empirical replacement coadd, all of which are included in the bottom panels. Because the replacement coadds are composed of “low-ISM” sightlines, we expect these off-

sets to be smaller than those shown in the top panels. This is the case for both Ca II K and Na I, with most $W_{\text{BOSZ}} - W_{\text{coadd}}$ values falling between -1 and $+0.8$ Å or -1 and 0 Å, respectively. Moreover, we see the same rise in $W_{\text{BOSZ}}(\text{Ca II K}) - W_{\text{coadd}}(\text{Ca II K})$ values below $T_{\text{eff,med}} \approx 9000$ K that is evident in the top panel, suggesting that our empirical replacement coadds are likewise dominated by the significant intrinsic dispersion in stellar Ca II profiles in these cooler stars. For the eleven stars with $T_{\text{eff,med}} > 9000$ K in these panels, the mean values of $W_{\text{BOSZ}} - W_{\text{coadd}}$ for Ca II K and Na I are -0.57 Å and -0.43 Å, respectively. The mean values of the uncertainty $\sigma_{W,\text{coadd}}$ are 0.20 Å and 0.11 Å, implying that the empirical replacement coadds tend to overestimate the equivalent widths of these transitions relative to BOSZ by $\sim 3 - 4\sigma_{W,\text{coadd}}$. This could suggest either (1) that even our “low-ISM” sample, from which the empirical replacement coadds are constructed, suffers some level of ISM contamination, or (2) that the BOSZ theoretical template spectra systematically underestimate the intrinsic absorption in these transitions, even at $T_{\text{eff,med}} > 9000$ K.

3.4. The “Clean” MaStar Spectroscopy

To assemble a “clean” spectroscopic sample from the edited spectra described above, we proceed as follows:

1. For all stars having $T_{\text{eff,med}} \leq 9000$ K, we use our empirical replacement spectra (constructed with $\Psi_{\text{thresh}} < 1$) to replace their Na I D profiles where available. We do not make any changes to their Ca II profiles.
2. For stars having $T_{\text{eff,med}} > 9000$ K, we use empirical replacement spectra to replace their Ca II and Na I D profiles if they are available. We instead use our BOSZ-cleaned spectra if we could not construct an empirical replacement sample with $\Psi_{\text{thresh}} < 1$ for the star.

We have assembled this clean sample into a FITS file that is identical in form to that of `mastar-combspec-v3_1_1-v1_7_7-lsfpercent99.5.fits`, with the addition of two flags indicating how each spectrum has been treated as described in Table 3, and with our estimates of W^{ISM} . This FITS file is available via Zenodo at [doi:10.5281/zenodo.14014915](https://doi.org/10.5281/zenodo.14014915).

We again assess the overall impact of these changes on the MaStar spectroscopy by measuring $\Delta W = W_{\text{orig}} - W_{\text{clean}}$ for each star that we now consider to be “clean” (i.e., with flag values of 0, 1, 2 or 3). We show the distributions of these values for each spectral type in Figure 15. The transparent histogram in each panel

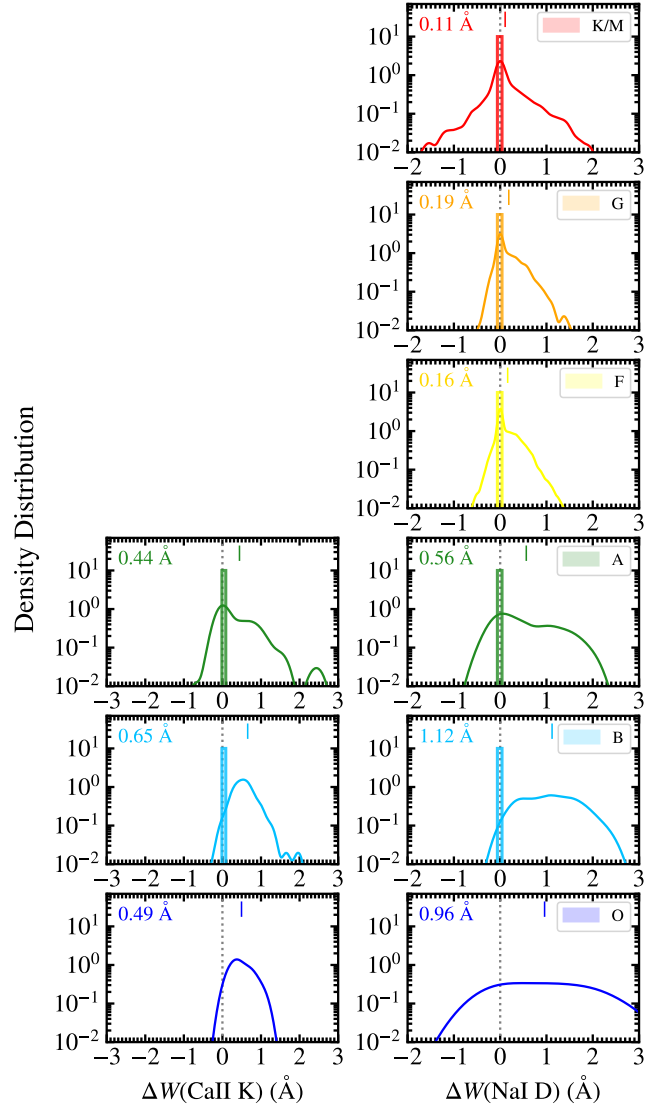


Figure 15. The distributions of the change in the Ca II K (left-hand panels) and Na I D (right-hand panels) equivalent widths relative to the original stellar spectra ($\Delta W = W_{\text{orig}} - W_{\text{clean}}$) for our final cleaned sample. All sightlines that are not considered “low-ISM”, and for which we are able to generate either an empirical or BOSZ spectral replacement, are included in each transparent histogram. The number of low-ISM sightlines of a given spectral type is indicated with the narrow bar at $\Delta W = 0$ Å. Distributions are color-coded by spectral type as indicated in the legends. The smooth curves show continuous probability densities. The colored markers toward the top of each panel indicate the average value of the full distribution (including low-ISM sightlines). These values are also printed at the top left of each panel.

shows the distribution of ΔW values for sightlines for which we replace their Ca II K and Na I D profiles using either coadded low-ISM spectra or a BOSZ theoretical template. The vertical bar at $\Delta W = 0 \text{ \AA}$ indicates the number of low-ISM sightlines of each spectral type. The short vertical hash mark indicates the average ΔW of the full distribution (including low-ISM and cleaned sightlines). $\Delta W(\text{Ca II K})$ distributions for K/M, G and F stars are not shown because we have chosen not to use spectral replacements for Ca II in this temperature range (see above).

The distributions of $\Delta W(\text{Ca II K})$ now all have positive mean values (of 0.4, 0.7 and 0.5 \AA , for A, B, and O types, respectively), and include only five sightlines in total with $\Delta W(\text{Ca II K}) < -1.0 \text{ \AA}$. These distributions also include many more sightlines with $W(\text{Ca II K}) > 0.5 \text{ \AA}$ relative to those shown in Figure 13 due to the inclusion of the BOSZ-cleaned sample.

The distributions showing the change in Na I D absorption strength indicate that its equivalent width has been reduced in the vast majority of the cleaned spectra. The mean value of $\Delta W(\text{Na I D})$ falls in the range 0.1 – 0.2 \AA for K/M, G, and F stars, and increases to 0.6, 1.1, and 1.0 \AA for A, B, and O stars, respectively. This trend is again qualitatively consistent with the predictions shown in Figure 6. We discuss some of the implications of these findings for analyses of the Na I D profile in external galaxy spectra in Section 4.

3.5. Construction of Cleaned Hierarchially-Clustered Spectral Templates

To facilitate the use of these cleaned products for the continuum modeling of external galaxy spectra (e.g., in tandem with the pPXF method; Cappellari et al. 2011), we construct a stellar template library based on the hierarchical clustering analysis described in Abdurro’uf et al. (2022, see their Section 5.2.1). In brief, this analysis uses pPXF to fit pairs of MaStar spectra, where one spectrum is optimized to fit the other. The “distance” used in the hierarchical-clustering analysis is defined as the rms of the optimized difference between the spectra in the pair. The details of the clustering analysis differ between those used in the DR15/DR16 analysis of the MaNGA data (Westfall et al. 2019, Section 5), and the more recent approach described by Abdurro’uf et al. (2022, Section 5.2.1) used to create the set referred to as the MASTAR-HC-v2 templates. We use the latter ap-

proach here.⁸ In particular, the association of each star with each cluster is kept mostly intact (with some exceptions noted below); however, we have updated the stacking approach and included our ISM corrections, as follows.

Our first step in preparing to create new versions of these templates is to apply an extinction correction to each stellar spectrum. We adopt the Fitzpatrick et al. (2019) extinction curve derived for $R_V = 3.1$, taking advantage of the tabulation available with the `dust_extinction` Python package⁹. For stars with *Gaia* colors $G_{BP} - G_{RP} < 0.8$ (Gaia Collaboration et al. 2023b), we use the extinction values (A_V) calculated in the course of the stellar template fitting and parameter analysis of Lazarz et al. (2022). For stars with redder colors, we instead adopt the extinction value implied by its 3D dust map reddening and Equation 1.

We then create two new versions of the HC templates. The first set is constructed from the original, extinction-corrected stellar spectra, but excludes all stars with a flag value > 3 (i.e., all stars for which we could not construct a “cleaned” spectrum, and which are not low-ISM sightlines). This subsample does not contain any stars assigned to cluster IDs 0, 6, 8, 13, 29, 35, or 88, leaving us with a total sample of 58 templates. We further caution that our newly constructed templates for clusters 9, 12, 26, 30, 66, 84, and 96 each contain only one star. We have performed a visual inspection to verify that these templates are in all cases very similar to the original MASTAR-HC-v2 versions.

Finally, we repeat this procedure using the clean version of the spectra assigned to each cluster, creating a new MASTAR-HC-NoISM template set.¹⁰ We show the resulting Ca II K and Na I profiles in orange in Figure 16 and in Appendix B. We show the matching templates created from the original stellar spectra in black for comparison. The clusters are sorted by their median $T_{\text{eff,med}}$ values, ordered from hot to cool. The orange vs. black profiles exhibit the largest differences in the templates containing the hottest stars (shown in Figure 16), consistent with the trends exhibited in the ΔW

⁸ The MASTAR-HC-v2 templates and the table identifying the spectra in each cluster by their MaNGA IDs are provided with the `mangadap` Python package; see https://github.com/sdss/mangadap/tree/4.2.0/mangadap/data/spectral_templates/mastarhc.v2.

⁹ <https://dust-extinction.readthedocs.io/>

¹⁰ These templates are publicly available at https://github.com/sdss/mangadap/tree/4.2.0/mangadap/data/spectral_templates/mastarhc.v2_noism. They may be used with the `mangadap` Python package for galaxy continuum modeling by setting the `eline_fits.fit_templates` key = ‘MASTARHC2-NOISM’.

Table 3. Treatment of Ca II and Na I D Spectral Regions

| Flag Value | Description | Number of Ca II Profiles | Number of Na I Profiles |
|----------------|---|--------------------------|-------------------------|
| 0 | low-ISM sightline (no replacement) | 6342 | 6342 |
| 1 | theoretical spectral replacement | 738 | 738 |
| 2 | empirical spectral replacement | 14 | 12,110 |
| 3 | empirical spectral replacement is available but not used for K/M/G/F/cool A stars | 12,109 | ... |
| 4 ^a | supersolar low-ISM sightline (no replacement) | 84 | 84 |
| 5 ^a | supersolar empirical replacement | 0 | 13 |
| 10 | sightline with likely ISM contamination | 4484 | 4484 |

^aFlag values of 4 indicate stars having $[\text{Fe}/\text{H}] > 0$, $W^{\text{ISM}}(\text{Ca II K}) < 0.4 \text{ \AA}$, $W^{\text{ISM}}(\text{Na I 5891}) < 0.15 \text{ \AA}$, and either $W^{\text{ISM}}(\text{Ca II K}) > 0.07 \text{ \AA}$ or $W^{\text{ISM}}(\text{Na I 5891}) > 0.05 \text{ \AA}$ (our supersolar low-ISM sample). Flag values of 5 indicate stars having $[\text{Fe}/\text{H}] > 0$, for which we have replaced their Na I D profiles with coconditions of stars with similar parameters drawn from the supersolar low-ISM sample. Both of these subsamples are used in our construction of SSP model spectra, as described in Section 3.6.

values shown in Figure 15. The differences in the Ca II K transitions between these two sets of profiles become negligible for nearly all templates having median stellar effective temperatures $\text{med}(T_{\text{eff,med}}) < 8100 \text{ K}$. Subtle differences persist in the black vs. orange Na I D profiles above $\text{med}(T_{\text{eff,med}}) \approx 3500 \text{ K}$ (shown in Appendix B).

3.6. Construction of Simple Stellar Population Model Spectra

3.6.1. Methodology

Analyses of external galaxy spectra aiming to constrain stellar population ages, metallicities, abundance patterns, or the IMF often rely on spectral templates constructed from stellar population models (e.g., Cid Fernandes et al. 2005; Ocvirk et al. 2006; Pérez et al. 2013; Conroy et al. 2014; González Delgado et al. 2015; Cappellari 2017; Wilkinson et al. 2017; Goddard et al. 2017; Conroy et al. 2018; Feldmeier-Krause et al. 2021, and many others). To facilitate the use of our cleaned spectra in such analyses, we follow the methods described in Maraston et al. (2020) to construct a suite of “cleaned” SSP model spectra. Summarizing briefly, as in Maraston (2005) and Maraston et al. (2020), we adopt isochrones and stellar tracks from Cassisi et al. (1997a), Cassisi et al. (1997b), and Cassisi et al. (2000) for ages older than $\sim 30 \text{ Myr}$, Schaller et al. (1992) for younger ages, and Girardi et al. (2000). Fuel consumption during the thermally pulsating asymptotic giant branch phase is calibrated empirically. Realistic horizontal branch morphologies are generated by assuming Reimers-type mass-loss along the red giant branch as in Maraston (2005). We adopt the fuel consumption approach to calculate the energetic contribution of each post-main-sequence phase to a given SSP, assuming it is proportional to the amount of fuel available for burning

in that phase (e.g., Renzini & Buzzoni 1986; Maraston 1998).

In constructing our SSPs, we adopt the calibrated median stellar parameters for the MaStar sample as described in Section 2.1 (R. Yan et al., in preparation). These parameters differ from those adopted in Maraston et al. (2020), which made use of parameters included in the first release of the MaStar library (Yan et al. 2019; Chen et al. 2020) and those derived from theoretical spectral fitting by Hill et al. (2022). We correct the spectra for extinction as described in Yan et al. (2019). We also establish the energy scale of each stellar spectrum as described in Maraston et al. (2020), first normalizing each spectrum by its average flux at $\sim 5550 \text{ \AA}$, and then rescaling it to the average $\sim 5550 \text{ \AA}$ luminosity of a theoretical stellar spectrum with the same stellar parameters. As in Maraston (2005) and Maraston et al. (2020), we use the Lejeune et al. (1997) theoretical library for this renormalization. Finally, we separate the MaStar stars into several different metallicity bins centered at $[Z/H] = -1.35, -0.33, 0.0$, and $+0.35$ (corresponding to the metallicities of the SSP grid calculated in Maraston 2005) with approximate widths of $\pm 0.1 \text{ dex}$. Within each metallicity bin, empirical spectra are assigned an evolutionary phase (e.g., main sequence, red giant branch). Then, we calculate the spectrum representing a given T_{eff} and $\log g$ via interpolation of the logarithmic fluxes of stars within the relevant phase as a function of $\log T_{\text{eff}}$ and $\log g$. These interpolated spectra are combined into representative SSPs with ages spanning 3 Myr to 15 Gyr . We assume a Salpeter IMF for these calculations.

3.6.2. The Addition of a Supersolar Low-ISM Sample

In examining the $T_{\text{eff}} - \log g$ distributions of stars having “cleaned” spectra in the $[Z/H] = +0.35$ bin, we found that we lacked any stars having $T_{\text{eff}} > 6000 \text{ K}$,

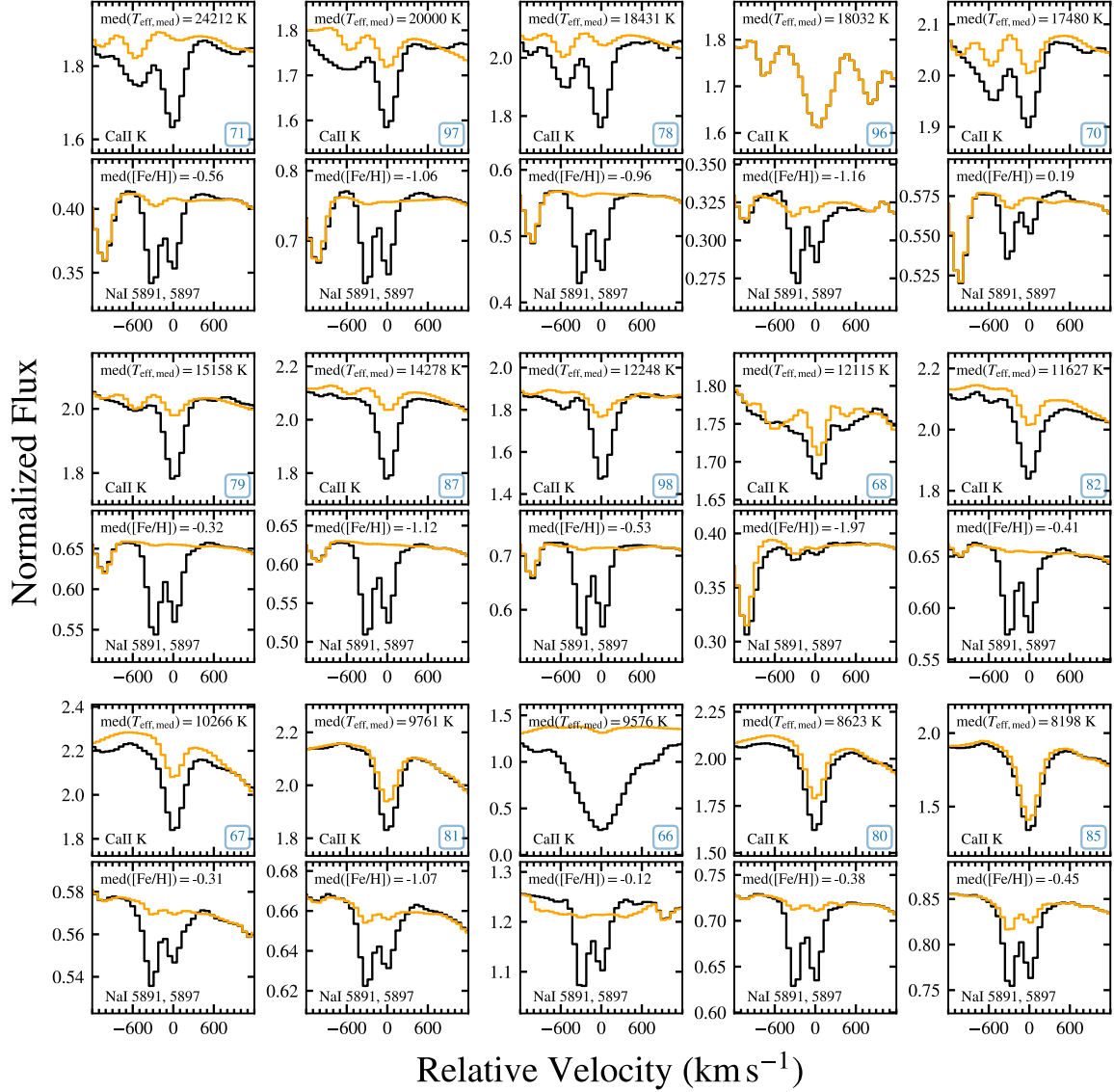


Figure 16. Comparison of hierarchically-clustered MaStar spectral templates constructed without correction for ISM absorption (black) and from our “cleaned” spectral sample (orange). Each pair of stacked panels shows the same template at the locations of the Ca II K and Na I $\lambda\lambda 5891, 5897$ transitions on top and bottom, respectively. Velocities are computed relative to the Ca II K $\lambda 3934$ and Na I $\lambda 5897$ rest wavelengths. The templates have been ordered according to the median $T_{\text{eff,med}}$ value of the stars used in each. This value, along with the median $[\text{Fe}/\text{H}]$ value, is noted in each panel pair. The cluster ID of each template is indicated in blue. The remaining templates are included in Appendix Figure 25.

as well as any stars sampling the red giant branch at $\log g < 2$. We were therefore unable to construct SSPs using the procedure described above. This is unsurprising given the small numbers of low-ISM stars with $0.2 < [\text{Fe}/\text{H}] < 0.4$ and $\log g < 3$ or $3\theta < 2$ shown in Figure 7. To improve our sampling of these regions of parameter space, we relaxed our criteria defining low-ISM stars to include those with $[\text{Fe}/\text{H}] > 0$, $W^{\text{ISM}}(\text{Ca II K}) < 0.4 \text{ \AA}$, and $W^{\text{ISM}}(\text{Na I 5891}) < 0.15 \text{ \AA}$. This “supersolar low-ISM” sample includes 84 stars that were previously assigned flag values of 10.

We use this supersolar low-ISM sample to construct empirical spectral replacement coadds as described in Section 3.2 for as many additional stars as possible. We are able to construct coadds with $\Psi_{\text{thresh}} < 1$ for 13 more stars, and we use these coadds to replace their Na I D spectral regions. We find that this supplementary sample of high- $[\text{Z}/\text{H}]$ stars fully samples the red giant branch and high- T_{eff} portions of the corresponding isochrones, and we include them in our construction of our $[\text{Z}/\text{H}] = +0.35$ SSP spectral templates. We have also indicated all supersolar low-ISM stars and all stars with supersolar low-ISM empirical replacements with flag values of 4 and 5 in the FITS file containing our cleaned spectra (described in Section 3.4 and Table 3).

3.6.3. “Cleaned” SSP Ca II and Na I D Absorption Profiles

As for the hierarchically-clustered templates described above, we generate two versions of each SSP spectrum. The first is constructed from the original, extinction-corrected MaStar stellar spectra, but includes only stars having flag values ≤ 5 . The second¹¹ is constructed from the “cleaned” versions of the extinction-corrected stellar spectra. We show the profiles of the resulting Ca II K and Na I spectral regions for a subset of these SSPs in orange in Figure 17. The matching SSP templates created from the original stellar spectra are shown in black. Note that in a few cases, the orange profile lies underneath a dashed cyan profile showing an SSP spectrum constructed solely from low-ISM stars, described in the following subsection. As expected, the differences between the orange vs. black profiles tend to be the greatest at the youngest ages and lowest metallicities. The Na I profiles for the 10 Myr old SSPs (both

original and cleaned) exhibit stronger absorption than those with 100 Myr ages, particularly for metallicities $[\text{Z}/\text{H}] \geq -0.33$. This is likely due to the dominant contribution of red supergiant stars in the Schaller et al. (1992) 10 Myr isochrones. The Ca II K profiles exhibit minimal differences for ages $\gtrsim 1$ Gyr; however, the black Na I profiles are evidently affected by ISM contamination even at an age of 10 Gyr at solar and subsolar metallicities. The differences between the original and cleaned Na I profiles in our supersolar SSPs are negligible; however, this is because the supersolar SSPs are dominated by stars in the supersolar low-ISM sample, rather than those for which the Na I spectral region has been replaced. Given the relatively high degree of ISM contamination we have predicted for the overall sample of high-metallicity stars, we posit that supersolar SSP templates constructed without regard for this contamination would be even more severely affected than those constructed for solar metallicity. We also caution that because we have relaxed our low-ISM criteria to construct the “cleaned” supersolar SSP templates, they too likely suffer from some degree of ISM contamination (i.e., at a level $W^{\text{ISM}}(\text{Na I 5891}) < 0.15 \text{ \AA}$). We discuss the implications of all of these findings for constraints on stellar ages, Na abundances, and the IMF from stellar population modeling below in Sections 4.2 and 4.3.

3.6.4. SSP Construction from Low-ISM Stars

To test the robustness of our cleaning procedure, we have constructed an additional set of SSP templates using only our original “low-ISM” sample of stars. The parameter space sampling of low-ISM stars is insufficient for the construction of SSP spectra with $[\text{Z}/\text{H}] = +0.35$; however, we were able to use the procedure described above to generate SSP templates for metallicity $[\text{Z}/\text{H}] = -1.35$ at ages > 2 Gyr, and for metallicities $[\text{Z}/\text{H}] = -0.33$ and 0.0 at ages > 0.5 Gyr. We show some of the resulting Na I profiles in Figure 17 with dashed cyan lines. These profiles are very similar, and in some cases nearly identical, to those of the cleaned templates. The Na I D equivalent width values measured from these low-ISM templates are also very similar to those of the cleaned SSP spectra described above, with a maximum offset $|\Delta W|$ of 0.17 \AA , a maximum fractional offset $|\Delta W/W_{\text{clean}}|$ of 9%, and a mean fractional offset of 3–4%. We conclude from this comparison that our procedure for ISM removal is indeed robust, and does not introduce unwanted artifacts into our final cleaned SSP templates.

¹¹ These templates are publicly available at <https://doi.org/10.5281/zenodo.14807331>. A subset of these templates with ages = 0.003, 0.01, 0.03, 0.1, 0.3, 1.0, 3.0, 9.0, and 14 Gyr is available at https://github.com/sdss/mangadap/tree/4.2.0/mangadap/data/spectral_templates/mastar_ssp_noism.v1.0. They may be used with the mangadap Python package for galaxy continuum modeling by setting the `eline_fits.fit.templates` key = ‘MASTARSSP-NOISM’.

4. DISCUSSION

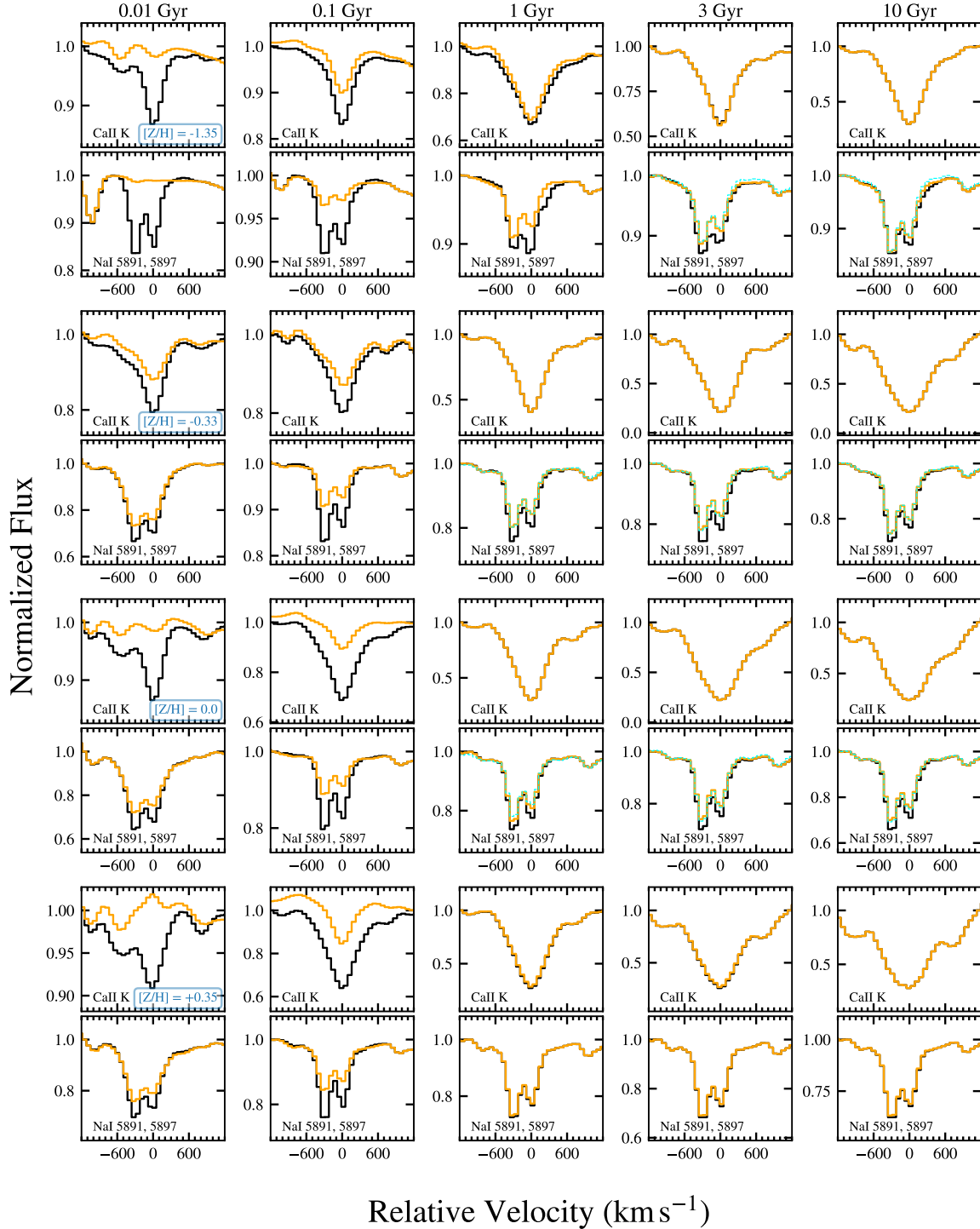


Figure 17. Comparison of MaStar SSP spectral templates constructed without correction for ISM absorption (black) and from our “cleaned” spectral sample (orange). Results for SSP templates constructed solely from low-ISM stars as described in Section 3.6.4 are shown with dashed cyan lines. Each pair of stacked panels shows the same template at the locations of the Ca II K and Na I $\lambda\lambda 5891, 5897$ transitions on top and bottom, respectively. Velocities are computed relative to the Ca II K $\lambda 3934$ and Na I $\lambda 5897$ rest wavelengths. Models increase in age from left to right, as labeled above the top panels, and increase in $[Z/H]$ from top to bottom, as indicated in blue in the left-most Ca II K panels.

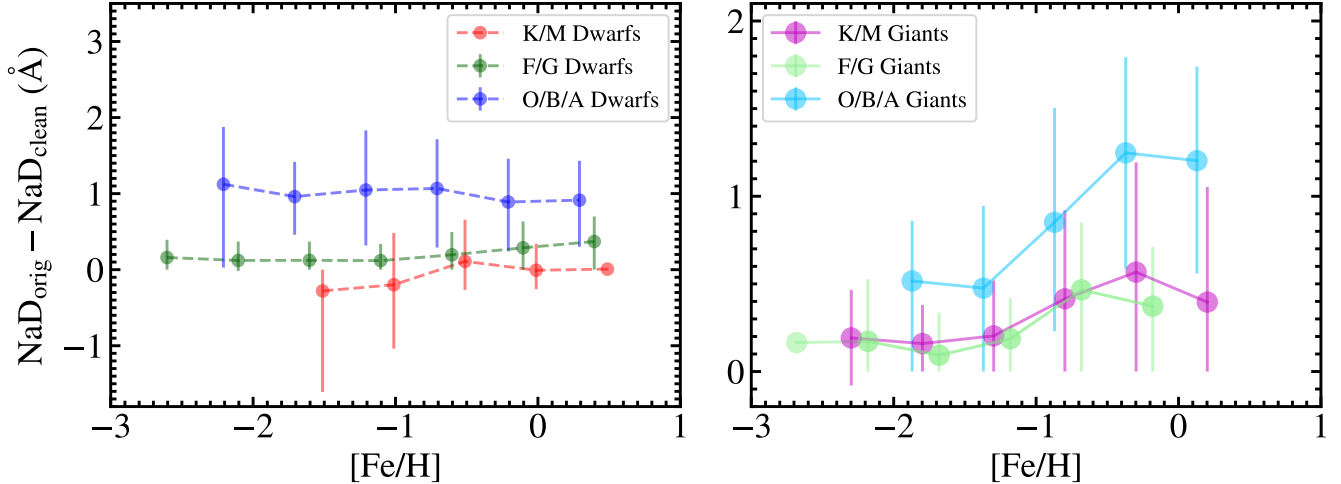


Figure 18. The difference between the NaD spectral index measured in the original MaStar spectra and that measured in the cleaned spectra vs. stellar $[\text{Fe}/\text{H}]$. *Left:* $\text{NaD}_{\text{orig}} - \text{NaD}_{\text{clean}}$ for dwarf stars (with $\log g > 4$) divided into three temperature bins. Each point shows the average value of this offset in a bin of width $\Delta[\text{Fe}/\text{H}] = 0.5$. The error bars indicate the 16th- and 84th-percentile values of these offsets within each bin. *Right:* Same as that shown at left, for giant stars having $\log g < 4$.

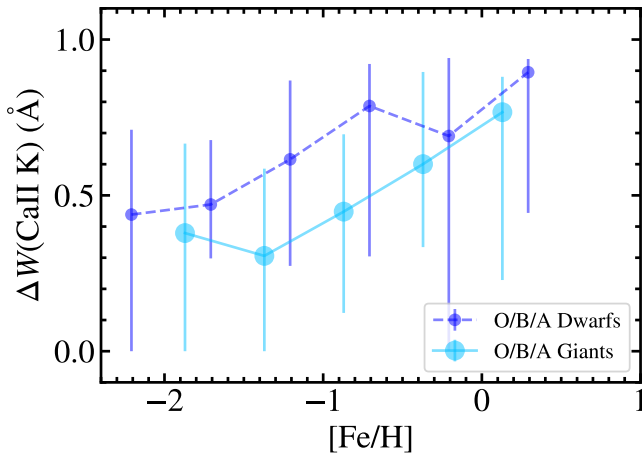


Figure 19. The difference between $W(\text{Ca II K})$ measured in the original MaStar spectra and that measured in the cleaned spectra vs. stellar $[\text{Fe}/\text{H}]$ for O/B/A-type stars. Results for dwarf stars (with $\log g > 4$) are shown with small dark blue circles, and results for giant stars are shown with large light blue circles. Each point shows the average value of this offset in a bin of width $\Delta[\text{Fe}/\text{H}] = 0.5$. The error bars indicate the 16th- and 84th-percentile values of these offsets within each bin.

The strengths of metal and hydrogen absorption lines in the spectra of external galaxies have long been understood to trace the elemental abundances and ages of the underlying stellar populations (e.g., Burstein et al. 1984, 1986; Worthey et al. 1992, 1994, 2014; Trager et al. 1998; Kuntschner 2000; Thomas et al. 2005; Bernardi et al. 2006; Johansson et al. 2012). The Na I D stellar

absorption feature has traditionally been quantified by the “NaD” Lick index (Trager et al. 1998), and serves as an indicator of the Na abundance relative to Fe (e.g., Thomas et al. 2003, 2011b; Parikh et al. 2018, 2021). Recent studies of this feature in the nearby galaxy population have concluded that massive systems (both early-type galaxies and massive spirals) are typically significantly Na-enhanced (with $[\text{Na}/\text{Fe}]$ up to $+0.6 - 0.8$ dex; McConnell et al. 2016; Alton et al. 2017; van Dokkum et al. 2017; Vaughan et al. 2018; Parikh et al. 2018), while low-mass galaxies ($\log M_*/M_\odot < 10$) have Na abundances close to solar (Parikh et al. 2018, 2019, 2021). The NaD index has also been used in conjunction with the surface-gravity-sensitive “NaI” spectral index at $\sim 8200 \text{ \AA}$ to constrain the slope of the IMF in early-type galaxies (e.g., Martín-Navarro et al. 2015, 2023; Parikh et al. 2018; La Barbera et al. 2019; Feldmeier-Krause et al. 2021; Gu et al. 2022). A common approach to linking the strength of this feature in a given stellar population to its $[\text{Na}/\text{Fe}]$ relies on the measurement of NaD for individual stellar template spectra in a stellar library of choice. NaD is then calibrated to $[\text{Na}/\text{Fe}]$ via the construction of SSP models that establish the weighting of the index strengths of a representative set of stars for a given IMF, age, and elemental abundance pattern (e.g., Worthey et al. 1994; Worthey & Ottaviani 1997; Maraston 1998; Thomas et al. 2003; Johansson et al. 2010).

4.1. Relation Between Interstellar Absorption Effects and Stellar T_{eff} , $\log g$, and $[\text{Fe}/\text{H}]$

We now consider the degree to which the NaD spectral index strengths of stars in the MaStar sample are affected by the Milky Way ISM. While none of the aforementioned studies rely on the MaStar stellar library to calibrate the relation between spectral indices and elemental abundances (and instead, more recent studies have used the MILES library constructed by Sánchez-Blázquez et al. 2006 or one of its many extensions; e.g., Vazdekis et al. 2010, Conroy et al. 2018), we argue that the Milky Way ISM will likely affect any such calibration if it is based on an empirical library, and if the stars were selected without regard for their interstellar reddening, distance, or Galactic latitude. We have measured the NaD index using the Trager et al. (1998) definition¹² for both the original spectrum (NaD_{orig}) and cleaned spectrum ($\text{NaD}_{\text{clean}}$) of every star in MaStar with a flag value ≤ 3 . The results are summarized in Figure 18. The left-hand panel shows the difference in these values for “dwarf” stars having $\log g > 4$. The dwarf sample is further divided into “K/M” ($T_{\text{eff,med}} < 5200$ K), “F/G” ($5200 \text{ K} < T_{\text{eff,med}} < 7610$ K), and “O/B/A” ($T_{\text{eff,med}} > 7610$ K) subsamples. Each point shows the average value of this difference in the relevant subsample across a metallicity bin of width $\Delta[\text{Fe}/\text{H}] = 0.5$. We include both low-ISM sightlines and sightlines for which we have successfully generated replacement spectral regions in this mean. The error bars show the 16th- and 84th-percentile values within each bin. The right-hand panel shows the same measurements for giant stars having $\log g < 4$. Each bin shown contains at least five stars.

This figure demonstrates that the strength of NaD in cool dwarfs is not significantly affected by ISM absorption in an aggregate sense. However, the dispersion in these offsets can be large ($> 0.5 \text{ \AA}$), suggesting that individual stars may occasionally be subject to strong ISM absorption. The lowest- $[\text{Fe}/\text{H}]$ bin exhibits a relatively large negative mean offset (of -0.3 \AA); however, we caution that it contains only 10 stars, three of which are low-ISM sightlines. F/G dwarfs exhibit a typical offset of $0.1 - 0.4 \text{ \AA}$, while O/B/A dwarfs exhibit more extreme offsets of $0.9 - 1.1 \text{ \AA}$. K/M giants exhibit mean offsets of $0.2 - 0.6 \text{ \AA}$; F/G giants exhibit mean offsets in the range $0.1 - 0.5 \text{ \AA}$; and O/B/A giants exhibit offsets in the range $0.5 - 1.2 \text{ \AA}$.

In summary, we find that the strength of NaD is systematically overestimated in the original MaStar sample due to ISM contamination. The degree of this overestimation is largest for hot stars, but persists at a level of $\sim 0.2 - 0.6 \text{ \AA}$ for cool giants. This in turn suggests that SSP models built from the original MaStar library to calibrate the relationship between NaD and $[\text{Na}/\text{Fe}]$ would yield index strengths that are larger than those intrinsic to the stars for a given $[\text{Na}/\text{Fe}]$. If this relationship is used in combination with NaD measurements of observed spectra of external galaxies, assuming the galaxies do not themselves contain significant interstellar Na I, it would yield $[\text{Na}/\text{Fe}]$ abundances that are systematically underestimated.

For completeness, we show the difference in the Ca II K line strength between the original and cleaned spectra of O/B/A dwarfs and giants as a function of the stellar metallicity in Figure 19.¹³ Metallicity bins are constructed in the same manner as for Figure 18, and each contains at least five stars. O/B/A dwarfs exhibit mean equivalent width offsets of $0.4 - 0.9 \text{ \AA}$, while hot giants exhibit slightly more modest offsets in the range of $0.3 - 0.8 \text{ \AA}$. These offsets furthermore appear to increase with increasing stellar $[\text{Fe}/\text{H}]$, as is evident for the NaD offsets exhibited by giant stars (i.e., shown in the right-hand panel of Figure 18). As highly temperature-sensitive transitions, Ca II H & K are not typically used to constrain Ca abundances via stellar population synthesis analysis (although they may be used to aid in the selection of extremely metal-poor stars; e.g., Starkenburg et al. 2017; Youakim et al. 2017). Instead, because the strengths of Ca II H & K increase dramatically with decreasing temperature in A stars, they have been useful as a diagnostic of stellar population age in young stellar populations ($\lesssim 1$ Gyr; Rose 1985; Leonardi & Rose 1996; Wild et al. 2007). SSP models constructed from the original MaStar library would overestimate the strength of Ca II H & K at a given age (Figures 17 and 19). The best-fitting combination of SSP model templates for an observed galaxy spectrum would therefore imply an age that is younger than the galaxy’s true age, under the assumption that the observed galaxy does not exhibit significant interstellar Ca II absorption. We further discuss the validity of this assumption in Section 4.3.

¹² The NaD index is defined to be the equivalent width measured in the spectral region $5876.875 \text{ \AA} < \lambda_{\text{rest}} < 5909.375 \text{ \AA}$. The continuum is determined from a linear fit to the mean flux measured in two pseudocontinuum regions on either side of the feature (i.e., $5860.625 \text{ \AA} < \lambda_{\text{rest}} < 5875.625 \text{ \AA}$ and $5922.125 \text{ \AA} < \lambda_{\text{rest}} < 5948.125 \text{ \AA}$).

¹³ While a spectral index (CaHK) defined to assess absorption strength in this spectral region was introduced by Serven et al. (2005) in their analysis of line indices in elliptical galaxies, we find that it is not well-suited for use on hot stars due to their strong Balmer absorption features falling in the index pseudocontinuum regions.

We also note that the construction of SSP templates or $[\text{Na}/\text{Fe}]$ calibrations from stars selected to have very close distances, or very low values of $E(B - V)$ and high Galactic latitudes, would likely reduce their ISM contamination to a degree similar to that seen above. That is, a selection of stars with distances < 0.1 kpc, or with $0.1 \text{ kpc} < D < 0.3$ kpc, $E_{\text{DustMap}} < 0.01$, and $b > 40^\circ$, yields 1177 low-ISM stars and only 61 stars that do not fall into our low-ISM sample. A simple selection of stars with $E_{\text{DustMap}} < 0.01$, on the other hand, yields 5222 low-ISM stars and 2117 that do not fall into our low-ISM sample. SSP templates constructed from such a selection would likely have lower ISM contamination than those constructed without regard for reddening, but would not be as “clean” as the stellar sample we have constructed above. The degree of ISM contamination for SSP templates or abundance calibrations constructed from such a sample – or any stellar library – may be estimated using our model for $W^{\text{ISM}}(\log E_{\text{DustMap}}, b, D)$ described in Section 2.2.

4.2. Interstellar Absorption Effects in Simple Stellar Population Model Spectra

Here we assess the significance of the effects of interstellar Ca II and Na I absorption as a function of the stellar population age and metallicity using the MaStar SSP spectra constructed as described in Section 3.6. In detail, we compare the strength of either $W(\text{Ca II K})$ or NaD measured from the SSP templates constructed from the original spectra, $W(X)_{\text{orig}}^{\text{SSP}}$, with the strength of the same feature measured from the corresponding “cleaned” SSPs ($W(X)_{\text{clean}}^{\text{SSP}}$). In Figure 20, we show the fractional enhancement in these features due to Milky Way ISM, $(W(X)_{\text{orig}}^{\text{SSP}} - W(X)_{\text{clean}}^{\text{SSP}})/W(X)_{\text{clean}}^{\text{SSP}}$, as a function of the SSP age for populations with $[\text{Z}/\text{H}] = -1.35$ and 0.0. For completeness, we also show NaD fractional enhancements calculated relative to the SSPs constructed solely from low-ISM stars (described in Section 3.6.4) for ages > 2 Gyr at $[\text{Z}/\text{H}] = -1.35$, and for ages > 0.5 Gyr at solar metallicity (i.e., $W(X)_{\text{orig}}^{\text{SSP}} - W(X)_{\text{lowISM}}^{\text{SSP}}/W(X)_{\text{lowISM}}^{\text{SSP}}$).

We find that interstellar Ca II absorption enhances the strength of $W(\text{Ca II K})^{\text{SSP}}$ by between 20% and 200% at solar metallicity for ages < 400 Myr due to the dominant contribution of hot stars in such young stellar populations. At $[\text{Z}/\text{H}] = -1.35$, a similar level of Ca II K enhancement is evident, but weakens to $< 20\%$ at ages $\gtrsim 300$ Myr. Because we do not alter the Ca II H&K profiles of stars cooler than $T_{\text{eff,med}} = 9000$ K, we do not predict any artificial enhancement for these transitions in SSPs dominated by later spectral types (at ages $\gtrsim 1$ Gyr).

We predict more significant enhancements of NaD across the full range of ages explored. At young ages, we predict a $\gtrsim 100\%$ enhancement in the NaD spectral index strength, which persists until ages of ~ 600 Myr for the low-metallicity SSPs. At solar metallicity, we predict enhancements of $\gtrsim 50\%$ for nearly all ages between 30 and 600 Myr. In general, we predict more significant fractional enhancements of NaD for our subsolar SSPs relative to the solar-metallicity case due to the increased importance of hot dwarfs and cool giants in the former, and because the intrinsic NaD is weaker in lower-metallicity stars. However, even in the solar-metallicity case at older ages, we predict artificial enhancements of NaD of $\sim 20 - 30\%$ in the age range 1 – 4 Gyr, and of $> 10\%$ at 4 – 15 Gyr. If we instead use the SSPs constructed from low-ISM stars as our reference, we predict artificial enhancements of NaD of $\sim 20\%$ at ages 0.5 – 1.5 Gyr, and of $> 10\%$ at 1.5 – 12 Gyr.

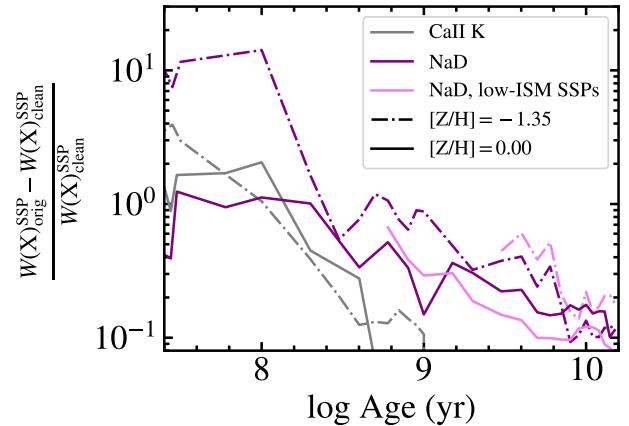


Figure 20. Fractional enhancement due to interstellar absorption of the equivalent width of Ca II K (gray) and the NaD spectral index (purple) for solar-metallicity (solid) and $[\text{Z}/\text{H}] = -1.35$ (dashed-dotted) SSPs. The violet curves show the fractional NaD enhancement estimated relative to the SSPs constructed solely from low-ISM stars described in Section 3.6.4. We measure enhancements of $\gtrsim 100\%$ for young stellar populations in both transitions, and measure NaD enhancements $\gtrsim 10\%$ across the full range of ages at solar metallicity.

4.3. The Impact of Interstellar Absorption on Analyses of Stellar Population Age, Sodium Abundance, and the IMF

4.3.1. Artificial Enhancements as a Function of Age

Nearby extragalactic stellar populations are of course substantially more complex than the SSPs explored above (e.g., Franx & Illingworth 1990; Kauffmann et al.

2003; Cid Fernandes et al. 2005; Pérez et al. 2013; Sánchez-Blázquez et al. 2014; Roig et al. 2015; González Delgado et al. 2015; Goddard et al. 2017; Parikh et al. 2021). Typical late-type galaxies are understood to be comprised of both old ($\sim 5 - 6$ Gyr), metal-poor and younger (~ 1 Gyr), metal-rich stellar populations, and exhibit negative lightweighted age gradients consistent with “inside out” formation (e.g., Pérez et al. 2013; González Delgado et al. 2014, 2015; Goddard et al. 2017; Parikh et al. 2021). Early-type galaxies are well-understood to be dominated by old stars (with ages $\gtrsim 10$ Gyr), but can contain a subdominant younger population ($\gtrsim 3$ Gyr old) toward their centers (Trager et al. 1998; Kuntschner 2000; Mehlert et al. 2003; Thomas et al. 2005; Bernardi et al. 2006; Clemens et al. 2006; Spolaor et al. 2010; Greene et al. 2015; Goddard et al. 2017). We therefore expect that absorption originating in the Milky Way’s ISM would systematically increase the strength of NaD by at least 10 – 30% in MaStar stellar population synthesis models of late-type galaxies if constructed from the original library, and that the magnitude of this effect would increase with radius as the overall stellar age decreases. Stellar population synthesis models of early-type galaxies would exhibit at least a 10% enhancement of NaD due to contaminating ISM absorption, with a greater enhancement associated with any younger stars at their centers.

Stellar population synthesis analyses that must suffer the most significant impacts from Milky Way ISM are those focusing on galaxies with a starburst or post-starburst component. Post-starburst galaxies are often identified by a combination of strong Balmer absorption and a lack of emission lines signifying ongoing star formation (e.g., Dressler & Gunn 1983; Couch & Sharples 1987; Zabludoff et al. 1996; Wild et al. 2007; Kaviraj et al. 2007). In the local Universe, these spectral features have been found to arise from starburst events that occurred within the past ~ 1 Gyr and generated 20 – 60% of the galaxy’s stellar mass (Kaviraj et al. 2007). The light from these recent bursts will contribute a yet larger fraction to the galaxies’ rest-frame optical emission, implying that their spectra will be dominated by stellar populations for which stellar synthesis models constructed from the original MaStar library would have a $\gtrsim 20\%$ enhancement in the strength of Ca II K due to the ISM, and a $\gtrsim 50\%$ enhancement of NaD.

Many modern analyses that use the stellar population synthesis technique to assess the star formation histories, chemical abundances, and/or IMF of extragalactic systems do so by fitting linear combinations of SSP templates to observed spectra covering the full optical range (e.g., Cid Fernandes et al. 2005; Ocvirk et al. 2006; Con-

roy et al. 2014, 2018; Cappellari 2017; Wilkinson et al. 2017; Feldmeier-Krause et al. 2021). This full spectrum fitting can in principle take advantage of the simultaneous fitting of numerous spectral features to constrain physical quantities, reducing the importance of accurate modeling of those few transitions affected by the ISM. However, as noted above, constraints on the ages of recent starburst events are driven primarily by the Ca II H&K transitions for studies that lack corroborating rest-frame UV photometry (e.g., Rose 1985; Leonardi & Rose 1996, 2003; Wild et al. 2007; Kaviraj et al. 2007).

4.3.2. Implications for $[Na/Fe]$ Abundances in Early-type Galaxies

$[Na/Fe]$ may likewise be constrained via the simultaneous analysis of numerous other metal-line transitions in rest-frame optical spectroscopy of early-type galaxies, as the abundance of Na has a significant impact on the electron pressure in cool stellar atmospheres (Conroy & van Dokkum 2012a). However, such constraints are heavily dominated by Na I D, as it is significantly stronger than many of these other transitions, including the surface-gravity-sensitive Na I $\lambda\lambda 8183, 8195$ features (Thomas et al. 2011a), and the Na I $1.14\mu\text{m}$ and $2.21\mu\text{m}$ transitions in the near-IR (Conroy & van Dokkum 2012a). It also has a weak dependence on the IMF slope (Conroy & van Dokkum 2012b; Spiniello et al. 2012; La Barbera et al. 2013; Parikh et al. 2018). A $\gtrsim 10\%$ enhancement of NaD due to ISM in stellar population model spectra of early-type galaxies would imply a yet more extreme Na abundance enhancement than is currently estimated for these systems (i.e., beyond the $\sim +0.6 - 0.8$ dex reported by Alton et al. 2017, van Dokkum et al. 2017, Parikh et al. 2018, and Vaughan et al. 2018). In detail, the SSP models of Conroy & van Dokkum (2012a) predict that varying $[Na/Fe]$ by ± 0.3 dex for a 13.5 Gyr stellar population with a Chabrier IMF would change the strength of the NaD index by $\approx +30\% / -20\%$ relative to the value predicted at solar metallicity. This suggests that a $>10\%$ correction to SSP model NaD indices would result in a $\sim +0.1 - 0.2$ dex enhancement in $[Na/Fe]$, and thus an overall Na abundance of $\sim +0.7 - 1.0$ dex. In the case that there is a younger component toward the centers of these galaxies (Goddard et al. 2017), the effect of interstellar contamination would vary systematically with radius. These studies have further noted that the enhanced $[Na/Fe]$ abundances they estimate are inconsistent with the Type II supernova yields calculated by Woosley & Weaver (1995), and are not observed in individual stars in the Milky Way (Bensby et al. 2014, 2017). However, the updated yield calculations by Kobayashi et al. (2006) are in better accord with early-type galaxy abun-

dances, as they imply that $[\text{Na}/\text{Fe}]$ increases strongly with increasing progenitor metallicity while remaining consistent with observed Galactic stellar abundance ratios (Kobayashi et al. 2020). The prospect that early-type galaxy $[\text{Na}/\text{Fe}]$ measurements are underestimated due to ISM contamination may therefore be fully consistent with the Na enrichment levels expected for such massive systems.

4.3.3. Complications from External Galaxy ISM Absorption

The effects of these systematics are further complicated by the possible presence of cool Ca II- and/or Na I D-absorbing material in the external galaxies being studied. Starburst galaxies are indeed well-known to exhibit both Ca II and Na I interstellar absorption (Heckman et al. 2000; Rupke et al. 2005; Zych et al. 2007; Chen et al. 2010b; Concas et al. 2019; Roberts-Borsani et al. 2020; Veilleux et al. 2020; Rubin et al. 2022), with stronger absorption associated with higher star formation rates (e.g., Chen et al. 2010b; Straka et al. 2015; Rubin et al. 2022). In particular, interstellar $W(\text{Ca II K})$ values of $\sim 0.3 - 1 \text{ \AA}$ are observed to arise in hosts with SFRs $\gtrsim 1 M_{\odot} \text{ yr}^{-1}$ (Rubin et al. 2022). These absorption strengths are comparable to the equivalent width enhancement due to Milky Way interstellar Ca II (i.e., $W(\text{Ca II K})_{\text{orig}}^{\text{SSP}} - W(\text{Ca II K})_{\text{clean}}^{\text{SSP}}$ values fall in the range $0.5 - 1.5 \text{ \AA}$ for young SSPs). We therefore expect that in practice, the effect of the presence of Milky Way ISM in stellar population synthesis analyses of starbursting systems is partially or completely compensated by the presence of ISM in the host. That is, an analysis that fits “contaminated” SSP templates to observed Ca II H&K profiles, ignoring the effects of the ISM altogether, will not underestimate the galaxy’s age to the extent implied by Figure 20, and indeed may overestimate its age in some cases.

Early-type galaxies, on the other hand, are commonly assumed to exhibit minimal interstellar Na I D absorption (e.g., Conroy & van Dokkum 2012b; Spiniello et al. 2012; La Barbera et al. 2013; Parikh et al. 2018; Gu et al. 2022; Lonoce et al. 2023; den Brok et al. 2024; Parikh et al. 2024; Maksymowicz-Maciata et al. 2024). Parikh et al. (2018) tested this assumption by deriving the spatially-resolved $E(B - V)$ profile for SDSS-IV/MaNGA galaxies from spectra coadded in radial bins (and having stellar masses $9.9 < \log M_{*}/M_{\odot} < 10.8$). These authors measured values of $\sim 0.1 \text{ mag}$ toward the galaxy centers and $\lesssim 0.05 \text{ mag}$ toward the outskirts. The Poznanski et al. (2012) relation, derived for the Milky Way’s ISM and halo, implies a Na I absorption strength of $\approx 0.7 \text{ \AA}$ for $E(B - V) = 0.1$. While this relation

may not be appropriate for the physical conditions in the ISM of early-type galaxies, this absorption strength nevertheless exceeds the offset $\text{NaD}_{\text{orig}} - \text{NaD}_{\text{clean}}$ we observe for $\sim 10 \text{ Gyr}$ old SSPs ($\sim 0.3 - 0.5 \text{ \AA}$). On the other hand, a Herschel Space Observatory survey of dust emission at 250, 350, and $500 \mu\text{m}$ across $\sim 22.6\text{K}$ ellipticals detected significant emission in only 13% of the sample (Leńniewska et al. 2023). Early-type galaxies have also been surveyed for both neutral hydrogen and molecular gas, with approximately two-thirds of field early types exhibiting H I masses greater than a few times $10^6 M_{\odot}$, and fewer than 10% of cluster galaxies detected to the same limit (Oosterloo et al. 2010). Molecular gas (traced by CO) is likewise detected in $\approx 20\%$ of the ATLAS^{3D} and MASSIVE samples (Young et al. 2011; Davis et al. 2019), to a gas mass detection limit of 0.1% of the stellar mass. This molecular material is moreover observed to be concentrated toward the centers of the systems (e.g., Alatalo et al. 2013; Davis et al. 2013; Ruffa et al. 2019). Given that both neutral and molecular hydrogen could harbor the Na I ion, it is therefore likely that at least some early types exhibit interstellar Na I D absorption that, when fit with “contaminated” SSP templates, would compensate for the tendency to underestimate $[\text{Na}/\text{Fe}]$. This possibility should be considered in all stellar population synthesis analyses that include Na I D.

4.3.4. Implications for IMF Slope Constraints

$[\text{Na}/\text{Fe}]$ measurements in turn play a role in anchoring spectroscopic constraints on the IMF slope. There are several surface-gravity-sensitive transitions in the rest-frame optical and near-IR that have been explored as IMF indicators, including Na I $\lambda\lambda 8183, 8195$, the FeH $\lambda 9916$ Wing-Ford band, the Ca II $\lambda\lambda 8498, 8542, 8662$ triplet (Wing & Ford 1969; Spinrad & Taylor 1971; Whitford 1977; Faber & French 1980; van Dokkum & Conroy 2010, 2012; Martín-Navarro et al. 2015), and $\text{TiO}_2 \lambda 6230$ (Spiniello et al. 2012). Many recent studies have focused their analyses on the former three sets of transitions, as Na, Fe, and Ca abundances may be tightly constrained from complementary (and IMF-insensitive) transitions (e.g., van Dokkum & Conroy 2010; Smith et al. 2012; Conroy & van Dokkum 2012a; La Barbera et al. 2013; Parikh et al. 2018; La Barbera et al. 2019; Gu et al. 2022). The strength of both Na I $\lambda\lambda 8183, 8195$ and FeH increase with the fraction of dwarf stars (as well as with Na and Fe abundances), while the strength of the Ca triplet increases with the fraction of giant stars. Our suggestion that the presence of ISM contamination in empirical stellar libraries leads to a systematic underestimation of the Na abundance

(assuming the absence of significant interstellar Na I in the host galaxy) implies that, when accounted for, a less bottom-heavy (i.e., more Milky Way-like) IMF will be needed to explain the observed strengths of Na I $\lambda\lambda 8183, 8195$ in massive ellipticals. We further posit that the same (or a greater) degree of ISM contamination could be present in SSP models of lower-mass ellipticals, for which a Milky Way-like IMF is typically derived (e.g., Conroy & van Dokkum 2012b; La Barbera et al. 2013; Parikh et al. 2018). By the same token, the fraction of dwarf stars in these models may need to be reduced in order to avoid the overprediction of Na I $\lambda\lambda 8183, 8195$ for such systems, pushing the models toward bottom-light IMFs. More detailed modeling is required to test whether ISM contamination has had a statistically significant impact on these spectroscopic IMF constraints.

The case for a steeper IMF slope in more massive early-type systems by no means rests solely on [Na/Fe] and Na I. Several independent, corroborating lines of evidence for a variable IMF come from studies relying on dynamical mass constraints from gravitational lensing or galaxy kinematics (e.g. Treu et al. 2010; Thomas et al. 2011c; Cappellari et al. 2012; Lyubenova et al. 2016). Conroy & van Dokkum (2012b) found evidence for significant IMF variation even after excluding Na I lines from their analysis; however, they also found that their derived mass-to-light ratios changed by $\gtrsim 50\%$ as a result. Na I D and Na I $\lambda\lambda 8183, 8195$ thus play a crucial role in setting IMF constraints, including for studies that make use of full spectrum fitting, in part because FeH has confounding sensitivities to [Fe/H], age, and $[\alpha/\text{Fe}]$ (Conroy & van Dokkum 2012b; La Barbera et al. 2013; Parikh et al. 2018). We argue that precision constraints on the IMF slope that rely on analysis of Na I transitions must account for the systematic effects we have elucidated.

5. CONCLUSION

The cool material that pervades the Milky Way’s ISM has long been understood to give rise to Ca II $\lambda\lambda 3934, 3969$ and Na I $\lambda\lambda 5891, 5897$ absorption in optical spectroscopy of stars and QSOs (Hobbs 1969, 1974; Crawford 1992; Sembach et al. 1993; Welty et al. 1996; Welsh et al. 2010; Poznanski et al. 2012; Murga et al. 2015; Bish et al. 2019). We have quantified the impact of interstellar absorption in these transitions on the spectra of 23,771 stars comprising the SDSS-IV MaNGA Stellar Library (Yan et al. 2019; Chen et al. 2020; Abdurro’uf et al. 2022; Hill et al. 2022; Imig et al. 2022; Lazarz et al. 2022). MaStar includes over an order of magnitude more stars than any other extant empirical stellar library, and thus enables population synthesis that ade-

quately captures the diversity of the MaNGA sample of $\sim 10,000$ nearby galaxies (Yan et al. 2019).

Our analysis leverages high-resolution spectroscopic observations of interstellar Ca II and Na I absorption from Sembach et al. (1993), Munari & Zwitter (1997), and Welsh et al. (2010) to develop a model of the equivalent widths of these transitions as a function of stellar distance, Galactic latitude, and the dust reddening of the stellar sightline. We apply this model to the MaStar sample, making use of stellar distances and reddening values available from Green et al. (2019) and Bailer-Jones et al. (2021). We find that the predicted equivalent widths of ISM absorption are roughly uniformly distributed across the ranges $0 \text{ \AA} < W^{\text{ISM}}(\text{Ca II K}) < 0.6 \text{ \AA}$, $0 \text{ \AA} < W^{\text{ISM}}(\text{Na I } 5891) < 1.0 \text{ \AA}$, and $0 \text{ \AA} < W^{\text{ISM}}(\text{Na I } 5897) < 0.7 \text{ \AA}$ for stars with effective temperatures $T_{\text{eff}} > 7610 \text{ K}$, whereas cooler stars are predicted to have median interstellar absorption strengths of $W^{\text{ISM}}(\text{Ca II K}) = 0.11 \text{ \AA}$, $W^{\text{ISM}}(\text{Na I } 5891) = 0.15 \text{ \AA}$, and $W^{\text{ISM}}(\text{Na I } 5897) = 0.09 \text{ \AA}$.

We then use this simple model to identify a subset of 6342 “low-ISM” stars for which the interstellar contamination level is minimal ($W^{\text{ISM}}(\text{Ca II K}) < 0.07 \text{ \AA}$ and $W^{\text{ISM}}(\text{Na I D}) < 0.05 \text{ \AA}$). For 12,110 of the remaining stars, we remove interstellar contamination from each star by identifying a subset of the low-ISM sample with similar stellar parameters, coadding the spectra in this subset, and replacing the Na I D profile in the affected spectrum with that in the coadd. We execute the same replacement of Ca II H&K only in the very small subset of these stars with $T_{\text{eff}} > 9000 \text{ K}$, as we found that this replacement does not yield any systematic reduction in the Ca II K equivalent widths in cooler stars. For those 738 stars for which we could not identify a low-ISM replacement subset that was sufficiently close in stellar parameter space and which have $T_{\text{eff}} > 9000 \text{ K}$, we select well-matched stars from the theoretical stellar library of Bohlin et al. (2017) to replace the Ca II H & K and Na I D spectral regions.

This procedure results in a mean reduction in $W(\text{Ca II K})$ of 0.4, 0.7, and 0.5 \AA for A, B, and O spectral types, and a mean reduction in $W(\text{Na I D})$ of 0.1 – 0.2 \AA for stars with $T_{\text{eff}} < 7610 \text{ K}$, and of 0.6, 1.1, and 1.0 \AA for A, B, and O spectral types. We additionally find that the degree of ISM contamination of Na I D is larger in giant stars (having $\log g < 4$), and that it systematically increases with stellar [Fe/H] in these giants. Our catalog of “cleaned” stellar spectra is publicly available via Zenodo with doi:10.5281/zenodo.14014915. We also make public a hierarchically-clustered stellar template library constructed from our cleaned MaStar spectra that is

suitable for continuum modeling of external galaxy spectroscopy.¹⁴

Finally, we demonstrate the impact of this interstellar absorption on stellar population analyses by constructing simple stellar population (SSP) templates from both the “cleaned” and original stellar spectra. We find that MaStar SSPs constructed from the original spectra overestimate the strength of Ca II K absorption by $\gtrsim 20\%$ in relatively young ($\lesssim 400$ Myr) stellar populations at solar metallicity. We further demonstrate that the presence of interstellar Na I absorption in SSP templates constructed from the original MaStar spectra implies (1) a dramatic overestimate of the strength of stellar Na I D absorption in starbursting systems (by $\gtrsim 50\%$); and (2) an overestimate of the strength of the NaD index in older stellar populations ($\gtrsim 10$ Gyr) by $\gtrsim 10\%$. The former effect would systematically reduce the equivalent width attributed to the host’s ISM, inflows, and outflows in “down-the-barrel” analyses of Na I D kinematics (e.g., [Chen et al. 2010b](#); [Roberts-Borsani & Saintonge 2019](#); [Avery et al. 2022](#)), and would do so to a more extreme degree in the youngest starburst systems. The latter effect would lead to a systematic underestimation of [Na/Fe] in early-type galaxies (under the assumption that the galaxies themselves do not harbor significant interstellar Na I), potentially weakening the requirement for a steep IMF slope to match near-IR Na I absorption line strengths (e.g., [Conroy & van Dokkum 2012b](#); [La Barbera et al. 2013](#); [Martín-Navarro et al. 2015](#); [Parikh et al. 2018](#)).

Our findings suggest that the Milky Way’s ISM is latent in any empirical stellar library which lacks the spectral resolution to distinguish stellar from interstellar absorption (e.g., [Le Borgne et al. 2003](#); [Valdes et al. 2004](#); [Sánchez-Blázquez et al. 2006](#)). Our model for interstellar absorption equivalent widths may be used to estimate the magnitude of these effects on previous analyses. Moreover, our “cleaned” SSP templates are publicly available¹⁵, and may now be used to quantitatively assess the systematic effects of interstellar Ca II and Na I absorption on stellar age, [Na/Fe], and IMF slope constraints.

ACKNOWLEDGMENTS

¹⁴ The hierarchically-clustered templates are available at https://github.com/sdss/mangadap/tree/4.2.0/mangadap/data/spectral_templates/mastarhc_v2_noism.

¹⁵ The full set of SSP templates is available at <https://doi.org/10.5281/zenodo.14807331>. A subset of the SSP templates that have been modified for use with the MaNGA Data Analysis Pipeline is available at https://github.com/sdss/mangadap/tree/4.2.0/mangadap/data/spectral_templates/mastar_ssp_noism_v1.0.

The authors are grateful for support for this project from NSF grants AST-1715630, AST-1715898, and AST-2009417. R.Y. acknowledges the support of two grants from the Research Grants Council of the Hong Kong Special Administrative Region, China (Project No: CUHK 14303123, CUHK 14302522) and a grant from the National Science Foundation of China (No.12373008). R.Y. also acknowledges support from the Hong Kong Global STEM Scholar scheme, by the Hong Kong Jockey Club Charities Trust through the JC STEM Lab of Astronomical Instrumentation.

We thank Dan Welty for sharing his Milky Way absorption line data with us. We wish to also thank the MaNGA team for their extraordinary efforts to obtain and process this exceptionally high-quality dataset. It is a pleasure to thank Scott Trager and Else Starkenburg for sharing their extensive expertise in stellar spectroscopy which led to improvements in this manuscript. K.H.R.R. thanks the astrophysicists at the University of Pittsburgh for their warm hospitality during her sabbatical stay, during which much of this manuscript was written, and thanks Evan Schneider and Jessica Werk for numerous helpful conversations and writing support. The authors also wish to acknowledge the anonymous referee, who provided valuable feedback that improved this work.

Funding for the Sloan Digital Sky Survey IV has been provided by the Alfred P. Sloan Foundation, the U.S. Department of Energy Office of Science, and the Participating Institutions.

SDSS-IV acknowledges support and resources from the Center for High Performance Computing at the University of Utah. The SDSS website is www.sdss4.org.

SDSS-IV is managed by the Astrophysical Research Consortium for the Participating Institutions of the SDSS Collaboration including the Brazilian Participation Group, the Carnegie Institution for Science, Carnegie Mellon University, Center for Astrophysics Harvard & Smithsonian, the Chilean Participation Group, the French Participation Group, Instituto de Astrofísica de Canarias, The Johns Hopkins University, Kavli Institute for the Physics and Mathematics of the Universe (IPMU) / University of Tokyo, the Korean Participation Group, Lawrence Berkeley National Laboratory, Leibniz Institut für Astrophysik Potsdam (AIP), Max-Planck-Institut für Astronomie (MPIA Heidelberg), Max-Planck-Institut für Astrophysik (MPA Garching), Max-Planck-Institut für Extraterrestrische Physik (MPE), National Astronomical Observatories of China, New Mexico State University, New York University, University of Notre Dame, Observatório Nacional / MCTI, The Ohio State University, Pennsylva-

nia State University, Shanghai Astronomical Observatory, United Kingdom Participation Group, Universidad Nacional Autónoma de México, University of Arizona, University of Colorado Boulder, University of Oxford, University of Portsmouth, University of Utah, University of Virginia, University of Washington, University of Wisconsin, Vanderbilt University, and Yale University.

APPENDIX

A. TELLURIC CONTAMINATION OF THE NA I D SPECTRAL REGION

While absorption features arising in Earth’s atmosphere are most prominent at wavelengths $\lambda > 6800 \text{ \AA}$, there are several comparatively weak telluric features in the wavelength range $5885 \text{ \AA} < \lambda_{\text{air}} < 5906 \text{ \AA}$ ¹⁶ (e.g., Lallement et al. 1993; Chen et al. 2014; Sandford et al. 2023). At the $\mathcal{R} \sim 1800$ resolution of MaStar, these features are fully blended with the lines of the Na I D doublet and cannot be removed using traditional techniques for telluric correction. As described in Yan et al. (2016) and Yan et al. (2019), telluric correction was performed for MaStar by fitting a high-order cubic basis spline (B-spline) function to the ratio of fluxes observed in standard stars to a matching theoretical stellar template. However, these high-frequency corrections were performed only in spectral regions with severe telluric contamination (all redward of 6842 \AA). In all other spectral regions, the flux calibration vector was derived in two steps. First, a large sample of standard star observations was coadded and divided by a matching theoretical template. Complex spectral regions (including Balmer transitions, Ca II H&K, and Na I D) were masked, and then a B-spline with break points spaced every 10 pixels was fit to this ratio to derive an average calibration vector. A time-dependent correction to this curve was determined by fitting a lower-order B-spline (with break points spaced every 160 pixels) to the standard star spectra on individual plates (again normalized by matching spectral templates), and applied in addition to the average calibration vector.

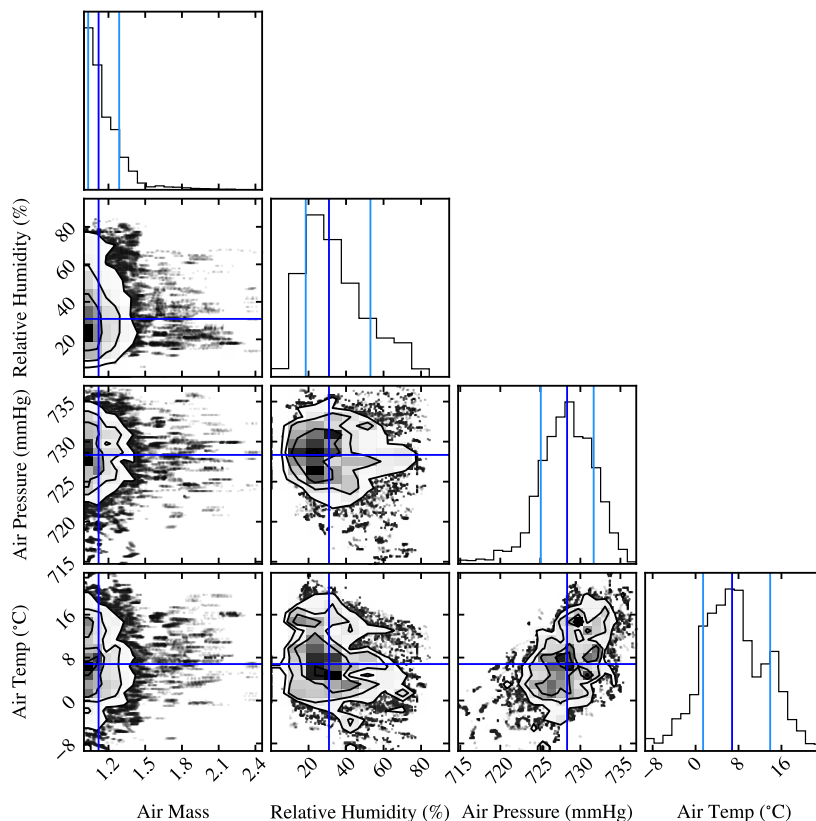


Figure 21. Distributions of the atmospheric conditions for all high-quality exposures used in “good” visit spectra in the MaStar library. This includes all spectra with no `MASTAR_QUAL` flags set. The median of each distribution is indicated in dark blue, with the 16th- and 84th-percentile values indicated in light blue.

¹⁶ <https://sites.astro.caltech.edu/~tb/makee/>

This procedure in effect leaves all telluric absorption features in the final stellar spectra near Na I D. We investigate the potential impact this may have on our analysis as follows. First, because telluric absorption is a strong function of the atmospheric conditions (i.e., air temperature, air pressure, relative humidity) and air mass, we assemble this information for each of the high-quality exposures comprising the “good” MaStar visit spectra¹⁷ as described in the SDSS-IV DR17 documentation.¹⁸ We show the distributions of these conditions in Figure 21. The median values of the air mass, relative humidity, air pressure, and air temperature are 1.12, 31%, 728 mmHg, and 6.8°C, respectively.

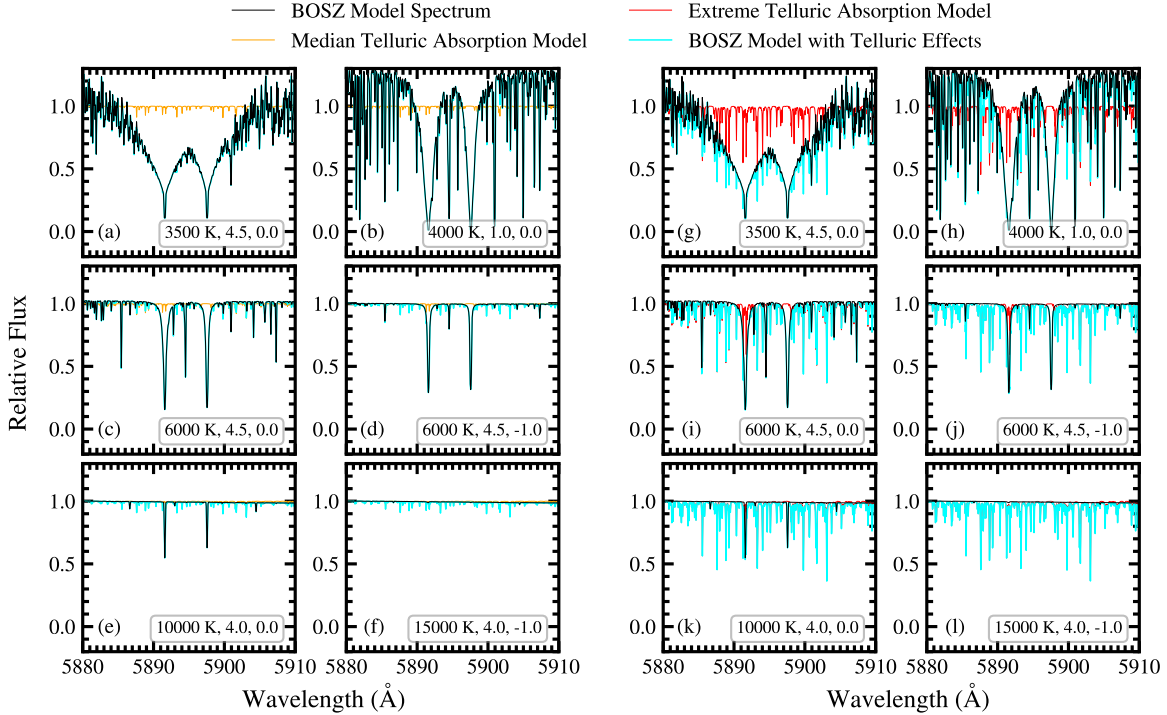


Figure 22. *Panels (a)-(f):* The atmospheric transmission spectrum predicted by TelFit/LBLRTM for Apache Point Observatory for an air mass = 1.1, 30% relative humidity, atmospheric pressure = 730 mmHg, and an air temperature of 5.5°C is shown in orange. The black spectra show a selection of six BOSZ theoretical stellar templates calculated at $\mathcal{R} = 300,000$. The T_{eff} , $\log g$, and $[M/H]$ values for each template are printed in the lower right of each panel. We have rebinned the telluric model to match that of the BOSZ templates, and show the product of the two in cyan. *Panels (g)-(l):* An APO TelFit/LBLRTM atmospheric transmission spectrum for an air mass = 1.6, 70% relative humidity, atmospheric pressure = 730 mmHg, and an air temperature of 20.5°C is shown in red. The black spectra are the same as in the corresponding panel at left. The cyan spectrum in each panel shows the product of the theoretical template and this more extreme telluric absorption.

We then use the TelFit Python package¹⁹ to calculate a grid of telluric atmospheric transmission spectra appropriate for these conditions. TelFit is a wrapper for the LBLRTM FORTRAN code (Clough et al. 1992, 2005), a radiative transfer modeling code that draws from the HITRAN database of molecular spectroscopic parameters (Gordon et al. 2022). The grid contains atmospheric transmission spectra for humidities in the range 10 – 70%, air pressures in the range 720 – 735 mmHg, air temperatures in the range $-4.5^{\circ}\text{C} - +20.5^{\circ}\text{C}$, and air masses between 1.0 and 1.7. These ranges encompass the 2.5th- and 97.5th-percentile values of the distributions shown in Figure 21.

We show two examples of these predictions in Figure 22. In the left-hand set of panels ((a)-(f)), a model that assumes an air mass = 1.1, atmospheric pressure = 730 mmHg, 30% relative humidity, and an air temperature of 5.5°C is shown in orange. For comparison, we also show a selection of six BOSZ theoretical stellar spectra calculated with $\mathcal{R} = 300,000$ for a broad range of stellar parameters (approximately following the locations in parameter space

¹⁷ This includes all exposures with the USED_IN_VISIT flag set, for all visit spectra with MJDQUAL bits set to indicate high quality.

¹⁸ <https://www.sdss4.org/dr17/mastar/mastar-spectra/>

¹⁹ <https://telfit.readthedocs.io/en/latest/>

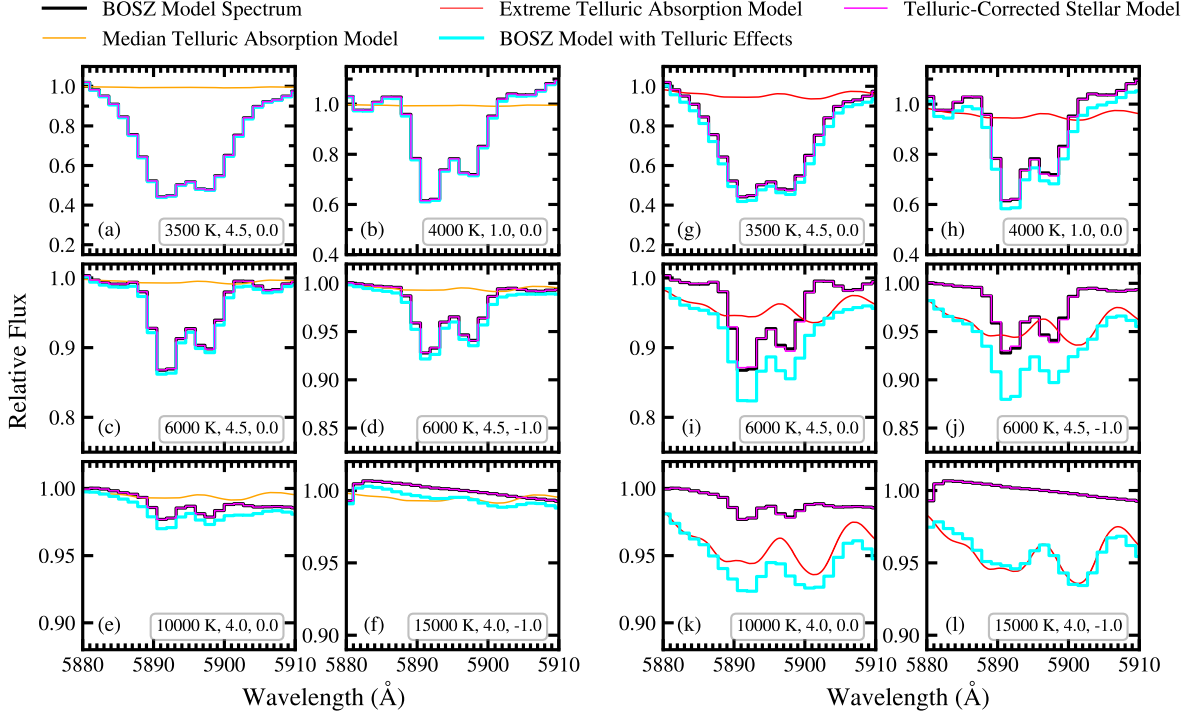


Figure 23. The BOSZ model spectra (black), telluric absorption models (orange and red), and combined spectra (cyan) shown in Figure 22, smoothed to the resolution of the MaStar 99.5th-percentile LSF. The magenta spectra show the ratio of each smoothed combined spectrum and the smoothed telluric absorption model. The magenta spectra lie nearly exactly on top of the original BOSZ models, indicating that this simple approach to telluric correction is effective.

numbered in Figure 8). The product of each of these models and the atmospheric transmission (telluric) spectrum is in principle representative of the observed spectrum in these atmospheric conditions. We have rebinned the telluric spectrum to match that of the BOSZ templates, and show their products in cyan. A preponderance of weak telluric features across this spectral region, greater in strength than the stellar Na I D absorption in one case, is evident. In the right-hand set of panels ((g)-(l)), we show a telluric absorption model calculated assuming more extreme conditions: we adopt an air mass = 1.6, 70% relative humidity, and an air temperature of 20.5°C. Such atmospheric conditions were very rare during the course of the MaStar observations, but are representative of the extremes of the distributions shown in Figure 21. The product of each BOSZ template and this telluric model is again shown in cyan. In this case, the telluric absorption contributes significant equivalent width, and dominates over that produced by the two hottest stars.

To estimate the impact of these features on the Na I D equivalent widths we observe in the MaStar spectra, we repeat the following procedure for each of these stellar templates at each telluric model grid point. First, we smooth the BOSZ models and the product of the BOSZ and telluric models to the 99.5th-percentile spectral resolution curve of MaStar. We then rebin the BOSZ and product spectra to a wavelength bin width matching that of the MaStar catalog (i.e., $1.357 \text{ \AA pix}^{-1}$ near Na I D). The results of this exercise for the telluric models displayed in Figure 22 are shown in Figure 23.

We then establish the continuum level around the Na I D feature by fitting a linear model to the flux in the spectral windows $5881.0 \text{ \AA} < \lambda < 5885.0 \text{ \AA}$ and $5904.0 \text{ \AA} < \lambda < 5908.0 \text{ \AA}$ (as is done in our MaStar analysis), noting that this level is affected by the overall strength of the telluric absorption. Finally, we measure the boxcar equivalent width in the spectral window $5885.0 \text{ \AA} < \lambda < 5904.0 \text{ \AA}$ and compute the difference between that measured in the product spectrum and that measured in the original spectrum of each star (ΔW_{tell}).

We summarize these results in Figure 24. Each contour indicates the range in ΔW_{tell} values exhibited by the six BOSZ stellar templates for telluric models with the specified relative humidity and air temperature as a function of the air mass. We find that at very low humidities (10%), the strength of these features remains $< 0.1 \text{ \AA}$ at all

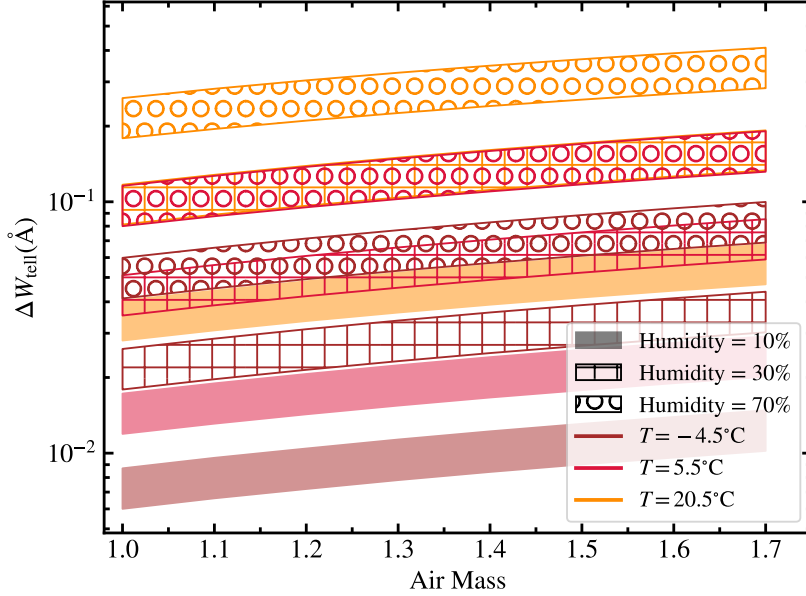


Figure 24. Equivalent width enhancement due to telluric absorption within the Na I D spectral window predicted by TelFit/LBLRTM for APO. All models shown adopt atmospheric pressures of 730 mmHg. Each contour shows the full range of equivalent width enhancements exhibited by the BOSZ stellar templates analyzed in this section as a function of the air mass. Solid, hatched, and circle-hatched contours show results for models assuming 10%, 30%, and 70% relative humidity, respectively. At each of these humidity levels, we show results for models adopting air temperatures of -4.5°C in brown, 5.5°C in red, and 20.5°C in orange.

air masses and temperatures covered in the grid. Higher humidities at warm temperatures can yield a significantly stronger telluric contribution (e.g., up to $0.2 - 0.4 \text{ \AA}$ for 70% humidity at 20.5°C). However, the model that best represents the median atmospheric conditions during the MaStar observations (with 30% relative humidity, an air temperature of 5.5° , and an air pressure of 730 mmHg) produces a $\Delta W_{\text{tell}} \lesssim 0.06 \text{ \AA}$ at air masses < 1.2 . Among the 204,185 exposures included in Figure 21, 4.6% were obtained at $>70\%$ relative humidity, and 2.1% were obtained at $>70\%$ relative humidity with air temperatures $>5.5^{\circ}\text{C}$. Fewer than 1% of all exposures were taken in air temperatures $>20.5^{\circ}\text{C}$, and all of these latter exposures were obtained with relative humidities $<39\%$.

Together, these findings imply that the contribution of telluric absorption to our measured Na I equivalent widths is negligible in comparison to the effect of ISM contamination for most of the MaStar sightlines, but that telluric absorption may be significant in a small minority of cases. At the same time, the degree of telluric absorption should not have any dependence on the reddening or distance to the target stars, as is the case for interstellar absorption. Telluric absorption will therefore introduce an additional, very slight systematic enhancement of Na I equivalent widths across our sample as a whole.

We do not attempt to correct for this enhancement. However, we have found that it is possible to recover the intrinsic Na I profile of a star when observed at low spectral resolution in the case that the telluric absorption model is known. For each telluric model + BOSZ template combination shown in Figure 23 (in cyan), we smooth the telluric model to the same spectral resolution as the data, and then divide the product spectrum by the smoothed telluric. The results are shown with the magenta spectra, which in all cases overlap completely with the original, smoothed BOSZ spectra. While this approach is not mathematically sound (as the observed spectrum is convolved with the LSF after the starlight is absorbed by the atmosphere), it nevertheless yields the same Na I equivalent widths as are measured in the original smoothed BOSZ spectra to within $<0.03 \text{ \AA}$. It should therefore be feasible to correct the Na I region of low-resolution spectroscopy for telluric effects by constraining the atmospheric absorption model using “clean” spectral regions at longer wavelengths.

B. CA II AND NA I IN HIERARCHICALLY-CLUSTERED MASTAR TEMPLATES

In Figure 25 we present the Ca II K and Na I profiles for the hierarchically-clustered templates described in Section 3.5 which were not shown in Figure 16.

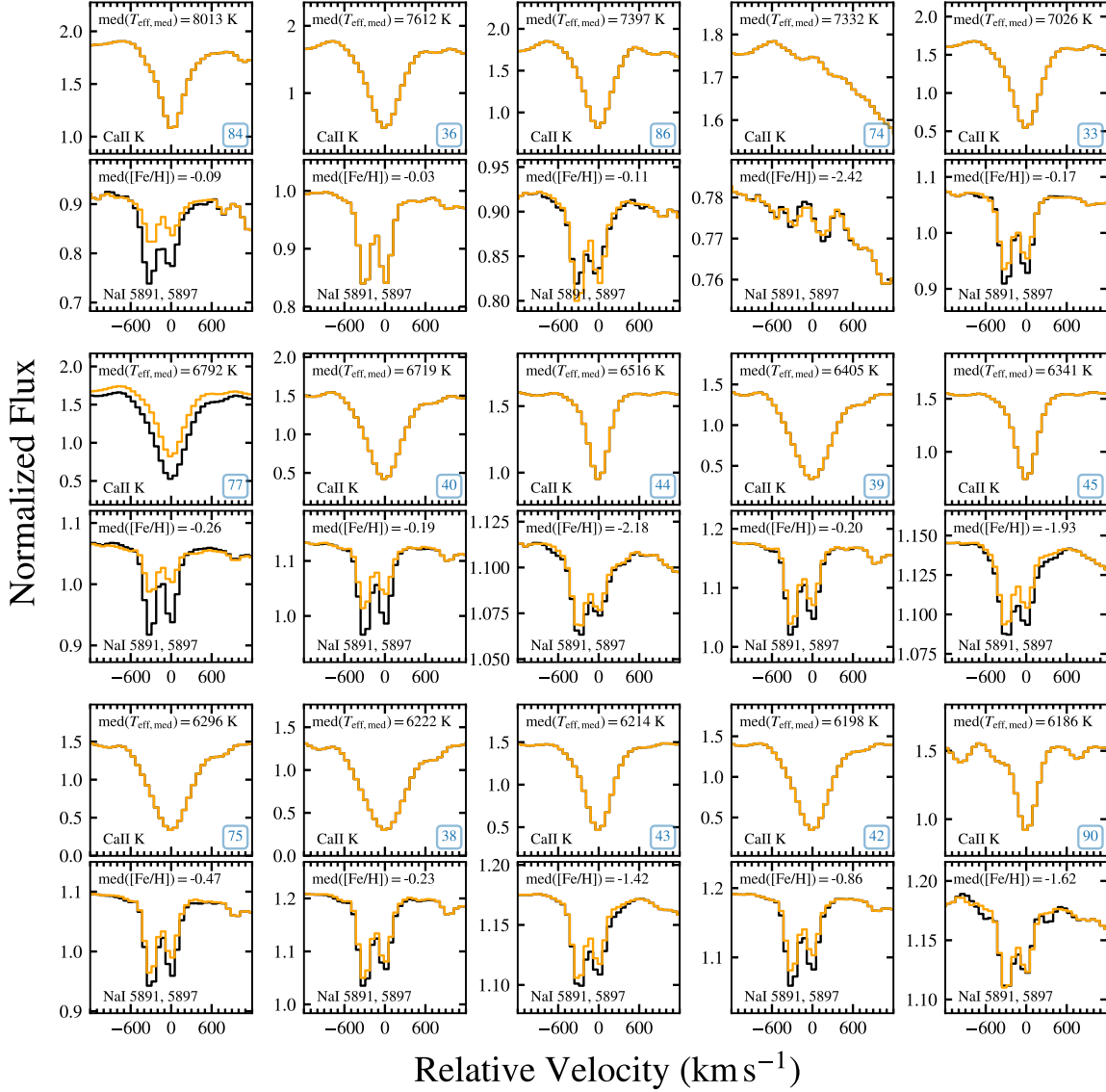


Figure 25. Comparison of hierarchically-clustered MaStar spectral templates constructed without correction for ISM absorption (black) and from our “cleaned” spectral sample (orange). This is a multipage continuation of Figure 16. Each pair of stacked panels shows the same template at the locations of the Ca II K and Na I $\lambda\lambda 5891, 5897$ transitions on top and bottom, respectively. Velocities are computed relative to the Ca II K $\lambda 3934$ and Na I $\lambda 5897$ rest wavelengths. The templates have been ordered according to the median $T_{\text{eff,med}}$ value of the stars used in each. This value, along with the median $[\text{Fe}/\text{H}]$ value, is noted in each panel pair. The cluster ID of each template is indicated in blue.

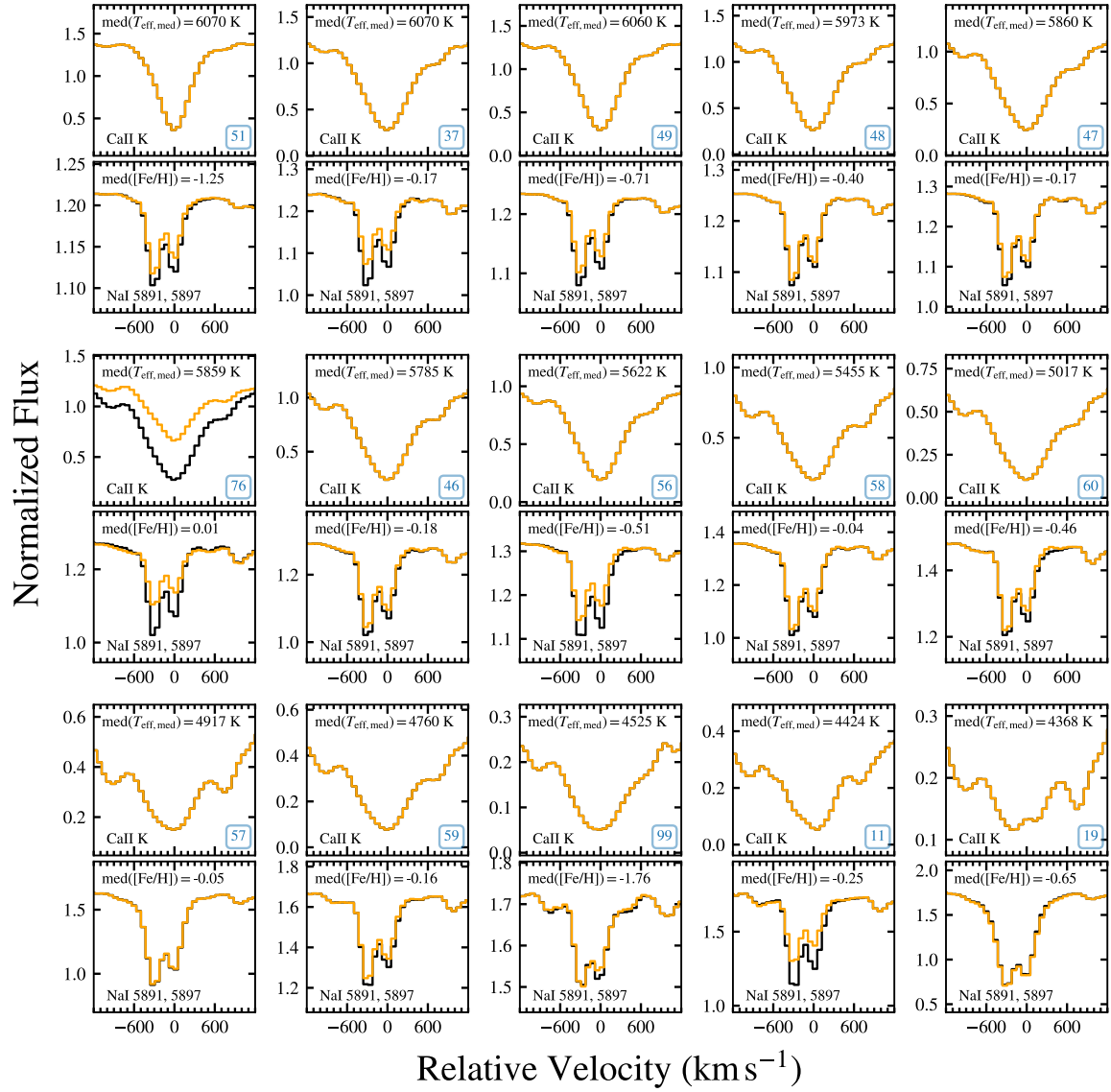


Figure 25. – continued

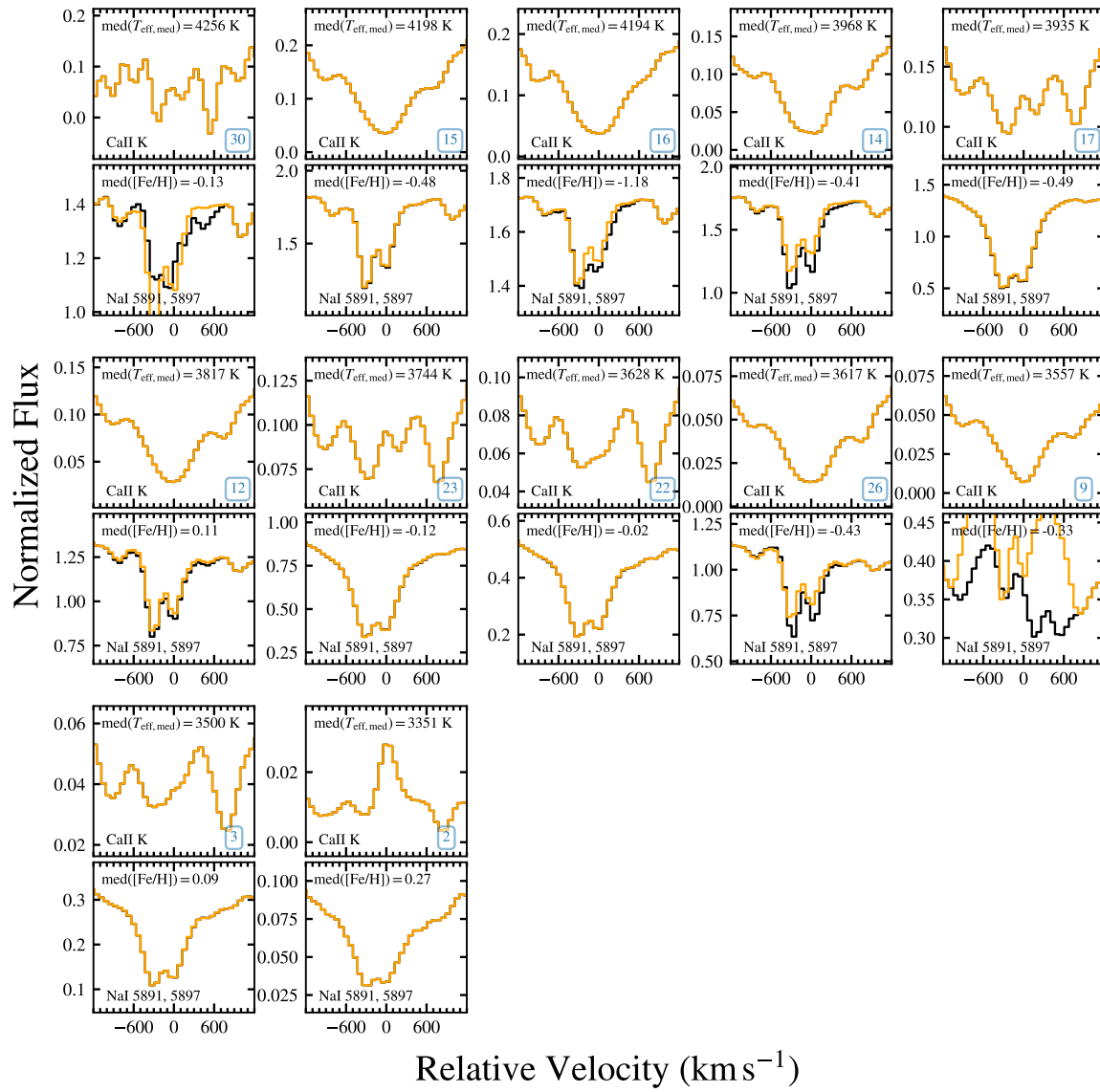


Figure 25. – continued

REFERENCES

- Abdurro'uf, Accetta, K., Aerts, C., et al. 2022, *ApJS*, 259, 35, doi: [10.3847/1538-4365/ac4414](https://doi.org/10.3847/1538-4365/ac4414)
- Alatalo, K., Davis, T. A., Bureau, M., et al. 2013, *MNRAS*, 432, 1796, doi: [10.1093/mnras/sts299](https://doi.org/10.1093/mnras/sts299)
- Alton, P. D., Smith, R. J., & Lucey, J. R. 2017, *MNRAS*, 468, 1594, doi: [10.1093/mnras/stx464](https://doi.org/10.1093/mnras/stx464)
- Avery, C. R., Wuyts, S., Förster Schreiber, N. M., et al. 2022, *MNRAS*, 511, 4223, doi: [10.1093/mnras/stac190](https://doi.org/10.1093/mnras/stac190)
- Bailer-Jones, C. A. L., Rybizki, J., Fouesneau, M., Demleitner, M., & Andrae, R. 2021, *AJ*, 161, 147, doi: [10.3847/1538-3881/abd806](https://doi.org/10.3847/1538-3881/abd806)
- Baron, D., Stern, J., Poznanski, D., & Netzer, H. 2016, *ApJ*, 832, 8, doi: [10.3847/0004-637X/832/1/8](https://doi.org/10.3847/0004-637X/832/1/8)
- Belfiore, F., Maiolino, R., Tremonti, C., et al. 2017, *MNRAS*, 469, 151, doi: [10.1093/mnras/stx789](https://doi.org/10.1093/mnras/stx789)
- Belfiore, F., Westfall, K. B., Schaefer, A., et al. 2019, *AJ*, 158, 160, doi: [10.3847/1538-3881/ab3e4e](https://doi.org/10.3847/1538-3881/ab3e4e)
- Ben Bekhti, N., Richter, P., Westmeier, T., & Murphy, M. T. 2008, *A&A*, 487, 583, doi: [10.1051/0004-6361:20079067](https://doi.org/10.1051/0004-6361:20079067)
- Ben Bekhti, N., Winkel, B., Richter, P., et al. 2012, *A&A*, 542, A110, doi: [10.1051/0004-6361/201118673](https://doi.org/10.1051/0004-6361/201118673)
- Bensby, T., Feltzing, S., & Oey, M. S. 2014, *A&A*, 562, A71, doi: [10.1051/0004-6361/201322631](https://doi.org/10.1051/0004-6361/201322631)
- Bensby, T., Feltzing, S., Gould, A., et al. 2017, *A&A*, 605, A89, doi: [10.1051/0004-6361/201730560](https://doi.org/10.1051/0004-6361/201730560)
- Bernardi, M., Domínguez Sánchez, H., Sheth, R. K., Brownstein, J. R., & Lane, R. R. 2023, *MNRAS*, 518, 4713, doi: [10.1093/mnras/stac3287](https://doi.org/10.1093/mnras/stac3287)
- Bernardi, M., Nichol, R. C., Sheth, R. K., Miller, C. J., & Brinkmann, J. 2006, *AJ*, 131, 1288, doi: [10.1086/499522](https://doi.org/10.1086/499522)
- Bish, H. V., Werk, J. K., Prochaska, J. X., et al. 2019, *ApJ*, 882, 76, doi: [10.3847/1538-4357/ab3414](https://doi.org/10.3847/1538-4357/ab3414)
- Bloom, J. V., Croom, S. M., Bryant, J. J., et al. 2017, *MNRAS*, 472, 1809, doi: [10.1093/mnras/stx1701](https://doi.org/10.1093/mnras/stx1701)
- Bohlin, R. C., Mészáros, S., Fleming, S. W., et al. 2017, *AJ*, 153, 234, doi: [10.3847/1538-3881/aa6ba9](https://doi.org/10.3847/1538-3881/aa6ba9)
- Borisov, S. B., Chilingarian, I. V., Rubtsov, E. V., et al. 2023, *ApJS*, 266, 11, doi: [10.3847/1538-4365/acc321](https://doi.org/10.3847/1538-4365/acc321)
- Bruzual, A. G. 1983, *ApJ*, 273, 105, doi: [10.1086/161352](https://doi.org/10.1086/161352)
- Bruzual, G., & Charlot, S. 2003, *MNRAS*, 344, 1000, doi: [10.1046/j.1365-8711.2003.06897.x](https://doi.org/10.1046/j.1365-8711.2003.06897.x)
- Bryant, J. J., Croom, S. M., van de Sande, J., et al. 2019, *MNRAS*, 483, 458, doi: [10.1093/mnras/sty3122](https://doi.org/10.1093/mnras/sty3122)
- Bundy, K., Bershad, M. A., Law, D. R., et al. 2015, *ApJ*, 798, 7, doi: [10.1088/0004-637X/798/1/7](https://doi.org/10.1088/0004-637X/798/1/7)
- Burstein, D., Faber, S. M., Gaskell, C. M., & Krumm, N. 1984, *ApJ*, 287, 586, doi: [10.1086/162718](https://doi.org/10.1086/162718)
- Burstein, D., Faber, S. M., & Gonzalez, J. J. 1986, *AJ*, 91, 1130, doi: [10.1086/114090](https://doi.org/10.1086/114090)
- Byrne, C. M., & Stanway, E. R. 2023, *MNRAS*, 521, 4995, doi: [10.1093/mnras/stad832](https://doi.org/10.1093/mnras/stad832)
- Cappellari, M. 2016, *ARA&A*, 54, 597, doi: [10.1146/annurev-astro-082214-122432](https://doi.org/10.1146/annurev-astro-082214-122432)
- . 2017, *MNRAS*, 466, 798, doi: [10.1093/mnras/stw3020](https://doi.org/10.1093/mnras/stw3020)
- Cappellari, M., Emsellem, E., Krajnović, D., et al. 2011, *MNRAS*, 413, 813, doi: [10.1111/j.1365-2966.2010.18174.x](https://doi.org/10.1111/j.1365-2966.2010.18174.x)
- Cappellari, M., McDermid, R. M., Alatalo, K., et al. 2012, *Nature*, 484, 485, doi: [10.1038/nature10972](https://doi.org/10.1038/nature10972)
- Cassisi, S., Castellani, M., & Castellani, V. 1997a, *A&A*, 317, 108, doi: [10.48550/arXiv.astro-ph/9603023](https://doi.org/10.48550/arXiv.astro-ph/9603023)
- Cassisi, S., Castellani, V., Ciarcelluti, P., Piotto, G., & Zoccali, M. 2000, *MNRAS*, 315, 679, doi: [10.1046/j.1365-8711.2000.03457.x](https://doi.org/10.1046/j.1365-8711.2000.03457.x)
- Cassisi, S., degl'Innocenti, S., & Salaris, M. 1997b, *MNRAS*, 290, 515, doi: [10.1093/mnras/290.3.515](https://doi.org/10.1093/mnras/290.3.515)
- Castelli, F., & Kurucz, R. L. 2003, in *Modelling of Stellar Atmospheres*, ed. N. Piskunov, W. W. Weiss, & D. F. Gray, Vol. 210, A20. <https://arxiv.org/abs/astro-ph/0405087>
- Cazzoli, S., Arribas, S., Colina, L., et al. 2014, *A&A*, 569, A14, doi: [10.1051/0004-6361/201323296](https://doi.org/10.1051/0004-6361/201323296)
- Chen, H.-W., Helsby, J. E., Gauthier, J.-R., et al. 2010a, *ApJ*, 714, 1521, doi: [10.1088/0004-637X/714/2/1521](https://doi.org/10.1088/0004-637X/714/2/1521)
- Chen, Y.-M., Tremonti, C. A., Heckman, T. M., et al. 2010b, *AJ*, 140, 445, doi: [10.1088/0004-6256/140/2/445](https://doi.org/10.1088/0004-6256/140/2/445)
- Chen, Y.-P., Trager, S. C., Peletier, R. F., et al. 2014, *A&A*, 565, A117, doi: [10.1051/0004-6361/201322505](https://doi.org/10.1051/0004-6361/201322505)
- Chen, Y.-P., Yan, R., Maraston, C., et al. 2020, *ApJ*, 899, 62, doi: [10.3847/1538-4357/ab9f35](https://doi.org/10.3847/1538-4357/ab9f35)
- Cid Fernandes, R., Mateus, A., Sodré, L., Stasińska, G., & Gomes, J. M. 2005, *MNRAS*, 358, 363, doi: [10.1111/j.1365-2966.2005.08752.x](https://doi.org/10.1111/j.1365-2966.2005.08752.x)
- Clemens, M. S., Bressan, A., Nikolic, B., et al. 2006, *MNRAS*, 370, 702, doi: [10.1111/j.1365-2966.2006.10530.x](https://doi.org/10.1111/j.1365-2966.2006.10530.x)
- Clough, S. A., Iacono, M. J., & Moncet, J.-L. 1992, *J. Geophys. Res.*, 97, 15,761, doi: [10.1029/92JD01419](https://doi.org/10.1029/92JD01419)
- Clough, S. A., Shephard, M. W., Mlawer, E. J., et al. 2005, *JQSRT*, 91, 233, doi: [10.1016/j.jqsrt.2004.05.058](https://doi.org/10.1016/j.jqsrt.2004.05.058)
- Coelho, P., Barbuy, B., Meléndez, J., Schiavon, R. P., & Castilho, B. V. 2005, *A&A*, 443, 735, doi: [10.1051/0004-6361:20053511](https://doi.org/10.1051/0004-6361:20053511)
- Coelho, P. R. T. 2014, *MNRAS*, 440, 1027, doi: [10.1093/mnras/stu365](https://doi.org/10.1093/mnras/stu365)
- Concas, A., Popesso, P., Brusa, M., Mainieri, V., & Thomas, D. 2019, *A&A*, 622, A188, doi: [10.1051/0004-6361/201732152](https://doi.org/10.1051/0004-6361/201732152)

- Conroy, C. 2013, *ARA&A*, 51, 393,
doi: [10.1146/annurev-astro-082812-141017](https://doi.org/10.1146/annurev-astro-082812-141017)
- Conroy, C., Graves, G. J., & van Dokkum, P. G. 2014, *ApJ*, 780, 33, doi: [10.1088/0004-637X/780/1/33](https://doi.org/10.1088/0004-637X/780/1/33)
- Conroy, C., & van Dokkum, P. 2012a, *ApJ*, 747, 69,
doi: [10.1088/0004-637X/747/1/69](https://doi.org/10.1088/0004-637X/747/1/69)
- Conroy, C., & van Dokkum, P. G. 2012b, *ApJ*, 760, 71,
doi: [10.1088/0004-637X/760/1/71](https://doi.org/10.1088/0004-637X/760/1/71)
- Conroy, C., Villaume, A., van Dokkum, P. G., & Lind, K. 2018, *ApJ*, 854, 139, doi: [10.3847/1538-4357/aaab49](https://doi.org/10.3847/1538-4357/aaab49)
- Couch, W. J., & Sharples, R. M. 1987, *MNRAS*, 229, 423,
doi: [10.1093/mnras/229.3.423](https://doi.org/10.1093/mnras/229.3.423)
- Crawford, I. A. 1992, *MNRAS*, 259, 47,
doi: [10.1093/mnras/259.1.47](https://doi.org/10.1093/mnras/259.1.47)
- Crowther, P. A. 2022, arXiv e-prints, arXiv:2207.08690.
<https://arxiv.org/abs/2207.08690>
- Davis, T. A., Greene, J. E., Ma, C.-P., et al. 2019, *MNRAS*, 486, 1404, doi: [10.1093/mnras/stz871](https://doi.org/10.1093/mnras/stz871)
- Davis, T. A., Alatalo, K., Bureau, M., et al. 2013, *MNRAS*, 429, 534, doi: [10.1093/mnras/sts353](https://doi.org/10.1093/mnras/sts353)
- den Brok, M., Krajnović, D., Emsellem, E., et al. 2024, *MNRAS*, 530, 3278, doi: [10.1093/mnras/stae912](https://doi.org/10.1093/mnras/stae912)
- Dressler, A., & Gunn, J. E. 1983, *ApJ*, 270, 7,
doi: [10.1086/161093](https://doi.org/10.1086/161093)
- Eldridge, J. J., Stanway, E. R., Xiao, L., et al. 2017, *PASA*, 34, e058, doi: [10.1017/pasa.2017.51](https://doi.org/10.1017/pasa.2017.51)
- Faber, S. M. 1972, *A&A*, 20, 361
- Faber, S. M., & French, H. B. 1980, *ApJ*, 235, 405,
doi: [10.1086/157644](https://doi.org/10.1086/157644)
- Feldmeier-Krause, A., Lonoce, I., & Freedman, W. L. 2021, *ApJ*, 923, 65, doi: [10.3847/1538-4357/ac281e](https://doi.org/10.3847/1538-4357/ac281e)
- Fitzpatrick, E. L., Massa, D., Gordon, K. D., Bohlin, R., & Clayton, G. C. 2019, *ApJ*, 886, 108,
doi: [10.3847/1538-4357/ab4c3a](https://doi.org/10.3847/1538-4357/ab4c3a)
- Foreman-Mackey, D., Hogg, D. W., Lang, D., & Goodman, J. 2013, *PASP*, 125, 306, doi: [10.1086/670067](https://doi.org/10.1086/670067)
- Franx, M., & Illingworth, G. 1990, *ApJL*, 359, L41,
doi: [10.1086/185791](https://doi.org/10.1086/185791)
- Gaia Collaboration, Schultheis, M., Zhao, H., et al. 2023a, *A&A*, 680, A38, doi: [10.1051/0004-6361/202347103](https://doi.org/10.1051/0004-6361/202347103)
- Gaia Collaboration, Vallenari, A., Brown, A. G. A., et al. 2023b, *A&A*, 674, A1, doi: [10.1051/0004-6361/202243940](https://doi.org/10.1051/0004-6361/202243940)
- Girardi, L., Bressan, A., Bertelli, G., & Chiosi, C. 2000, *A&AS*, 141, 371, doi: [10.1051/aas:2000126](https://doi.org/10.1051/aas:2000126)
- Goddard, D., Thomas, D., Maraston, C., et al. 2017, *MNRAS*, 466, 4731, doi: [10.1093/mnras/stw3371](https://doi.org/10.1093/mnras/stw3371)
- González Delgado, R. M., Pérez, E., Cid Fernandes, R., et al. 2014, *A&A*, 562, A47,
doi: [10.1051/0004-6361/201322011](https://doi.org/10.1051/0004-6361/201322011)
- González Delgado, R. M., García-Benito, R., Pérez, E., et al. 2015, *A&A*, 581, A103,
doi: [10.1051/0004-6361/201525938](https://doi.org/10.1051/0004-6361/201525938)
- Gordon, I., Rothman, L., Hargreaves, R., et al. 2022, *Journal of Quantitative Spectroscopy and Radiative Transfer*, 277, 107949,
doi: <https://doi.org/10.1016/j.jqsrt.2021.107949>
- Green, G. 2018, *The Journal of Open Source Software*, 3, 695, doi: [10.21105/joss.00695](https://doi.org/10.21105/joss.00695)
- Green, G. M., Schlafly, E., Zucker, C., Speagle, J. S., & Finkbeiner, D. 2019, *ApJ*, 887, 93,
doi: [10.3847/1538-4357/ab5362](https://doi.org/10.3847/1538-4357/ab5362)
- Greene, J. E., Janish, R., Ma, C.-P., et al. 2015, *ApJ*, 807, 11, doi: [10.1088/0004-637X/807/1/11](https://doi.org/10.1088/0004-637X/807/1/11)
- Gu, M., Greene, J. E., Newman, A. B., et al. 2022, *ApJ*, 932, 103, doi: [10.3847/1538-4357/ac69ea](https://doi.org/10.3847/1538-4357/ac69ea)
- Guiderdoni, B., & Rocca-Volmerange, B. 1987, *A&A*, 186, 1
- Habets, G. M. H. J., & Heintze, J. R. W. 1981, *A&AS*, 46, 193
- Hartmann, J. 1904, *ApJ*, 19, 268, doi: [10.1086/141112](https://doi.org/10.1086/141112)
- Heckman, T. M., Lehnert, M. D., Strickland, D. K., & Armus, L. 2000, *ApJS*, 129, 493, doi: [10.1086/313421](https://doi.org/10.1086/313421)
- Hill, L., Thomas, D., Maraston, C., et al. 2022, *MNRAS*, 509, 4308, doi: [10.1093/mnras/stab3263](https://doi.org/10.1093/mnras/stab3263)
- Ho, I. T., Kudritzki, R.-P., Kewley, L. J., et al. 2015, *MNRAS*, 448, 2030, doi: [10.1093/mnras/stv067](https://doi.org/10.1093/mnras/stv067)
- Hobbs, L. M. 1969, *ApJ*, 158, 461, doi: [10.1086/150210](https://doi.org/10.1086/150210)
- . 1974, *ApJ*, 191, 381, doi: [10.1086/152976](https://doi.org/10.1086/152976)
- Howk, J. C., Sembach, K. R., & Savage, B. D. 2003, *ApJ*, 586, 249, doi: [10.1086/346262](https://doi.org/10.1086/346262)
- Imig, J., Holtzman, J. A., Yan, R., et al. 2022, *AJ*, 163, 56,
doi: [10.3847/1538-3881/ac3ca7](https://doi.org/10.3847/1538-3881/ac3ca7)
- Johansson, J., Thomas, D., & Maraston, C. 2010, *MNRAS*, 406, 165, doi: [10.1111/j.1365-2966.2010.16683.x](https://doi.org/10.1111/j.1365-2966.2010.16683.x)
- . 2012, *MNRAS*, 421, 1908,
doi: [10.1111/j.1365-2966.2011.20316.x](https://doi.org/10.1111/j.1365-2966.2011.20316.x)
- Kauffmann, G., Heckman, T. M., White, S. D. M., et al. 2003, *MNRAS*, 341, 33,
doi: [10.1046/j.1365-8711.2003.06291.x](https://doi.org/10.1046/j.1365-8711.2003.06291.x)
- Kaviraj, S., Kirkby, L. A., Silk, J., & Sarzi, M. 2007, *MNRAS*, 382, 960, doi: [10.1111/j.1365-2966.2007.12475.x](https://doi.org/10.1111/j.1365-2966.2007.12475.x)
- Kobayashi, C., Karakas, A. I., & Lugaro, M. 2020, *ApJ*, 900, 179, doi: [10.3847/1538-4357/abae65](https://doi.org/10.3847/1538-4357/abae65)
- Kobayashi, C., Umeda, H., Nomoto, K., Tominaga, N., & Ohkubo, T. 2006, *ApJ*, 653, 1145, doi: [10.1086/508914](https://doi.org/10.1086/508914)
- Kos, J., Zwitter, T., Grebel, E. K., et al. 2013, *ApJ*, 778, 86, doi: [10.1088/0004-637X/778/2/86](https://doi.org/10.1088/0004-637X/778/2/86)
- Kuntschner, H. 2000, *MNRAS*, 315, 184,
doi: [10.1046/j.1365-8711.2000.03377.x](https://doi.org/10.1046/j.1365-8711.2000.03377.x)

- Kurucz, R. L. 1993, SYNTHE spectrum synthesis programs and line data
- . 2011, *Canadian Journal of Physics*, 89, 417, doi: [10.1139/p10-104](https://doi.org/10.1139/p10-104)
- La Barbera, F., Ferreras, I., Vazdekis, A., et al. 2013, *MNRAS*, 433, 3017, doi: [10.1093/mnras/stt943](https://doi.org/10.1093/mnras/stt943)
- La Barbera, F., Vazdekis, A., Ferreras, I., et al. 2019, *MNRAS*, 489, 4090, doi: [10.1093/mnras/stz2192](https://doi.org/10.1093/mnras/stz2192)
- Lallement, R., Bertin, P., Chassefiere, E., & Scott, N. 1993, *A&A*, 271, 734
- Law, D. R., Belfiore, F., Bershad, M. A., et al. 2022, *ApJ*, 928, 58, doi: [10.3847/1538-4357/ac5620](https://doi.org/10.3847/1538-4357/ac5620)
- Lazarz, D., Yan, R., Wilhelm, R., et al. 2022, *A&A*, 668, A21, doi: [10.1051/0004-6361/202243701](https://doi.org/10.1051/0004-6361/202243701)
- Le Borgne, J. F., Bruzual, G., Pelló, R., et al. 2003, *A&A*, 402, 433, doi: [10.1051/0004-6361:20030243](https://doi.org/10.1051/0004-6361:20030243)
- Lehner, N., & Howk, J. C. 2011, *Science*, 334, 955, doi: [10.1126/science.1209069](https://doi.org/10.1126/science.1209069)
- Leitherer, C., & Heckman, T. M. 1995, *ApJS*, 96, 9, doi: [10.1086/192112](https://doi.org/10.1086/192112)
- Lejeune, T., Cuisinier, F., & Buser, R. 1997, *A&AS*, 125, 229, doi: [10.1051/aas:1997373](https://doi.org/10.1051/aas:1997373)
- Leonardi, A. J., & Rose, J. A. 1996, *AJ*, 111, 182, doi: [10.1086/117772](https://doi.org/10.1086/117772)
- . 2003, *AJ*, 126, 1811, doi: [10.1086/377617](https://doi.org/10.1086/377617)
- Leśniewska, A., Michałowski, M. J., Gall, C., et al. 2023, *ApJ*, 953, 27, doi: [10.3847/1538-4357/acdfc](https://doi.org/10.3847/1538-4357/acdfc)
- Lonoce, I., Freedman, W. L., & Feldmeier-Krause, A. 2023, *ApJ*, 948, 65, doi: [10.3847/1538-4357/acc025](https://doi.org/10.3847/1538-4357/acc025)
- Lyubenova, M., Martín-Navarro, I., van de Ven, G., et al. 2016, *MNRAS*, 463, 3220, doi: [10.1093/mnras/stw2434](https://doi.org/10.1093/mnras/stw2434)
- Maksymowicz-Maciata, M., Spiniello, C., Martín-Navarro, I., et al. 2024, *MNRAS*, 531, 2864, doi: [10.1093/mnras/stae1318](https://doi.org/10.1093/mnras/stae1318)
- Maraston, C. 1998, *MNRAS*, 300, 872, doi: [10.1046/j.1365-8711.1998.01947.x](https://doi.org/10.1046/j.1365-8711.1998.01947.x)
- . 2005, *MNRAS*, 362, 799, doi: [10.1111/j.1365-2966.2005.09270.x](https://doi.org/10.1111/j.1365-2966.2005.09270.x)
- Maraston, C., Nieves Colmenárez, L., Bender, R., & Thomas, D. 2009, *A&A*, 493, 425, doi: [10.1051/0004-6361:20066907](https://doi.org/10.1051/0004-6361:20066907)
- Maraston, C., & Strömbäck, G. 2011, *MNRAS*, 418, 2785, doi: [10.1111/j.1365-2966.2011.19738.x](https://doi.org/10.1111/j.1365-2966.2011.19738.x)
- Maraston, C., Hill, L., Thomas, D., et al. 2020, *MNRAS*, 496, 2962, doi: [10.1093/mnras/staa1489](https://doi.org/10.1093/mnras/staa1489)
- Martín-Navarro, I., La Barbera, F., Vazdekis, A., Falcón-Barroso, J., & Ferreras, I. 2015, *MNRAS*, 447, 1033, doi: [10.1093/mnras/stu2480](https://doi.org/10.1093/mnras/stu2480)
- Martín-Navarro, I., Spiniello, C., Tortora, C., et al. 2023, *MNRAS*, 521, 1408, doi: [10.1093/mnras/stad503](https://doi.org/10.1093/mnras/stad503)
- McConnell, N. J., Lu, J. R., & Mann, A. W. 2016, *ApJ*, 821, 39, doi: [10.3847/0004-637X/821/1/39](https://doi.org/10.3847/0004-637X/821/1/39)
- Mehlert, D., Thomas, D., Saglia, R. P., Bender, R., & Wegner, G. 2003, *A&A*, 407, 423, doi: [10.1051/0004-6361:20030886](https://doi.org/10.1051/0004-6361:20030886)
- Mészáros, S., Allende Prieto, C., Edvardsson, B., et al. 2012, *AJ*, 144, 120, doi: [10.1088/0004-6256/144/4/120](https://doi.org/10.1088/0004-6256/144/4/120)
- Munari, U., & Zwitter, T. 1997, *A&A*, 318, 269
- Münch, G., & Zirin, H. 1961, *ApJ*, 133, 11, doi: [10.1086/146999](https://doi.org/10.1086/146999)
- Murga, M., Zhu, G., Ménard, B., & Lan, T.-W. 2015, *MNRAS*, 452, 511, doi: [10.1093/mnras/stv1277](https://doi.org/10.1093/mnras/stv1277)
- Neumann, J., Thomas, D., Maraston, C., et al. 2021, *MNRAS*, 508, 4844, doi: [10.1093/mnras/stab286810.48550/arXiv.2109.11564](https://doi.org/10.1093/mnras/stab286810.48550/arXiv.2109.11564)
- O’Connell, R. W. 1976, *ApJ*, 206, 370, doi: [10.1086/154392](https://doi.org/10.1086/154392)
- Ocvirk, P., Pichon, C., Lançon, A., & Thiébaud, E. 2006, *MNRAS*, 365, 46, doi: [10.1111/j.1365-2966.2005.09182.x](https://doi.org/10.1111/j.1365-2966.2005.09182.x)
- Oosterloo, T., Morganti, R., Crocker, A., et al. 2010, *MNRAS*, 409, 500, doi: [10.1111/j.1365-2966.2010.17351.x](https://doi.org/10.1111/j.1365-2966.2010.17351.x)
- Parikh, T., Saglia, R., Thomas, J., et al. 2024, *MNRAS*, 528, 7338, doi: [10.1093/mnras/stae448](https://doi.org/10.1093/mnras/stae448)
- Parikh, T., Thomas, D., Maraston, C., et al. 2021, *MNRAS*, 502, 5508, doi: [10.1093/mnras/stab449](https://doi.org/10.1093/mnras/stab449)
- . 2018, *MNRAS*, 477, 3954, doi: [10.1093/mnras/sty785](https://doi.org/10.1093/mnras/sty785)
- . 2019, *MNRAS*, 483, 3420, doi: [10.1093/mnras/sty3339](https://doi.org/10.1093/mnras/sty3339)
- Pellerin, A., Fullerton, A. W., Robert, C., et al. 2002, *ApJS*, 143, 159, doi: [10.1086/342268](https://doi.org/10.1086/342268)
- Pérez, E., Cid Fernandes, R., González Delgado, R. M., et al. 2013, *ApJL*, 764, L1, doi: [10.1088/2041-8205/764/1/L1](https://doi.org/10.1088/2041-8205/764/1/L1)
- Perna, M., Arribas, S., Catalán-Torrecilla, C., et al. 2020, *A&A*, 643, A139, doi: [10.1051/0004-6361/202038328](https://doi.org/10.1051/0004-6361/202038328)
- Perna, M., Arribas, S., Pereira Santaella, M., et al. 2021, *A&A*, 646, A101, doi: [10.1051/0004-6361/202039702](https://doi.org/10.1051/0004-6361/202039702)
- Phillips, A. P., Pettini, M., & Gondhalekar, P. M. 1984, *MNRAS*, 206, 337, doi: [10.1093/mnras/206.2.337](https://doi.org/10.1093/mnras/206.2.337)
- Phillips, M. M., Simon, J. D., Morrell, N., et al. 2013, *ApJ*, 779, 38, doi: [10.1088/0004-637X/779/1/38](https://doi.org/10.1088/0004-637X/779/1/38)
- Pickles, A. J. 1985, *ApJ*, 296, 340, doi: [10.1086/163454](https://doi.org/10.1086/163454)
- Poznanski, D., Prochaska, J. X., & Bloom, J. S. 2012, *MNRAS*, 426, 1465, doi: [10.1111/j.1365-2966.2012.21796.x](https://doi.org/10.1111/j.1365-2966.2012.21796.x)
- Puspitarini, L., & Lallement, R. 2012, *A&A*, 545, A21, doi: [10.1051/0004-6361/201219284](https://doi.org/10.1051/0004-6361/201219284)
- Renzini, A., & Buzzoni, A. 1986, in *Astrophysics and Space Science Library*, Vol. 122, *Spectral Evolution of Galaxies*, ed. C. Chiosi & A. Renzini, 195–231, doi: [10.1007/978-94-009-4598-2_19](https://doi.org/10.1007/978-94-009-4598-2_19)

- Richter, P., Krause, F., Fechner, C., Charlton, J. C., & Murphy, M. T. 2011, *A&A*, 528, A12, doi: [10.1051/0004-6361/201015566](https://doi.org/10.1051/0004-6361/201015566)
- Richter, P., Savage, B. D., Wakker, B. P., Sembach, K. R., & Kalberla, P. M. W. 2001a, *ApJ*, 549, 281, doi: [10.1086/319070](https://doi.org/10.1086/319070)
- Richter, P., Sembach, K. R., Wakker, B. P., et al. 2001b, *ApJ*, 559, 318, doi: [10.1086/322401](https://doi.org/10.1086/322401)
- Robert, C., Pellerin, A., Aloisi, A., et al. 2003, *ApJS*, 144, 21, doi: [10.1086/344478](https://doi.org/10.1086/344478)
- Robert, C. P., Chopin, N., & Rousseau, J. 2009, *Statistical Science*, 24, 141, doi: [10.1214/09-STS284](https://doi.org/10.1214/09-STS284)
- Roberts-Borsani, G. W., & Saintonge, A. 2019, *MNRAS*, 482, 4111, doi: [10.1093/mnras/sty2824](https://doi.org/10.1093/mnras/sty2824)
- Roberts-Borsani, G. W., Saintonge, A., Masters, K. L., & Stark, D. V. 2020, *MNRAS*, 493, 3081, doi: [10.1093/mnras/staa464](https://doi.org/10.1093/mnras/staa464)
- Rodríguez-Merino, L. H., Chavez, M., Bertone, E., & Buzzoni, A. 2005, *ApJ*, 626, 411, doi: [10.1086/429858](https://doi.org/10.1086/429858)
- Roig, B., Blanton, M. R., & Yan, R. 2015, *ApJ*, 808, 26, doi: [10.1088/0004-637X/808/1/26](https://doi.org/10.1088/0004-637X/808/1/26)
- Rose, J. A. 1985, *AJ*, 90, 1927, doi: [10.1086/113898](https://doi.org/10.1086/113898)
- Rubin, K. H. R., Diamond-Stanic, A. M., Coil, A. L., Crighton, N. H. M., & Moustakas, J. 2018, *ApJ*, 853, 95, doi: [10.3847/1538-4357/aa9792](https://doi.org/10.3847/1538-4357/aa9792)
- Rubin, K. H. R., Juarez, C., Cooksey, K. L., et al. 2022, *ApJ*, 936, 171, doi: [10.3847/1538-4357/ac7b88](https://doi.org/10.3847/1538-4357/ac7b88)
- Ruffa, I., Prandoni, I., Laing, R. A., et al. 2019, *MNRAS*, 484, 4239, doi: [10.1093/mnras/stz255](https://doi.org/10.1093/mnras/stz255)
- Rupke, D. S., Veilleux, S., & Sanders, D. B. 2005, *ApJS*, 160, 87, doi: [10.1086/432886](https://doi.org/10.1086/432886)
- Rupke, D. S. N., Thomas, A. D., & Dopita, M. A. 2021, *MNRAS*, 503, 4748, doi: [10.1093/mnras/stab743](https://doi.org/10.1093/mnras/stab743)
- Sánchez-Blázquez, P., Peletier, R. F., Jiménez-Vicente, J., et al. 2006, *MNRAS*, 371, 703, doi: [10.1111/j.1365-2966.2006.10699.x](https://doi.org/10.1111/j.1365-2966.2006.10699.x)
- Sánchez-Blázquez, P., Rosales-Ortega, F. F., Méndez-Abreu, J., et al. 2014, *A&A*, 570, A6, doi: [10.1051/0004-6361/201423635](https://doi.org/10.1051/0004-6361/201423635)
- Sandford, N. R., Weisz, D. R., & Ting, Y.-S. 2023, *ApJS*, 267, 18, doi: [10.3847/1538-4365/acd37b](https://doi.org/10.3847/1538-4365/acd37b)
- Schaller, G., Schaerer, D., Meynet, G., & Maeder, A. 1992, *A&AS*, 96, 269
- Schlegel, D. J., Finkbeiner, D. P., & Davis, M. 1998, *ApJ*, 500, 525, doi: [10.1086/305772](https://doi.org/10.1086/305772)
- Schmidt-Kaler. 1982, *Numerical Data and Functional Relationships in Science and Technology*, Landolt/Bornstein No. Group IV, Vol. 2(b) (Springer, Berlin)
- Sembach, K. R., & Danks, A. C. 1994, *A&A*, 289, 539
- Sembach, K. R., Danks, A. C., & Savage, B. D. 1993, *A&AS*, 100, 107
- Sembach, K. R., Savage, B. D., & Hurwitz, M. 1999, *ApJ*, 524, 98, doi: [10.1086/307811](https://doi.org/10.1086/307811)
- Serven, J., Worthey, G., & Briley, M. M. 2005, *ApJ*, 627, 754, doi: [10.1086/430400](https://doi.org/10.1086/430400)
- Smith, R. J., Lucey, J. R., & Carter, D. 2012, *MNRAS*, 426, 2994, doi: [10.1111/j.1365-2966.2012.21922.x](https://doi.org/10.1111/j.1365-2966.2012.21922.x)
- Spiniello, C., Trager, S. C., Koopmans, L. V. E., & Chen, Y. P. 2012, *ApJL*, 753, L32, doi: [10.1088/2041-8205/753/2/L32](https://doi.org/10.1088/2041-8205/753/2/L32)
- Spinrad, H., & Taylor, B. J. 1971, *ApJS*, 22, 445, doi: [10.1086/190232](https://doi.org/10.1086/190232)
- Spolaor, M., Kobayashi, C., Forbes, D. A., Couch, W. J., & Hau, G. K. T. 2010, *MNRAS*, 408, 272, doi: [10.1111/j.1365-2966.2010.17080.x](https://doi.org/10.1111/j.1365-2966.2010.17080.x)
- Starkeburg, E., Martin, N., Youakim, K., et al. 2017, *MNRAS*, 471, 2587, doi: [10.1093/mnras/stx1068](https://doi.org/10.1093/mnras/stx1068)
- Straka, L. A., Noterdaeme, P., Srianand, R., et al. 2015, *MNRAS*, 447, 3856, doi: [10.1093/mnras/stu2739](https://doi.org/10.1093/mnras/stu2739)
- Strand, K. 1963, *Basic Astronomical Data*, Basic Astronomical Data No. v. 3 (University of Chicago Press). <https://books.google.com/books?id=qInvAAAAMAAJ>
- Sūdžius, J., & Bobinas, V. 1994, *Baltic Astronomy*, 3, 158, doi: [10.1515/astro-1994-1-221](https://doi.org/10.1515/astro-1994-1-221)
- Taresch, G., Kudritzki, R. P., Hurwitz, M., et al. 1997, *A&A*, 321, 531
- Thomas, D., Johansson, J., & Maraston, C. 2011a, *MNRAS*, 412, 2199, doi: [10.1111/j.1365-2966.2010.18108.x](https://doi.org/10.1111/j.1365-2966.2010.18108.x)
- Thomas, D., Maraston, C., & Bender, R. 2003, *MNRAS*, 339, 897, doi: [10.1046/j.1365-8711.2003.06248.x](https://doi.org/10.1046/j.1365-8711.2003.06248.x)
- Thomas, D., Maraston, C., Bender, R., & Mendes de Oliveira, C. 2005, *ApJ*, 621, 673, doi: [10.1086/426932](https://doi.org/10.1086/426932)
- Thomas, D., Maraston, C., & Johansson, J. 2011b, *MNRAS*, 412, 2183, doi: [10.1111/j.1365-2966.2010.18049.x](https://doi.org/10.1111/j.1365-2966.2010.18049.x)
- Thomas, J., Saglia, R. P., Bender, R., et al. 2011c, *MNRAS*, 415, 545, doi: [10.1111/j.1365-2966.2011.18725.x](https://doi.org/10.1111/j.1365-2966.2011.18725.x)
- Tinsley, B. M. 1978, *ApJ*, 222, 14, doi: [10.1086/156116](https://doi.org/10.1086/156116)
- Trager, S. C., Worthey, G., Faber, S. M., Burstein, D., & González, J. J. 1998, *ApJS*, 116, 1, doi: [10.1086/313099](https://doi.org/10.1086/313099)
- Tremonti, C. A., Heckman, T. M., Kauffmann, G., et al. 2004, *ApJ*, 613, 898, doi: [10.1086/423264](https://doi.org/10.1086/423264)
- Treu, T., Auger, M. W., Koopmans, L. V. E., et al. 2010, *ApJ*, 709, 1195, doi: [10.1088/0004-637X/709/2/1195](https://doi.org/10.1088/0004-637X/709/2/1195)
- Tumlinson, J., Shull, J. M., Rachford, B. L., et al. 2002, *ApJ*, 566, 857, doi: [10.1086/338112](https://doi.org/10.1086/338112)
- Turnrose, B. E. 1976, *ApJ*, 210, 33, doi: [10.1086/154801](https://doi.org/10.1086/154801)

- Valdes, F., Gupta, R., Rose, J. A., Singh, H. P., & Bell, D. J. 2004, *ApJS*, 152, 251, doi: [10.1086/386343](https://doi.org/10.1086/386343)
- van Dokkum, P., Conroy, C., Villaume, A., Brodie, J., & Romanowsky, A. J. 2017, *ApJ*, 841, 68, doi: [10.3847/1538-4357/aa7135](https://doi.org/10.3847/1538-4357/aa7135)
- van Dokkum, P. G., & Conroy, C. 2010, *Nature*, 468, 940, doi: [10.1038/nature09578](https://doi.org/10.1038/nature09578)
- . 2012, *ApJ*, 760, 70, doi: [10.1088/0004-637X/760/1/70](https://doi.org/10.1088/0004-637X/760/1/70)
- VanderPlas, J. 2014, arXiv e-prints, arXiv:1411.5018, doi: [10.48550/arXiv.1411.5018](https://doi.org/10.48550/arXiv.1411.5018)
- Vaughan, S. P., Davies, R. L., Zieleniewski, S., & Houghton, R. C. W. 2018, *MNRAS*, 479, 2443, doi: [10.1093/mnras/sty1434](https://doi.org/10.1093/mnras/sty1434)
- Vazdekis, A. 1999, *ApJ*, 513, 224, doi: [10.1086/306843](https://doi.org/10.1086/306843)
- Vazdekis, A., Sánchez-Blázquez, P., Falcón-Barroso, J., et al. 2010, *MNRAS*, 404, 1639, doi: [10.1111/j.1365-2966.2010.16407.x](https://doi.org/10.1111/j.1365-2966.2010.16407.x)
- Veilleux, S., Maiolino, R., Bolatto, A. D., & Aalto, S. 2020, *A&A Rv*, 28, 2, doi: [10.1007/s00159-019-0121-9](https://doi.org/10.1007/s00159-019-0121-9)
- Vogriničič, R., Kos, J., Zwitter, T., et al. 2023, *MNRAS*, 521, 3727, doi: [10.1093/mnras/stad678](https://doi.org/10.1093/mnras/stad678)
- Wakker, B. P. 2001, *ApJS*, 136, 463, doi: [10.1086/321783](https://doi.org/10.1086/321783)
- Walborn, N. R. 1972, *AJ*, 77, 312, doi: [10.1086/111285](https://doi.org/10.1086/111285)
- . 1973, *AJ*, 78, 1067, doi: [10.1086/111509](https://doi.org/10.1086/111509)
- Welsh, B. Y., Lallement, R., Vergely, J. L., & Raimond, S. 2010, *A&A*, 510, A54, doi: [10.1051/0004-6361/200913202](https://doi.org/10.1051/0004-6361/200913202)
- Welty, D. E., Federman, S. R., Gredel, R., Thorburn, J. A., & Lambert, D. L. 2006, *ApJS*, 165, 138, doi: [10.1086/504153](https://doi.org/10.1086/504153)
- Welty, D. E., Morton, D. C., & Hobbs, L. M. 1996, *ApJS*, 106, 533, doi: [10.1086/192347](https://doi.org/10.1086/192347)
- Welty, D. E., Xue, R., & Wong, T. 2012, *ApJ*, 745, 173, doi: [10.1088/0004-637X/745/2/173](https://doi.org/10.1088/0004-637X/745/2/173)
- Westfall, K. B., Cappellari, M., Bershady, M. A., et al. 2019, *AJ*, 158, 231, doi: [10.3847/1538-3881/ab44a2](https://doi.org/10.3847/1538-3881/ab44a2)
- Whitford, A. E. 1977, *ApJ*, 211, 527, doi: [10.1086/154959](https://doi.org/10.1086/154959)
- Wild, V., & Hewett, P. C. 2005, *MNRAS*, 361, L30, doi: [10.1111/j.1745-3933.2005.00058.x](https://doi.org/10.1111/j.1745-3933.2005.00058.x)
- Wild, V., Kauffmann, G., Heckman, T., et al. 2007, *MNRAS*, 381, 543, doi: [10.1111/j.1365-2966.2007.12256.x](https://doi.org/10.1111/j.1365-2966.2007.12256.x)
- Wilkinson, D. M., Maraston, C., Goddard, D., Thomas, D., & Parikh, T. 2017, *MNRAS*, 472, 4297, doi: [10.1093/mnras/stx2215](https://doi.org/10.1093/mnras/stx2215)
- Wing, R. F., & Ford, W. Kent, J. 1969, *PASP*, 81, 527, doi: [10.1086/128814](https://doi.org/10.1086/128814)
- Woosley, S. E., & Weaver, T. A. 1995, *ApJS*, 101, 181, doi: [10.1086/192237](https://doi.org/10.1086/192237)
- Worthey, G., Faber, S. M., & Gonzalez, J. J. 1992, *ApJ*, 398, 69, doi: [10.1086/171836](https://doi.org/10.1086/171836)
- Worthey, G., Faber, S. M., Gonzalez, J. J., & Burstein, D. 1994, *ApJS*, 94, 687, doi: [10.1086/192087](https://doi.org/10.1086/192087)
- Worthey, G., & Ottaviani, D. L. 1997, *ApJS*, 111, 377, doi: [10.1086/313021](https://doi.org/10.1086/313021)
- Worthey, G., Tang, B., & Serven, J. 2014, *ApJ*, 783, 20, doi: [10.1088/0004-637X/783/1/20](https://doi.org/10.1088/0004-637X/783/1/20)
- Yan, R., Bundy, K., Law, D. R., et al. 2016, *AJ*, 152, 197, doi: [10.3847/0004-6256/152/6/197](https://doi.org/10.3847/0004-6256/152/6/197)
- Yan, R., Chen, Y., Lazarz, D., et al. 2019, *ApJ*, 883, 175, doi: [10.3847/1538-4357/ab3ebc](https://doi.org/10.3847/1538-4357/ab3ebc)
- Yao, Y., Tripp, T. M., Wang, Q. D., et al. 2009, *ApJ*, 697, 1784, doi: [10.1088/0004-637X/697/2/1784](https://doi.org/10.1088/0004-637X/697/2/1784)
- Youakim, K., Starkenburg, E., Aguado, D. S., et al. 2017, *MNRAS*, 472, 2963, doi: [10.1093/mnras/stx2005](https://doi.org/10.1093/mnras/stx2005)
- Young, L. M., Bureau, M., Davis, T. A., et al. 2011, *MNRAS*, 414, 940, doi: [10.1111/j.1365-2966.2011.18561.x](https://doi.org/10.1111/j.1365-2966.2011.18561.x)
- Zabludoff, A. I., Zaritsky, D., Lin, H., et al. 1996, *ApJ*, 466, 104, doi: [10.1086/177495](https://doi.org/10.1086/177495)
- Zych, B. J., Murphy, M. T., Hewett, P. C., & Prochaska, J. X. 2009, *MNRAS*, 392, 1429, doi: [10.1111/j.1365-2966.2008.14157.x](https://doi.org/10.1111/j.1365-2966.2008.14157.x)
- Zych, B. J., Murphy, M. T., Pettini, M., et al. 2007, *MNRAS*, 379, 1409, doi: [10.1111/j.1365-2966.2007.12015.x](https://doi.org/10.1111/j.1365-2966.2007.12015.x)